Master's thesis

NTNU
Norwegian University of Science and Technology
Faculty of Natural Sciences
Department of Physics

Sondre Erik Wennberg

Simulating future alternatives for the mixed energy system in Longyearbyen with different scales of renewable energy installations

Master's thesis in Applied Physics and Mathematics
Supervisor: Jon Andreas Støvneng
Co-supervisor: Harald G. Svendsen
June 2022

NTNU
Norwegian University of Science and Technology

Sondre Erik Wennberg

Simulating future alternatives for the mixed energy system in Longyearbyen with different scales of renewable energy installations

Master's thesis in Applied Physics and Mathematics
Supervisor: Jon Andreas Støvneng
Co-supervisor: Harald G. Svendsen
June 2022

Norwegian University of Science and Technology
Faculty of Natural Sciences
Department of Physics

NTNU
Norwegian University of
Science and Technology

Abstract

The mixed electricity and heating energy system in Longyearbyen, Svalbard is currently completely coal based, with a diesel installation operating as a backup system. In light of the climate crisis, however, it has been decided that the coal power plant is to be closed, and the diesel system will cover the demand in an energy transition period. In this period, renewable energy sources will gradually be phased in and eventually fully cover the energy demand of the town. In addition, the renewable system will have the capacity to function as a fossil free backup system to ensure the crucial energy security for the remote off grid settlement.

In this work, wind speed measurements, global weather model data, energy demand timeseries, and other data sources have been combined to simulate potential energy systems for Longyearbyen. By expanding a mixed integer linear programming modeling python package, energy system constellations were optimized to minimize fuel and operational costs using rolling optimization horizons for simulation lengths of one year. The cases primarily included, in addition to the transitional diesel system, photovoltaics, wind power, geothermal heat pumps, and a full hydrogen system with electrolysers, compressed storage, and fuel cells.

The simulation of the transitional diesel case resulted in CO_2 emissions of $35 \cdot 10^6$ kg/year, which is a reduction of 55% from the current emissions. The yearly costs for running the system, including a carbon tax of 2 NOK/kg, ended up at 149 MNOK, 61% higher than the current coal power plant operational costs.

Using a 25 MW photovoltaic installation, a 31 MW onshore wind installation, a 5.2 MW geothermal heat pump installation, and a compressed hydrogen storage capacity of 107 900 kg as the primary energy devices supplementing the diesel system, emission reductions of 94% from the current power plant were obtained. The yearly costs, including investment costs annualized over the expected lifetime of each investment, are found to be 92.5 MNOK, 38% lower than for the transitional diesel case and the same as the current costs. A fully renewable case with larger wind and hydrogen storage installations was found to have higher yearly costs of 101 MNOK, which is 32% lower than for the diesel case. Taking into account effects of known seasonal variability proved key to long term optimization.

The reduction of up to all carbon dioxide emissions from the energy production in Longyearbyen is found to not only be technologically feasible given existing renewable technologies and local wind and solar conditions, but it is also estimated to require a modest enough installation to be economically viable.

Figure 1: The author investigating the viability of charging small electrical appliances by harnessing the wind power potential near Longyearbyen on Svalbard.

Sammendrag

Det nåværende kraftvarmeverket for Longyearbyen, Svalbard er kullbasert, med et dieselbasert reservesystem. Grunnet klimakrisen har det imidlertid blitt vedtatt å stenge kullkraftverket og la dieselsystemet overta energiforsyningen i en overgangsperiode. I denne perioden skal fornybare energikilder bli faset inn og etterhvert kunne både dekke byens behov på egen hånd, samt ha kapasitet nok til å fungere som et fossilfritt reservesystem for å sikre den kritisk viktige energisikkerheten til den avsidesliggende bosetningen.

I denne oppgaven har vindhastighetsdata fra målestasjoner, data fra en global værmodell, tidsserier for byens energiforbruk, og andre datakilder blitt kombinert for å simulere mulige energisystemer for Longyearbyen. Ved å videreutvikle en python-pakke som lager og løser et lineært blandet heltallsprogram, ble ulike energisystemsammensetninger optimalisert med hensyn på drivstoff- og driftskostnader ved å benytte rullende horisonter og simuleringslengder på ett år. De ulike tilfellene inkluderte hovedsaklig, i tillegg til overgangsdieselsystemet, solceller, vindkraft, geotermiske varmepumper og et fullstendig hydrogensystem med elektrolyseapparat, komprimert lagring og brenselsceller.

Simuleringen av dieseltilfellet ga CO_2-utslipp på $35 \cdot 10^6$ kg per år, som er en reduksjon på 55% fra dagens kullkraftverksutslipp. De årlige kostnadene for å drive energisystemet, inkludert en CO_2-avgift på 2 NOK per kg, ble 149 MNOK, som er 61% høyere enn dagens kullkraftverkskostnader.

Ved å implementere hovedsaklig en solcelleinstallasjon på 25 MW, en vindkraftsinstallasjon på 31 MW, en geotermisk installasjon på 5.2 MW og en komprimert hydrogenlagringskapasitet på 107 900 kg for å supplere dieselsystemet, oppnådde simuleringen utslippskutt på 94% i forhold til nåværende kraftverk. De årlige kostnadene for dette tilfellet, inkludert investeringskostnader annualisert over forvented levetid for hver investering, var 92.5 MNOK, som er 38% lavere enn for dieseltilfellet og det samme som dagens kraftverkskostnader. Et fullstendig fornybart alternativ med større vind- og hydrogenlagerinvesteringer ga noe høyere årlige kostnader på 101 MNOK, som fremdeles er 32% lavere enn for tilfellet med kun dieselsystemet. Å ta hensyn til effektene av kjente sesongvariasjoner viste seg å være sentralt for å optimalisere systemet over lange tidshorisonter.

Reduksjon av opp til alt karbondioksidutslipp fra Longyearbyens energiproduksjon har her vist seg å ikke bare være teknisk mulig med eksisterende teknologier og lokale vind- og solforhold, men det har også blitt anslått å kreve en investering av beskjeden nok størrelse til å være økonomisk forsvarlig.

Preface

This master's thesis is written during the spring semester of 2022 for the Master of Science degree in Applied Physics and Mathematics, with the specialization in Applied Physics, at the Norwegian University of Science and Technology (NTNU) in Trondheim, Norway. It is written for SINTEF Energy as part of the FME NorthWind research project (Norwegian Research Centre on Wind Energy).

Acknowledgements

Firstly I want to thank my supervisor Harald G. Svendsen at SINTEF Energy for continued guidance, support, and feedback throughout this project, especially with regard to the energy system optimization model. I am grateful for getting the opportunity to conduct this thesis work.

I also want to thank my supervisor at the Department of Physics at NTNU, professor Jon Andreas Støvneng, for helping the project get underway.

I would also like to thank Guttorm Nygård and Mons Ole Sellevold at Store Norske for help and input on geothermal heat pumps for Longyearbyen, as well as fruitful discussions around the feasibility of wind power at different locations and the status of the existing diesel system.

Sondre Erik Wennberg
June, 2022

Contents

Abstract . . . . . **iii**
Sammendrag . . . . . **v**
Preface . . . . . **vii**
Acknowledgements . . . . . **vii**
Contents . . . . . **ix**
Figures . . . . . **xi**
Tables . . . . . **xiii**
1 Introduction **1**
1.1 Outline of the thesis 2
2 Theory **5**
2.1 Wind profile 5
2.1.1 The Navier-Stokes equations 5
2.1.2 Reynolds decomposition 7
2.1.3 Approximations of the boundary layer atmosphere 8
2.1.4 Reynolds averaged Navier-Stokes 9
2.1.5 The logarithmic wind profile 10
2.2 Compression work on hydrogen 12
2.2.1 The compressibility factor 13
2.2.2 Isothermal compression 15
2.2.3 Adiabatic compression 17
2.2.4 Comparison of isothermal and adiabatic compression work . 19
3 Modeling an integrated electricity and heating system using Oogeso 21
3.1 The optimization problem to be solved 21
3.2 Existing Oogeso features and devices used 23
3.2.1 A generic device 24
3.2.2 Energy carrier sources 25
3.2.3 Energy carrier sinks 26
3.2.4 Electrical energy storage 26
3.2.5 Heat pump 27
3.2.6 Hydrogen system 27
3.3 Devices implemented in Oogeso as part of this work 28
3.3.1 Additions to the generic device 29
3.3.2 Diesel system 30
3.3.3 Compressed hydrogen storage 31
3.4 Final objective function 35

4 Energy system devices and data sources . . . 37
4.1 Existing diesel system . . . 38
4.1.1 Diesel as an energy carrier . . . 38
4.1.2 Diesel generators . . . 39
4.1.3 Diesel boilers . . . 40
4.2 Battery . . . 40
4.3 Photovoltaic power . . . 41
4.4 Wind power . . . 42
4.4.1 Onshore . . . 44
4.4.2 Offshore . . . 47
4.5 Electric boiler . . . 51
4.6 Geothermal heat pump . . . 51
4.7 Hydrogen system . . . 52
4.7.1 Hydrogen as an energy carrier . . . 53
4.7.2 Electrolyser . . . 53
4.7.3 Compression and storage . . . 54
4.7.4 Fuel cells . . . 56
4.8 Load . . . 56
5 Different modeling cases . . . 59
5.1 Case 1: base case . . . 60
5.2 Case 2: PV installation . . . 61
5.3 Case 3: PV, geothermal, and small onshore wind installations . . . 63
5.4 Case 4: all devices - onshore . . . 65
5.5 Case 5: all devices - offshore . . . 67
5.6 Case 6: fully renewable - onshore . . . 69
6 Discussion of the simulated cases . . . 71
6.1 CO_2 emissions . . . 71
6.2 Diesel system usage . . . 74
6.3 Energy usage . . . 77
6.4 Curtailed power production . . . 80
6.5 Hydrogen production . . . 81
6.6 Energy loss . . . 82
6.7 Costs for each case . . . 84
6.8 The feasibility of the different cases . . . 87
7 Discussion of the modelling approach . . . 91
7.1 The chosen modelling framework . . . 91
7.2 The parameters used in the Oogeso model . . . 93
7.2.1 Diesel fuel costs . . . 93
7.2.2 CO_2 emissions . . . 94
7.2.3 Wind farm dimensioning . . . 94
7.2.4 Hydrogen system and electric heating . . . 94
7.3 Further work . . . 96
8 Conclusion . . . 99
Bibliography . . . 101
A Additional simulated cases . . . 109

Figures

1 The author investigating wind power on Svalbard. iv

2.1 Coordinate system used in the derivation of the wind profile. 6
2.2 Compressibility factor, $Z(p,T)$ of hydrogen gas. 14
2.3 Isothermal compressibility factor, $Z(p)$, of hydrogen gas. 15
2.4 Isothermal compression work on hydrogen gas. 16
2.5 Hydrogen compressibility factor, $Z(p,T)$, along adiabats. 18
2.6 Adiabatic compression work on hydrogen gas. 19
2.7 Both isothermal and adiabatic compression work on hydrogen gas. 20

3.1 Example of an energy system network modeled in Oogeso. 22

4.1 Photovoltaic capacity factors for 2018. 41
4.2 Power curve for the Vestas V105 wind turbine. 43
4.3 Location of the onshore weather stations. 44
4.4 Onshore wind capacity factors for 2018. 45
4.5 Breinosa capacity factor duration curves for 2018. 45
4.6 Onshore wind speed duration curves for 2018. 46
4.7 Location of the offshore weather station. 47
4.8 Offshore wind capacity factors for 2018. 48
4.9 Offshore capacity factor duration curves for 2018. 49
4.10 Offshore wind speed duration curves for 2018. 49
4.11 Onshore and offshore capacity factor duration curves for 2018. . . . 50
4.12 The capacity factors for the geothermal heat installation for a year. 52
4.13 Hydrogen storage target profile. 55
4.14 Electricity and heat load for Longyearbyen for 2018. 57

5.1 Case 1 energy flow diagram. 60
5.2 Case 2 energy flow diagram. 61
5.3 Case 3 energy flow diagram. 64
5.4 Case 4 and 5 energy flow diagram. 66
5.5 Case 4 hydrogen storage level. 68
5.6 Case 5 hydrogen storage level 68
5.7 Case 6 energy flow diagram. 69
5.8 Case 6 hydrogen storage level. 70

6.1 CO_2 emissions for all six cases. 72
6.2 CO_2 emissions per emission device for five cases. 73
6.3 Diesel device start up counts for five cases. 74
6.4 Diesel device operating hours for five cases. 75
6.5 CO_2 emissions per diesel device operational hour for five cases. . . 76
6.6 Diesel device running hours per start up count for five cases. 76
6.7 Electricity consumption for all six cases. 77
6.8 Energy consumption for all six cases. 78
6.9 Curtailed heat energy for all six cases. 79
6.10 Curtailed PV and wind energy for two cases. 80
6.11 Hydrogen production for three cases. 81
6.12 Yearly energy losses from curtailment or energy conversion. 82
6.13 Yearly expenses for all six cases. 84
6.14 Yearly non-investment costs for all six cases. 85
6.15 Total expenses for installing and operating all six cases for 20 years. 86
6.16 Investment and operational expenses for 20 years for case 4. 86

A.1 Carbon dioxide emissions for 12 different cases. 111
A.2 Running hours of the diesel devices per year for 12 cases. 112
A.3 Total energy consumption or 12 cases. 113
A.4 Curtailed renewable energy for 6 cases. 114
A.5 Yearly energy losses for 12 cases. 115
A.6 Yearly costs for 12 cases. 116
A.7 Yearly non-investment costs for 12 cases. 117

Tables

2.1 Constants for the Lemmon equation 14

4.1 Diesel data used in the optimization model. 38
4.2 Diesel generator data used in the optimization model. 39
4.3 Diesel boiler data used in the optimization model. 40
4.4 Battery data used in the optimization model. 41
4.5 Photovoltaic (PV) data used in the optimization model. 42
4.6 Onshore wind data used in the optimization model. 47
4.7 Offshore wind data used in the optimization model. 50
4.8 Electric boiler data used in the optimization model. 51
4.9 Geothermal heat pump data used in the optimization model. 52
4.10 Hydrogen data at 273.15 K and 1 atm. 53
4.11 Electrolyser data used in the optimization model. 53
4.12 Compressed hydrogen storage data used in the optimization model. 55
4.13 Fuel cell data used in the optimization model. 56

5.1 Installed capacities of different energy systems for all six cases. . . . 59
5.2 Key results after simulating case 1 for one year. 62
5.3 Key results after simulating case 2 for one year. 62
5.4 Key results after simulating case 3 for one year. 63
5.5 Key results after simulating case 4 for one year. 65
5.6 Key results after simulating case 5 for one year. 67
5.7 Key results after simulating case 6 for one year. 70

Chapter 1

Introduction

The town of Longyearbyen is one of the northernmost settlements in the world, being located at 78°N latitude on Spitsbergen in Svalbard, Norway. With over 2500 inhabitants, it is also the only settlement north of 75°N with a population of comparable size. The initial settlement was established to extract coal in 1903, and to this day the coal industry has been one of the main reasons for sustaining the settlement, though scientific research and tourism have become very important areas in the most recent decades [1]. With the local coal production, the energy supply for Longyearbyen has been coal based for its entire history, with a backup diesel system appearing relatively recently [2].

With the urgency of the climate crisis, and the particularly strong effects of global warming in the Arctic, the Community Council of Longyearbyen has decided to move towards a future that is not powered by coal. In the community plan for the period 2022-2033 [3], 7 of the United Nations' Sustainable Development Goals [4] are prioritized. Among those are goal 7 (Affordable and clean energy), 11 (Sustainable cities and communities), and 13 (Climate action). Reducing the carbon footprint of the town ties in to the details of how Longyearbyen policy is formed to meet these goals, and in 2021 it was decided to shut down the coal power plant within 2023 [5]. While the transitional energy supply is set to be the existing diesel system, the aim is to gradually phase in renewable sources in the remote, off grid energy system [6]. Within 2030, the politically agreed goal is to reduce the carbon dioxide emissions from energy production by 80% compared to the 2018 levels.

Previously, reports have been made considering various energy systems and the related costs for implementing them on Svalbard. Most notably among those is one made for the Norwegian oil and energy department by THEMA and Multiconsult in 2018 [7], and one by Statkraft in the same year [8]. Additionally, the university Centre in Svalbard (UNIS) has had several projects and courses researching aspects of renewable energy in the settlement [9]. In the most recent years, however, the pace of the energy transition has increased, with the closure of the coal mine and coal power plant set to occur four years earlier than anticipated in the reports, while the adopted emission reduction goals have been increased.

In this work, the aim is to simulate potential renewable additions to the energy system in Longyearbyen, with a focus on wind power and hydrogen production for long term energy storage. Contrary to previous studies, the goal of this project is to simulate the entire energy system on an hourly basis over several seasons, using hourly data timeseries for all relevant energy system devices. The simulation will thus consider short term, mid term, and long term variability of energy production, demand, and storage. It may be that the heating demand correlates with high wind speeds for the next few hours, while the the wind and photovoltaic potential is forecasted to drop to a minimum for several days next week, and at the same time the currently available hydrogen storage is slightly below the estimated amount needed for the next 6 months. The model should take all such events into account when making decisions for the optimal choice for meeting energy demand for the next few hours. In this way, the model will make choices using the same kind of information an operator of the system would possess in a realistic scenario. The result from using actual data from the same years in such a model should produce realistic results, while also being applicable to use as a tool for operating an actual mixed energy off grid system with intermittent sources.

A disadvantage of the renewable energy sources of wind and photovoltaic cells, as illustrated above, is that they are intermittent, and thus not reliably providing the needed power when it is needed. The production and storage of hydrogen will be looked at for mediating and distributing the energy from times of high production to the times where energy demand surpasses momentary production. Another challenge with transitioning away from a fossil based energy source for Longyearbyen, is providing heat energy to the district heating system. This demand is significantly higher than the electricity demand and is currently provided from the "waste" heat from the coal power plant.

1.1 Outline of the thesis

Chapter 2 will discuss two theoretical issues of importance to this thesis. The wind speed at a certain height above the ground will be needed, while measurements are available at select heights. To this end the logarithmic wind profile will be derived using properties of momentum transport in the atmosphere. Next, to model compressed hydrogen storage, expressions for isothermal and adiabatic hydrogen compression are derived. Approximations linear in the amount of hydrogen are found for use in the model, and compared with the nonlinear expressions.

In chapter 3 the expanded mixed integer linear programming (MILP) model is explained. This model will assure that all physical constraints are obeyed, while optimizing resource usage with a rolling optimization horizon. The linear hydrogen compression expressions will be implemented into a device in this model.

Relevant data for all energy systems added to the model are presented and explained in chapter 4. In particular, to assess the potential of wind power, measurement data from various weather stations in the proximity of Longyearbyen are obtained. The corresponding wind data at higher elevations, where the blades of wind turbines are located, are estimated using the logarithmic wind profile. Furthermore, Store Norske has provided details of a potential geothermal heat pump installation in the town that will here be implemented as a potential way of covering parts of the heating demand in the mixed energy system.

Chapter 5 presents six energy system configurations that are simulated for one year, with simulation results like carbon dioxide emissions, renewable electricity production, and hydrogen storage levels.

In the sixth chapter, results from the six cases will be compared and discussed to assess the viability of the different energy system installations. Both emissions and energy consumption, as well as energy losses and costs for all the simulated cases, will be compared to both the current status with the coal power plant and the planned transitional diesel system.

The optimization model itself and thoughts around parameter choices, applicability for other locations, and possibilities for future improvements will be discussed in chapter 7.

The findings will then be summarized as a conclusion in chapter 8.

Chapter 2

Theory

2.1 Wind profile

In order to estimate the power output of a wind turbine, it is necessary to know the wind speeds at the height where the hub of the turbine is located. As wind speeds are typically measured at much lower heights than the heights of the wind turbines of interest[1], it is useful to derive an expressions for how the wind speed scales with height.

2.1.1 The Navier-Stokes equations

The *Navier-Stokes equations* describe the motion of fluids. In the case of the atmosphere of the earth, the equations take the form [10]

$$\frac{\partial u_i}{\partial t} = -u_j \frac{\partial u_i}{\partial x_j} - \frac{1}{\rho}\frac{\partial p}{\partial x_i} + \varepsilon_{ij3} f u_j - \delta_{i3} g + \frac{1}{\rho}\frac{\partial \tau_{ij}}{\partial x_j}. \tag{2.1}$$

Here the Einstein summation convention is used, meaning that repeated indices in each term are summed over. Each index can take three values, 1,2,3, one for each cartesian coordinate in 3D space. The coordinates are defined such that direction $x_1 = x$, is east, direction $x_2 = y$ is north, and direction $x_3 = z$, is up, as displayed in Figure 2.1. Furthermore, u_i is the wind in the i direction, with the common labels $u_1 = u$, $u_2 = v$, and $u_3 = w$. Next, ρ is the air density, p is the atmospheric pressure, g is the gravitational acceleration, and f is the Coriolis parameter defined as $f = 2\Omega \sin\phi$, with Ω being the rotation frequency of the earth and ϕ being the latitude, as defined in Figure 2.1. The Levi-Civita symbol, ε_{ijk} is defined to be equal to 1 if the indices are an even permutation of $(1,2,3)$, -1 if they are an odd permutation of $(1,2,3)$, and 0 otherwise. The Kronecker delta symbol, δ_{ij}, is defined to be equal to 1 for equal indices, and 0 otherwise.

Finally, the shear stress tensor, τ_{ij} is

[1] Weather stations, for instance, often measure wind speeds at heights of 10 meters or less above the ground. Wind turbines, on the other hand, may have hub heights exceeding 100 meters.

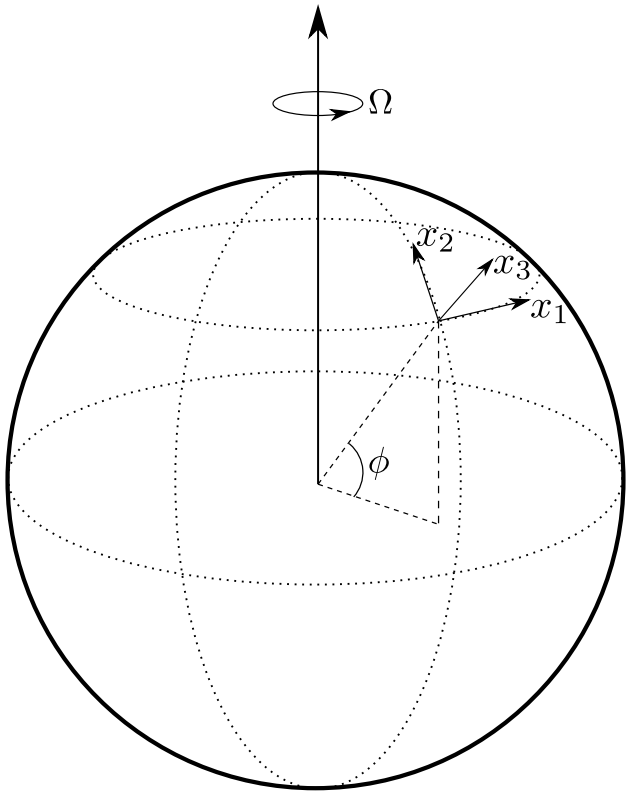

Figure 2.1: The coordinate system for which the Navier-Stokes equations, Equation (2.1), are defined for the atmosphere on the planet. A point on the northern hemisphere, at a latitude of ϕ from the equator, is chosen as the origin of the coordinates. Then $x_1 = x$ is pointed eastward, $x_2 = y$ is pointed northward, and $x_3 = z$ is pointed up and radially outwards from the earth. The earth has a rotation frequency of Ω around its rotation axis, causing the Coriolis parameter at the origin of the coordinate system to be $f = 2\Omega \sin(\phi)$.

$$\tau_{ij} = \mu \left(\frac{\partial u_i}{\partial x_j} + \frac{\partial u_j}{\partial x_i} - \frac{2}{3} \frac{\partial u_k}{\partial x_k} \delta_{ij} \right), \tag{2.2}$$

where μ is the dynamic viscosity.

The Navier-Stokes equations[2] will be used to find the effect of turbulent flow on momentum transport in the atmosphere, but first the framework of Reynold's decomposition must be defined.

[2]The centrifugal force is not explicitly included in Equation (2.1), but for a given location on earth's surface it will be of constant magnitude with constant components in the x_2 and x_3 directions. The latter can be thought of as decreasing the value of the gravitational acceleration, g, to an effective gravitational constant in the same direction, while the former will simply be a constant term in the x_2 direction. As constant terms not in the x_3 direction are not relevant in the following derivation, it is omitted.

2.1.2 Reynolds decomposition

The *Reynolds number* of a fluid is defined as $Re = \frac{LU}{\nu}$, with ν being the fluid's kinematic viscosity and L and U being characteristic length and velocity scales of the fluid's flow, respectively. When the value of this quantity exceeds the order of 5000, the fluid flow is turbulent [11]. This is the case for flow in the planetary boundary layer[3], where the turbulent transfer of for example momentum is of significance, and the characteristic scales are the sizes and velocities of eddies in the flow.

In order to include turbulent motion into the Navier-Stokes equations Equation (2.1), *Reynolds decomposition* is applied to all variables. The variables are then decomposed into a mean part, $\overline{x}$, and a (turbulent) fluctuating part, x', yielding

$$x = \overline{x} + x'. \tag{2.3}$$

The turbulent part of this decomposition, x' has to be varying over much shorter timescales than variations of the mean part, $\overline{x}$. The mean properties can then be regarded as steady [11], and the following *Reynolds postulates* hold for the averaging of flows $x = \overline{x} + x'$, $y = \overline{y} + y'$, with a being a constant [10]:

$$\begin{aligned}
&\textbf{I} && \overline{x'} = 0 \\
&\textbf{II} && \overline{xy} = \overline{x}\,\overline{y} + \overline{x'y'} \\
&\textbf{III} && \overline{\overline{x}y} = \overline{x}\,\overline{y} \\
&\textbf{IV} && \overline{ax} = a\overline{x} \\
&\textbf{V} && \overline{x+y} = \overline{x} + \overline{y}
\end{aligned} \tag{2.4}$$

For later use, several further relations when it comes to averaging decomposable variables and their constituents are derived from the Reynolds postulates here:

$$\begin{aligned}
\overline{\overline{x}} &= \overline{x - x'} = \overline{x} - \overline{x'} = \overline{x} \\
\overline{xy'} &= \overline{x(y - \overline{y})} = \overline{xy} - \overline{x\overline{y}} = \overline{x}\,\overline{y} + \overline{x'y'} - \overline{x}\,\overline{y} = \overline{x'y'} \\
\overline{\overline{x}y'} &= \overline{(x - x')y'} = \overline{xy'} - \overline{x'y'} = \overline{x'y'} - \overline{x'y'} = 0 \\
\overline{\overline{x}\,\overline{y}} &= \overline{\overline{x}(y - y')} = \overline{\overline{x}y} - \overline{xy'} = \overline{x}\,\overline{y} \\
\overline{\partial x} &= \partial\overline{x}
\end{aligned} \tag{2.5}$$

With these relations, a few approximations regarding the properties of the lower atmosphere will be made.

[3]The planetary boundary layer is the layer of earth's atmosphere that is directly influenced by the earth's surface, for example by the turbulence-induced transport processes. This layer typically comprises the lowest kilometers of the atmosphere [12].

2.1.3 Approximations of the boundary layer atmosphere

Approximating the atmosphere to be an ideal gas, it can be described by the *ideal gas law* [11],

$$p = R_m \rho T, \tag{2.6}$$

with p being pressure, ρ the atmospheric density and T the temperature of the atmosphere. R_m is then the specific gas constant of the atmosphere [4]. Decomposing all the variables in Equation (2.6) into mean and varying parts yield

$$\overline{p} + p' = R_m(\overline{\rho} + \rho')(\overline{T} + T'). \tag{2.7}$$

Equation (2.7) can again be averaged, giving, with $\overline{\overline{p} + p'} = \overline{p}$,

$$\overline{p} = \overline{R_m(\overline{\rho}\ \overline{T} + \overline{\rho}T' + \overline{T}\rho' + \rho'T')} = R_m(\overline{\rho}\ \overline{T} + \overline{\rho'T'}) = R_m\overline{\rho}\ \overline{T}(1 + \frac{\overline{\rho'T'}}{\overline{\rho}\ \overline{T}}). \tag{2.8}$$

In the atmosphere, it has been found that $\left|\frac{\rho'}{\overline{\rho}}\right| \lesssim 10^{-2}$ and $\left|\frac{p'}{\overline{p}}\right| \lesssim 10^{-2}$ [13]. Then the last term of Equation (2.8) is negligible, and the resulting approximate relation has the same form as the ideal gas law, Equation (2.6), but with mean values:

$$\overline{p} \approx R_m\overline{\rho}\,\overline{T} \tag{2.9}$$

Now dividing Equation (2.7) by Equation (2.9) yields

$$1 + \frac{p'}{\overline{p}} \approx 1 + \frac{\rho'}{\overline{\rho}} + \frac{T'}{\overline{T}} + \frac{\rho'T'}{\overline{\rho}\ \overline{T}}. \tag{2.10}$$

Here again, the last term in Equation (2.10) is negligible compared to the other terms, giving the final relation

$$\frac{p'}{\overline{p}} \approx \frac{\rho'}{\overline{\rho}} + \frac{T'}{\overline{T}}. \tag{2.11}$$

Observations[5] have shown that $\left|\frac{p'}{\overline{p}}\right| \ll \left|\frac{\rho'}{\overline{\rho}}\right| + \left|\frac{T'}{\overline{T}}\right|$ [13]. The following approximations can thus be made for the boundary layer of the atmosphere:

[4] R_m is related to the universal gas constant, R, by $R = MR_m$, where M is the molar weight of the gas, which for air is 28.96 g/mol [11]

[5] As the pressure is related to the mass of the column of air above the region, it is reasonable to find that the relative pressure fluctuations are very small in the lower portion of the atmosphere.

$$\begin{aligned}
\frac{\rho'}{\overline{\rho}} &\ll 1 \\
\frac{T'}{\overline{T}} &\ll 1 \\
\frac{p'}{\overline{p}} &\ll \frac{\rho'}{\overline{\rho}} \\
\frac{p'}{\overline{p}} &\ll \frac{T'}{\overline{T}}
\end{aligned} \tag{2.12}$$

When these approximations hold, as observations have shown them to do in the boundary layer of the atmosphere, another important approximation can be made to the Navier-Stokes equations. This is the *Boussinesq approximation*, in which density fluctuations is neglected in all but the gravitational term. The gravitational term is instead modified with a potential temperature term [12]. The procedure of the Boussinesq approximation is then the following,

- Replace ρ with $\overline{\rho}$.
- Replace g with $\left(1-\frac{\theta'}{\overline{\theta}}\right)g$.

Here θ is the potential temperature, which is the temperature a system would assume if it is adiabatically compressed or expanded to the standard pressure of 1 bar [11].

This Boussinesq approximation is equivalent to incompressibility [11], which also affects the shear stress term of the Navier-Stokes equations, Equation (2.1). With incompressible flow, the divergence is zero, $\partial_j u_j = 0$, which gives

$$\frac{1}{\rho}\frac{\partial \tau_{ij}}{\partial x_j} = \nu\frac{\partial}{\partial x_j}\left(\frac{\partial u_i}{\partial x_j}+\frac{\partial u_j}{\partial x_i}-\frac{2}{3}\frac{\partial u_k}{\partial x_k}\delta_{ij}\right) = \nu\frac{\partial^2 u_i}{\partial x_j^2} = \nu\nabla^2 u_i. \tag{2.13}$$

Another consequence of having zero divergence is that $\partial_j(u_j u_i) = u_j\partial u_i + u_i\partial u_j = u_j\partial u_i$, which will be used in the first term on the left, the convection term, of Equation (2.1).

With all these approximations and their effects in place, it is time to apply them to the Navier-Stokes equations of motion.

2.1.4 Reynolds averaged Navier-Stokes

Applying Reynolds decomposition, the Boussinesq approximation, and the resulting incompressibility on the Navier-Stokes equations, Equation (2.1), yields

$$\begin{aligned}
\frac{\partial}{\partial t}\left(\overline{u_i}+u_i'\right) = &-\frac{\partial}{\partial x_j}\left(\left(\overline{u_i}+u_i'\right)\left(\overline{u_j}+u_j'\right)\right)-\frac{1}{\overline{\rho}}\frac{\partial}{\partial x_i}\left(\overline{p}+p'\right) \\
&+\varepsilon_{ij3}f\left(\overline{u_j}+u_j'\right)-\delta_{i3}\left(1-\frac{\theta'}{\overline{\theta}}\right)g+\nu\nabla^2\left(\overline{u_i}+u_i'\right).
\end{aligned} \tag{2.14}$$

Reynolds averaging all the terms of Equation (2.14) gives, term by term,

$$\overline{\frac{\partial}{\partial t}\left(\overline{u_i}+u_i'\right)} = \frac{\partial}{\partial t}\left(\overline{\overline{u_i}+u_i'}\right) = \frac{\partial}{\partial t}\left(\overline{u_i}\right) \tag{2.15}$$

$$\begin{aligned}\overline{-\frac{\partial}{\partial x_j}\left(\left(\overline{u_i}+u_i'\right)\left(\overline{u_j}+u_j'\right)\right)} &= -\frac{\partial}{\partial x_j}\left(\overline{\overline{u_i}\,\overline{u_j}+\overline{u_i}u_j'+u_i'\overline{u_j}+u_i'u_j'}\right)\\ &= -\frac{\partial}{\partial x_j}\left(\overline{u_i}\,\overline{u_j}+\overline{u_i'u_j'}\right)\end{aligned} \tag{2.16}$$

$$\overline{-\frac{1}{\overline{\rho}}\frac{\partial}{\partial x_i}\left(\overline{p}+p'\right)} = -\frac{1}{\overline{\rho}}\frac{\partial}{\partial x_i}\left(\overline{\overline{p}+p'}\right) = -\frac{1}{\overline{\rho}}\frac{\partial}{\partial x_i}\left(\overline{p}\right) \tag{2.17}$$

$$\overline{\varepsilon_{ij3}f\left(\overline{u_j}+u_j'\right)} = \varepsilon_{ij3}f\,\overline{u_j} \tag{2.18}$$

$$\overline{-\delta_{i3}\left(1-\frac{\theta'}{\overline{\theta}}\right)g} = -\delta_{i3}g \tag{2.19}$$

$$\overline{\nu\nabla^2\left(\overline{u_i}+u_i'\right)} = \nu\nabla^2\left(\overline{\overline{u_i}+u_i'}\right) = \nu\nabla^2\overline{u_i} \tag{2.20}$$

Collecting all these terms back together results in, with some rearranging,

$$\frac{\partial\overline{u_i}}{\partial t} = -\overline{u_j}\frac{\partial\overline{u_i}}{\partial x_j} - \frac{1}{\overline{\rho}}\frac{\partial\overline{p}}{\partial x_i} + \varepsilon_{ij3}f\,\overline{u_j} - \delta_{i3}g + \nu\nabla^2\overline{u_i} - \frac{\partial}{\partial x_j}\left(\overline{u_i'u_j'}\right). \tag{2.21}$$

This has the same form as the incompressible form of the original Navier-Stokes, Equation (2.1), with the variables replaced by their mean values, and, crucially, with an extra turbulence term at the end. Hence, in the turbulent boundary layer, the turbulence has an effect on the mean quantities. The extra term represents a frictional drag, and can be described as the divergence of turbulent momentum flux [12], introducing a *Reynolds shear stress*, $\tau_{ij,\text{Reynolds}}$,

$$-\frac{\partial}{\partial x_j}\left(\overline{u_i'u_j'}\right) = \frac{1}{\overline{\rho}}\frac{\partial}{\partial x_j}\tau_{ij,\text{Reynolds}}, \tag{2.22}$$

$$\tau_{ij,\text{Reynolds}} = -\overline{\rho}\,\overline{u_i'u_j'}. \tag{2.23}$$

As it can be seen that turbulent momentum flux affects the mean wind speed in the boundary layer of the atmosphere, the next step is finding how a wind profile in this region of the atmosphere will look.

2.1.5 The logarithmic wind profile

In order to move from the turbulent momentum flux term in the atmosphere,derived to be Equation (2.22), to a wind profile in the lower boundary layer, further assumptions and approximations about the conditions in this region must be made.

One such approximation is introducing *K-theory*, also called gradient transport theory. In this framework, kinematic turbulent fluxes are assumed to be the product of a constant and the gradient of the mean value of the fluctuating variable[6] [14]. This yields

$$\overline{u_i' u_j'} = -K_m \frac{\partial \overline{u_j}}{\partial x_i}, \tag{2.24}$$

where K_m is a constant[7].

Another assumption that can be made about the atmospheric boundary layer, is that the mean motion is horizontally homogeneous [11]. Then the mean velocity in the $x_3 = x$ direction, $\overline{u_3} = \overline{w}$, is zero. Furthermore, the gradient of the mean velocities $\overline{u_1} = \overline{u}$ and $\overline{u_2} = \overline{v}$ in the $x_1 = x$ and $x_2 = y$ directions must zero as well. This, by Equation (2.24), leaves only two cases where the turbulent flux affects the mean flow,

$$\overline{w'u'} = -K_m \frac{\partial \overline{u}}{\partial z} \qquad \text{and} \qquad \overline{w'v'} = -K_m \frac{\partial \overline{v}}{\partial z}. \tag{2.25}$$

As there is no qualitative difference between the two expressions in Equation (2.25) under isotropic turbulence, coordinates can be redefined to have x in the direction of the mean wind u. A characteristic velocity scale of turbulent motion can then be defined as

$$u_* = \sqrt{-\overline{w'u'}} = \sqrt{\frac{\tau_{\text{Reynolds}}}{\overline{\rho}}}. \tag{2.26}$$

u_* is commonly called the *friction velocity*, as it represents the turbulent shear stress, the Reynolds stress, near the surface [11].

The constant, K_m, near the surface is only horizontally constant. It is proportional to the characteristic velocity and length scales of the turbulent *eddies* that are responsible for the turbulent momentum flux. In the *surface layer*[8] of the boundary layer, these eddies have characteristic length scales that have been found to be proportional to the elevation above the surface [11]. This thus satisfies the no-slip condition with no vertical turbulence at the ground level, where both the mean and turbulent velocities approach zero. The resulting expression for K_m in this region becomes

[6] This is qualitatively analogous to molecular diffusion. Experiments have shown, however, that the constant related to the turbulent flux in the boundary layer is many orders of magnitude greater than the corresponding molecular diffusion constant [11]. Thus the turbulent flux is the main source of drag on the mean flow in this region.

[7] K_m might generally be thought of as two-dimensional tensor of constants, where the constant might be different for different directions. For isotropic turbulence, however, the constant will be equal for turbulent dispersion of all components in all directions. Here isotropic turbulence is assumed

[8] The surface layer is estimated to typically comprise the lowest 15% of the boundary layer, meaning it typically extends several hundred meters above the surface [11].

$$K_m = \kappa u_* z, \tag{2.27}$$

with $\kappa = 0.40$ being the Von Kármán constant [10].

Inserting Equation (2.27) and Equation (2.26) into Equation (2.25) yields a differential equation relating the horizontal mean wind velocity with the elevation above ground, the Von Kármán constant, and the friction velocity:

$$u_* = \kappa z \frac{\partial \overline{u}}{\partial z}. \tag{2.28}$$

Equation (2.28) can then be integrated to obtain a wind profile. The mean horizontal wind can be integrated from where it is zero, $\overline{u}(z_0) = 0$ to $\overline{u}(z)$. Here z_0 is the *roughness parameter* of the surface, which relates to how high above the surface the wind speed is zero[9]. Correspondingly the elevation can be integrated from $z = z_0$ to $z - d$, with d being a *displacement height*. This displacement height is the zero-level elevation in case structures on the ground (like plants) cause the elevation from where it is sensible to define a starting height for the wind profile to differ from the ground level. The roughness parameter, z_0, is then defined as the height above d [14]. This yields the logarithmic wind profile[10],

$$\overline{u}(z) = \frac{u_*}{\kappa} \ln\left(\frac{z-d}{z_0}\right). \tag{2.29}$$

Of special interest is using a known wind speed at one height, and scaling it to the wind speed at another height using this wind profile. When $\overline{u}(z_1)$ is known a height z_1 above a surface with roughness parameter z_0 and displacement height d, Equation (2.29) gives that the mean horizontal velocity a height z_2 above the same surface is

$$\overline{u}(z_2) = \overline{u}(z_1) \frac{\ln((z_2-d)/z_0)}{\ln((z_1-d)/z_0)}. \tag{2.30}$$

Equation (2.30) will be central to estimating wind turbine power production in the modeling of an energy system using historical weather data.

2.2 Compression work on hydrogen

To find the energy needed for a hydrogen compressor to compress produced gas from a production pressure to the current pressure in a hydrogen storage tank, the following approximate expressions are used.

[9] The surface roughness parameter is typically between 10^{-6} meters and 10^{-1} meters for common surfaces, and values are given in tables [10].

[10] This wind profile is only accurate for *neutral* stability conditions. In that case air parcels will not move vertically unprovoked, but not resist movement either. For stable conditions (air parcels will resist vertical movement and fall back into place if moved vertically) and unstable conditions (air parcels will continue to move vertically if they begin to alter height) an extra term must be included into the logarithm [10]. For the purposes of this project, neutral stability conditions are assumed.

2.2.1 The compressibility factor

A simplified equation of state for a gas can be expressed as the *ideal gas law*, Equation (2.6), which can be rewritten as

$$pV = nRT. \tag{2.31}$$

Here p, V, and T are the pressure, volume, and temperature of the gas, respectively. Furthermore, n is the number of moles of the gas, and R is the universal gas constant [11]. Though this expression describes the case of a monatomic gas at low pressures and/or high temperatures well [15], the compression of the diatomic hydrogen gas leads to situations that deviate significantly from this law.

A way to account for such deviations is to introduce a *compressibility factor, Z* to Equation (2.31) [16], giving

$$pV = nRTZ. \tag{2.32}$$

This compressibility factor is then the ratio of the actual volume of a gas to the volume calculated from the ideal gas law; $Z(p,T) = \dfrac{V_{\text{actual}}}{V_{\text{ideal}}(p,T)}$, and it is seen that the factor is a function of both pressure and temperature.

The compressibility factor for hydrogen has been studied extensively, and measurements have been used to develop empirical equations for the value. One such equation is the *Lemmon equation* [17],

$$Z(p,T) = 1 + \sum_{i=1}^{9} a_i \left(\frac{100\text{K}}{T}\right)^{b_i} \left(\frac{p}{1\text{MPa}}\right)^{c_i}, \tag{2.33}$$

where T is in kelvin and p is in megapascal, and the constants for a_i, b_i, and c_i as given in Table 2.1 [12].

The resulting hydrogen gas compressibility factor for the relevant pressure and temperature ranges is displayed in Figure 2.2. It can be observed that the compressibility factor is relatively close to unity for low pressures and low temperatures, low pressures and high temperatures, and high pressures and high temperatures, which is where the ideal gas law approximates gas behavior well. For high pressures and low temperatures, however, the compressibility factor increases rapidly and deviates significantly from unity.

[11] The universal gas constant has the (exact) value $R = 8.31446261815324\ \text{Jmol}^{-1}\text{K}^{-1}$ in SI units [11].

[12] The hydrogen densities obtained from the Lemmon equation are within 0.01% of their actual values in the temperature range from 220 K to 1000K and pressure range from 0 MPa to 70 MPa. The expression is further accurate to within 0.15% for temperatures down to 150 K and pressures up to 200 MPa. This accuracy is considered sufficient for the use cases in this work.

Table 2.1: Constants for the Lemmon equation

i	a_i	b_i	c_i
1	0.05888460	1.325	1.0
2	-0.06136111	1.87	1.0
3	-0.002650473	2.5	2.0
4	0.002731125	2.8	2.0
5	0.001802374	2.938	2.42
6	-0.001150707	3.14	2.63
7	0.9588528×10^{-4}	3.37	3.0
8	$-0.1109040 \times 10^{-6}$	3.75	4.0
9	0.1264403×10^{-9}	4.0	5.0

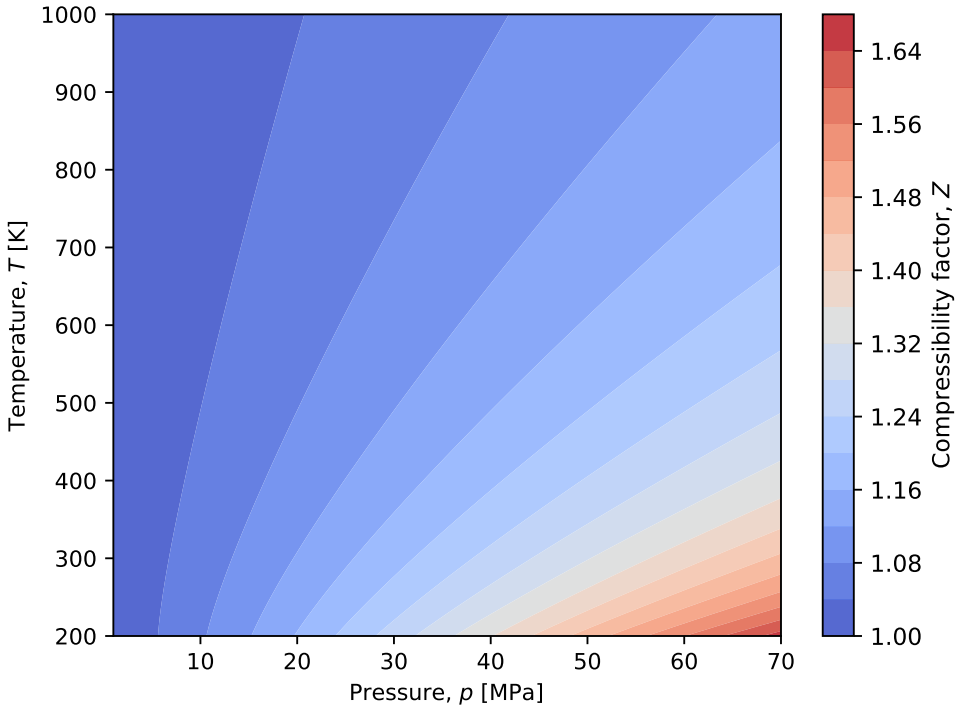

Figure 2.2: The compressibility factor, $Z(p, T)$ for hydrogen gas for the temperature range from 200 K to 1000 K and pressure range from 1 MPa to 70 MPa, shown as a two dimensional contour plot.

2.2.2 Isothermal compression

Compressing a gas isothermally requires the least amount of external work, as no work leads to increasing the internal energy of the gas. Hence, such compression is strived towards in many compressor designs [16]. The work required to compress an ideal gas isothermally from a state "1" to a state "2" is [16]

$$W_{\text{iso,ideal}} = \int_{V_1}^{V_2} p\mathrm{d}V = nRT \int_{V_1}^{V_2} \frac{1}{V}\mathrm{d}V = nRT\ln\left(\frac{V_1}{V_2}\right) = nRT\ln\left(\frac{p_2}{p_1}\right). \quad (2.34)$$

Here Equation (2.31) was used with T constant.

Due to the deviation from unity of the compressibility factor of hydrogen as the pressure increases, this simplified expression will deviate from the actual work required to isothermally compress the gas. Figure 2.3 shows how the compressibility factor increases, almost linearly, with pressure for three temperatures. As expected from Figure 2.2, the increase in compressibility is less for higher temperatures.

By choosing very small pressure differences, the compressibility factor can be approximated by the average of the compressibility factors related to the initial and final pressures, $Z_{\text{avg}} = \frac{1}{2}(Z(p_1, T_1) + Z(p_2, T_2))$. The resulting compression

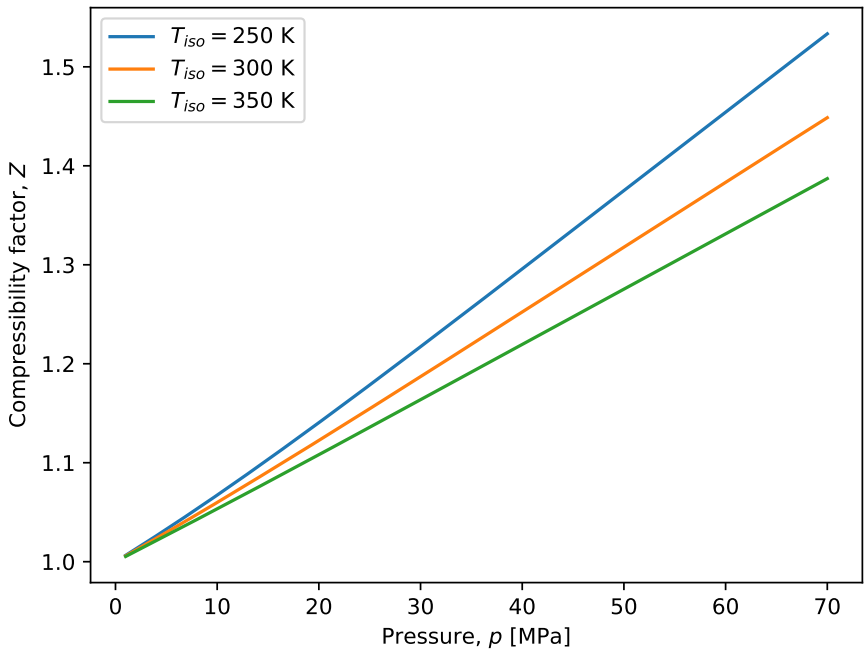

Figure 2.3: The compressibility factor of hydrogen from 1 MPa to 70 MPa along isothermal compression for three different temperatures; 250 K, 300 K, and 350 K.

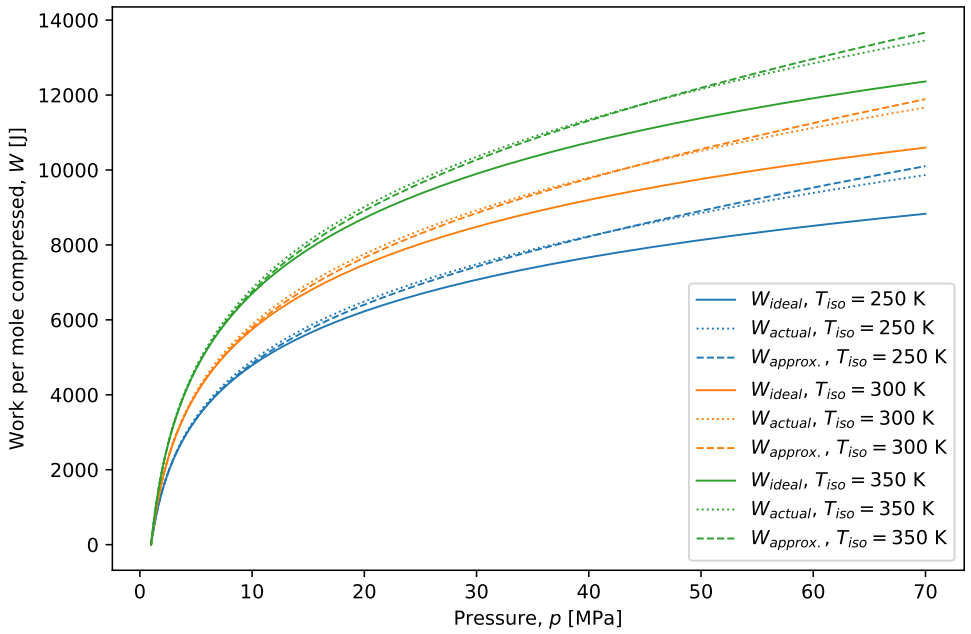

Figure 2.4: The work done for isothermal compression per mole of gas from 1 MPa to a pressure of up to 70 MPa. Three different temperature cases are considered; 250 K, 300 K, and 350 K. For each case, three different calculations are done; the ideal gas approximation, the actual work calculated from the varying compressibility factor along the pressure increase, and an approximation using only the initial and final compressibility factor.

work can be expressed as

$$W_{\text{iso,actual}} \approx nRT \sum_i Z_{\text{avg},i} \ln\left(\frac{p_{i+1}}{p_i}\right), \tag{2.35}$$

where the it summed over arbitrarily small increments in p to obtain the desired precision.

In addition, for later use, an approximation for the actual compression work using only the pressure values at the initial and final states is found. This is done by multiplying Equation (2.34) by Z_{avg} and replacing each pressure p_i in the argument of the logarithm by $p_i/Z(p_i, T_i)$, yielding

$$W_{\text{iso,approx}} = nRT Z_{\text{avg}} \ln\left(\frac{p_2 Z(p_1, T)}{p_1 Z(p_2, T)}\right). \tag{2.36}$$

The calculated compression work per mole of gas using Equation (2.34), Equation (2.35), and Equation (2.36) for the three temperature cases of 250 K, 300 K, and 350 K are shown in Figure 2.4.

It can be seen that for isothermal compression of these pressures and temperatures the approximation using only initial and final compressibility factor values

is a much better fit to the actual work required to compress the gas than the ideal gas assumption, and consequently the former approximation will be used in this work.

2.2.3 Adiabatic compression

An actual compression stage is usually closer to *adiabatic*[13] than isothermal [16]. An adiabatic process is characterized by satisfying the *adiabatic equation of state* [15],

$$p_1 V_1^{\gamma} = p_2 V_2^{\gamma}, \qquad \gamma = \frac{C_p}{C_V}, \tag{2.37}$$

where γ, called the *adiabatic index*, is the ratio of the heat capacity at constant pressure and the heat capacity at constant volume for the gas[14]. Equation (2.37) yields $V = V_1 \left(\frac{p_1}{p}\right)^{\frac{1}{\gamma}}$ and the work required to compress an ideal gas adiabatically from state "1" to state "2" becomes [16]

$$\begin{aligned} W_{\text{ad,ideal}} = \int_{p_1}^{p_2} V\,dP &= V_1 p^{\frac{1}{\gamma}} \frac{1}{1-\frac{1}{\gamma}} \left(p_2^{\,1-\frac{1}{\gamma}} - p_1^{\,1-\frac{1}{\gamma}} \right) \\ &= nRT_1 \frac{\gamma}{\gamma-1} \left(\left(\frac{p_2}{p_1}\right)^{\frac{\gamma-1}{\gamma}} - 1 \right). \end{aligned} \tag{2.38}$$

As for the isothermal case, however, the varying compressibility factor will cause the actual required work to deviate from the ideal assumption. Following the same procedure to obtain the actual compression work requires knowing the compressibility factor after a small pressure increase. Since a small pressure increase also causes a temperature increase in the adiabatic case, and since the compressibility factor is a function of both temperature and pressure, an approximation for the new temperature is found by inserting Equation (2.32) into Equation (2.37) and rearranging to

$$T_{2,\text{new}} = T_1 \frac{Z(p_1, T_1)}{Z(p_2, T_2)} \left(\frac{p_2}{p_1}\right)^{\frac{\gamma-1}{\gamma}}. \tag{2.39}$$

By starting with $T_2 = T_1$ and iterating over Equation (2.39) until $T_{2,\,new}$ is within desired proximity of T_2, the new temperature after adiabatically increasing the pressure a small amount is found. Having both the pressure and temperature along adiabatic compression then gives the compressibility factor for this process. This factor is shown for the three starting temperatures 250 K, 300 K, and 350 K in Figure 2.5. As for the isothermal case, the factor approaches being linear for

[13] Due to a reversible, adiabatic process also being isentropic, it is also common to call this *isentropic compression*.

[14] For hydrogen gas, the adiabatic index, also called the *isentropic expansion factor* is $\gamma \approx 1.41$ [16].

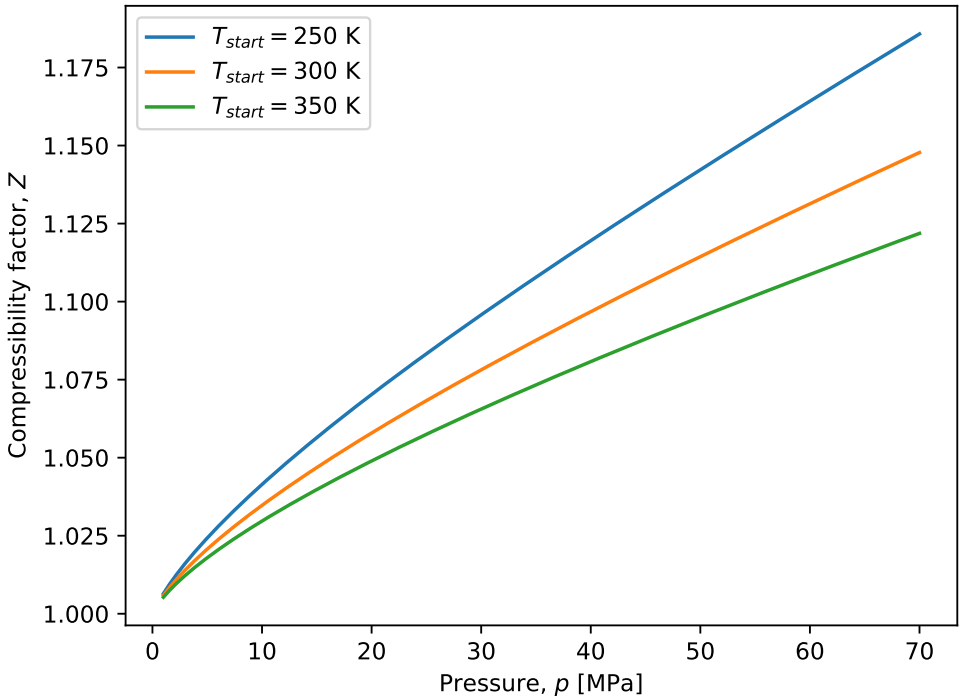

Figure 2.5: The compressibility factor of hydrogen from 1 MPa to 70 MPa along adiabatic compression for three different starting temperatures; 250 K, 300 K, and 350 K.

higher temperatures, but the magnitude is significantly lower in this case. This is expected from Figure 2.2 showing the compressibility factor decreasing with increased temperature, as is the case when adiabatically increasing pressure.

Using this further gives Z_{avg} for that small change of state, and the actual adiabatic compression work can be expressed as

$$W_{\text{ad,actual}} \approx nR\frac{\gamma}{\gamma-1}\sum_i T_i Z_{\text{avg},i}\left(\left(\frac{p_{i+1}}{p_i}\right)^{\frac{\gamma-1}{\gamma}}-1\right). \tag{2.40}$$

As for the isothermal case, an approximation for the actual compression work using only the pressure values at the initial and final states is found. This is done by estimating the final temperature from Equation (2.39), and from this obtaining an approximate value for Z_{avg}. Multiplying Equation (2.38) by this value yields [18]

$$W_{\text{ad,approx}} = nRT_1 Z_{\text{avg}}\frac{\gamma}{\gamma-1}\left(\left(\frac{p_2}{p_1}\right)^{\frac{\gamma-1}{\gamma}}-1\right). \tag{2.41}$$

The calculated compression work per mole of gas using Equation (2.38), Equation (2.40), and Equation (2.41) for the three initial temperature cases of 250 K,

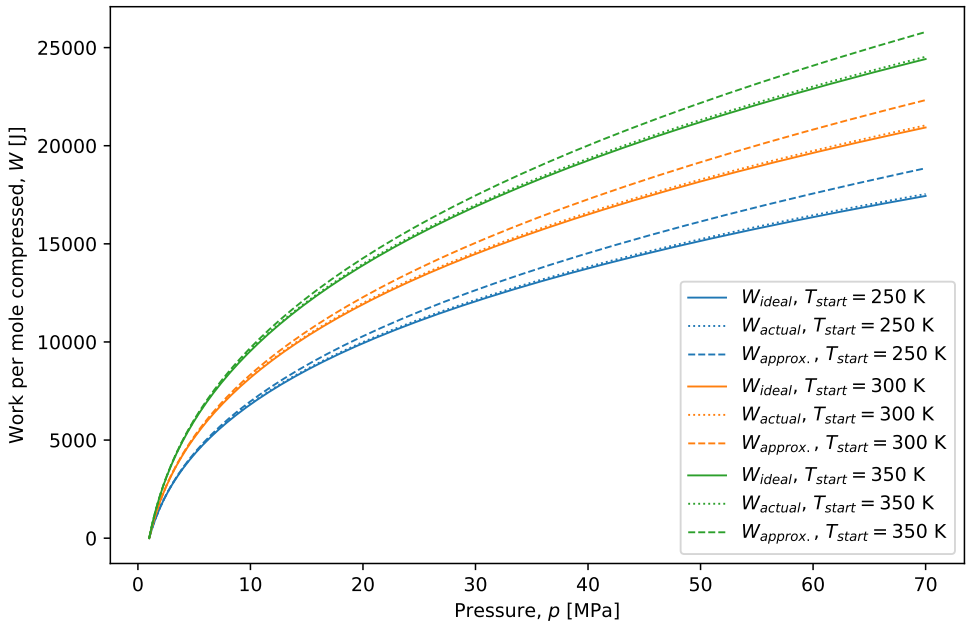

Figure 2.6: The work done for adiabatic compression per mole of gas from 1 MPa to a pressure of up to 70 MPa. Three different starting temperature cases are considered; 250 K, 300 K, and 350 K. For each case, three different calculations are done; the ideal gas approximation, the actual work calculated from the varying compressibility factor along the pressure and temperature increase, and an approximation using only the initial and final compressibility factor.

300 K, and 350 K are shown in Figure 2.6.

It can be seen that for adiabatic compression of these pressures and temperatures the ideal gas assumption gives a much better fit to the actual work required to adiabatically compress the gas than the approximation using only initial temperature and initial and final pressure values. The compressibility factor being much closer to unity for the adiabatic domain than the isothermal cases gives reason for the ideal gas assumption being more valid for the adiabatic compression. Further in this work, the ideal gas assumption will thus be used for the adiabatic case.

2.2.4 Comparison of isothermal and adiabatic compression work

The isothermal and adiabatic energy required to compress a gas will constitute the lower and upper limits, respectively, of the amount of energy an actual compressor must impress on the gas [16]. Both of these curves for the initial temperatures of 300 K and 350 K are shown in Figure 2.7.

It is evident that adiabatic compression requires nearly twice as much energy as isothermal compression does. The work a compressor does on the gas will depend on the design and potentially multi-stage setup of the compressor.

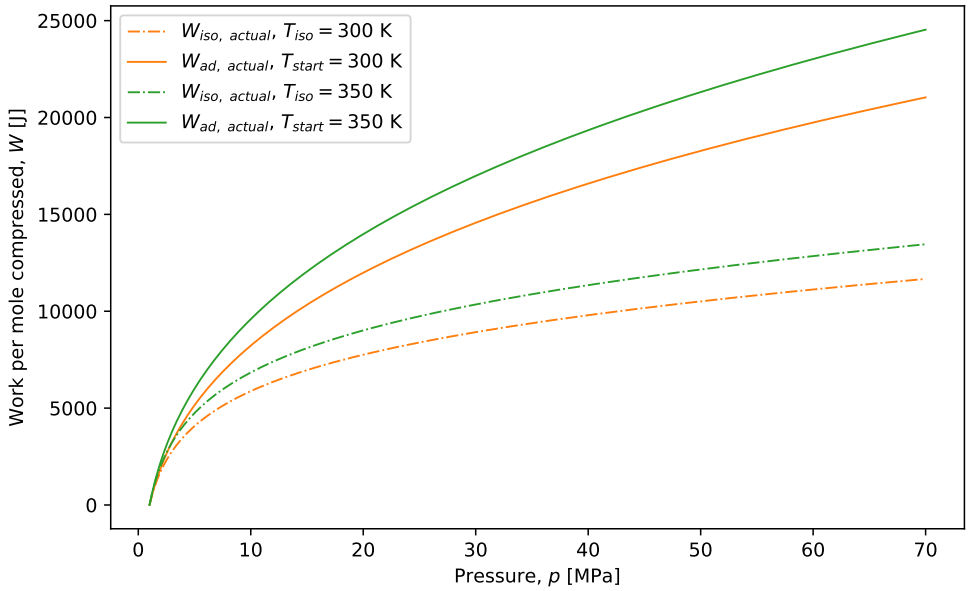

Figure 2.7: The isothermal and adiabatic compression work per mole of gas compressed from 1 MPa to a pressure of up to 70 MPa for the two highest temperature cases considered above. The work on the gas supplied by an actual compressor will be in between the isothermal and adiabatic limits.

Chapter 3

Modeling an integrated electricity and heating system using Oogeso

The *Offshore Oil and Gas Energy System Optimisation (Oogeso)* simulation tool is an open-source python package written by Harald G. Svendsen et. al. [19], and the code is available as a GitHub repository [20]. The tool is in this work expanded to model the off grid settlement of Longyearbyen on Svalbard[1].

3.1 The optimization problem to be solved

The energy system in Longyearbyen needs to satisfy electricity and heating demands using the available sources implemented. Currently the system relies on the coal power plant for both of these, with diesel systems as a backup. While these sources for energy production are fully controlled, future renewable energy sources, like wind and solar, may be intermittent, necessitating short and long term energy storage. At any point there may then be several sources that could be used to meet the power demand, and both the current and future energy storage situation and the predicted intermittent energy production in the future become variables in finding the optimal energy mix. There may also be different parameters one wants to optimize, like minimizing costs or CO_2 emissions.

Oogeso defines this optimization parameter as the *objective function* in a *mixed-integer linear programming (MILP)* optimization problem with a rolling horizon. The constraints to the problem are defined by creating a *network* of *nodes* containing *devices*, with *edges* in between the nodes. Each device has a set of constant *parameters* and a set of *optimization variables* that can be tuned for each timestep in the simulation. Using these parameters and optimization variables, a set of constraints that must be fulfilled for each device is defined for all timesteps. In the

[1]Despite the name, Oogeso is also suitable to model and simulate renewable energy systems of onshore, off grid energy systems.

following, only the devices, parameters, and optimization variables relevant for the Longyearbyen energy system are mentioned. For the comprehensive list see the related paper [21] or the open-source code [20].

An example of such an energy network is illustrated in Figure 3.1. The nodes are marked by grey rectangles, while there are double arrows representing the edges between nodes. Each edge carries the *flow* of electricity or heat from one node to another. Within each node the devices are illustrated as white rounded boxes with the top text being the *name* of the device and the bottom text being the *type* of the device. Each device has input and output flows of energy or energy carriers, and the device constraints restrict these flows.

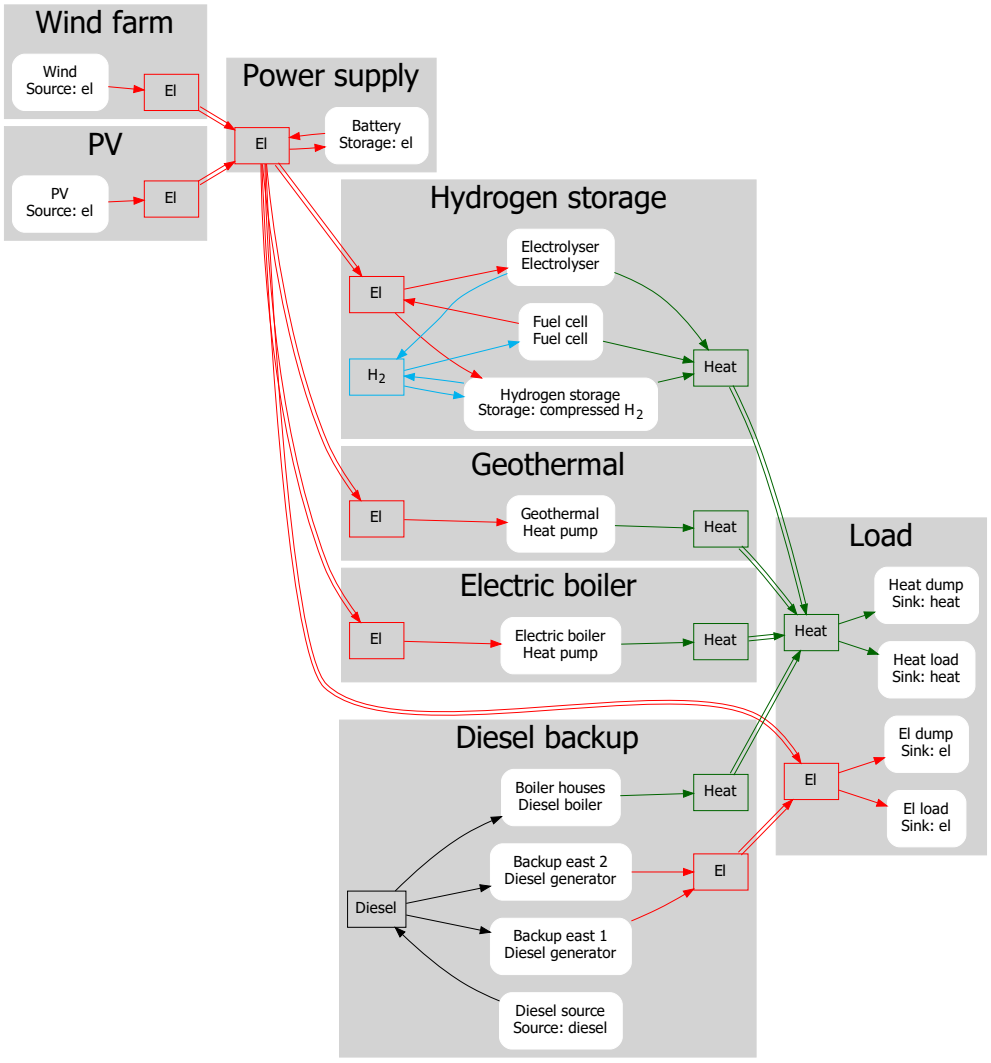

Figure 3.1: An example of an energy system network in Oogeso. Electricity (red), heat (green), hydrogen (blue), and diesel (black) can flow within nodes (single arrows) and on edges connecting nodes (double arrows).

In all cases discussed here, the objective function will be the cost of operating the energy system, which should be minimized. The optimization to be done for each optimization step is then[2]

$$\text{minimize} \sum_{d \in \mathbb{D}} \sum_{t \in \mathbb{T}} P(d,t), \tag{3.1}$$

such that all constraints are satisfied [21].

In Equation (3.1) the first sum is over all devices d in the set of devices, $\mathbb{D}$, while the second sum is correspondingly over all timesteps t in the set of timesteps in the optimization horizon[3], $\mathbb{T}$. $P(d,t)$ is a *penalty function* that gives the cost for each timestep for the device d. It can depend on the variables like the *flow* $f_{i,c}$ in the flow direction i of the energy carrier[4] c that is flowing. It can also depend on binary variables[5] like y_{on} and y_{start}, which state whether the device is on and whether the device is starting up, respectively. Such a function can then include variable operation and maintenance (O&M) costs and startup costs, the specifics of which are defined in the constraints for each device.

In the following there will be a brief explanation of the existing Oogeso features used in this work, followed by an explanation of the implementations added to simulate some potential renewable Longyearbyen energy system cases.

3.2 Existing Oogeso features and devices used

This section briefly outlines the relevant parts of the setup of the optimization system. There are more parameters, variables, constraints, and functions to ensure all devices operate as outlined. A good understanding of the workings of the network to be optimized is given, however, and the implementation details are available in the python package [20].

The relevant global simulation parameters used are,

- Δt: The length of each timestep in the simulation.
- t_{H}: The number of timesteps used in the optimization horizon.
- t_{between}: The number of timesteps in between each optimization.
- r_{min}: The minimum electrical power reserve required in case of unforeseen power losses or needs.
- c_{CO_2}: The CO_2 emission cost factor.

[2]The Oogeso framework contains further parameters and optimization variables that enter into the general cost objective function, but only the ones used in the simulated cases are displayed here.

[3]The *optimization horizon* is the collection of the current and the future timesteps that are taken into account when optimizing the objective function.

[4]Electricity and heat are considered energy "carriers" in this expression.

[5]Binary optimization variables are represented by the letter "y" in the rest of this chapter.

A global constraint that must be satisfied is that the sum of reserve electrical power $r(d,t)$ for all devices d must be greater than or equal to the minimum electrical power reserve parameter r_{min} for all timesteps t,

$$\left(\sum_{d\in\mathbb{D}} r(d,t)\right) \geq r_{\text{min}} \quad \forall \quad t \in \mathbb{T}. \tag{3.2}$$

3.2.1 A generic device

Each device *type* has its own set of parameters, variables, constraints, and input and output carrier flows. The relevant parameters shared among all devices are listed here.

- **Id**: The identifier, or name, of the device.
- **Node id**: The identifier, or name, of the node the device is located at.
- **Model**: The model, or type, of device.
- **Profile**: The name of the profile, pr, specifying the maximum flow at each timestep.
- f_{min}: The minimum flow of the device when it is on.
- f_{max}: The maximum flow of the device when it is on.
- $c_{\text{O\&M}}$: The variable operational and maintenance cost factor.
- c_{start}: The startup cost factor.
- c_{r}: The fraction of the unused power capacity that counts toward the electrical power reserve.

The variables and their valid domain[6] that apply to all devices are as follows,

- $f_{i,c}$, $\mathbb{R}^+$: The flows in and out of the device for all energy carriers.
- y_{on}, $\mathbb{Z}_2$: Whether the device is on or off.
- y_{start}, $\mathbb{Z}_2$: Whether the device is starting.

For each device a default flow variable, f, is specified as the flow in or out of a specific energy carrier. Using the parameters and variables, a set of constraints for each device in the flow network are implemented. The relevant constraints applying to all devices are,

[6] $\mathbb{R}^+$ signifies that the variable can take all nonnegative real values. $\mathbb{Z}_2$ signifies that the variable can take all values in the set of integers modulo 2, which is the set of binary values: $\{0,1\}$.

- $f \leq y_{\text{on}} \cdot f_{\text{max}} \cdot pr$:
  If the device is off, the default flow variable must be zero. Otherwise, this flow variable must not exceed the maximum flow parameter times the profile value for the timestep[7], if present.
- $f \geq y_{\text{on}} \cdot f_{\text{min}}$:
  If the device is on, the default flow variable must not be lower than the minimum flow parameter.

To satisfy the global electrical reserve constraint, a calculation of the device electrical reserve is done by finding the difference of the maximum electrical output power from the device and subtracting the actual output power.

$$r = c_r \cdot f_{\text{max}} \cdot pr - c_r \cdot f_{\text{out,el}}. \tag{3.3}$$

A value used in the objective function is the average[8] variable O&M cost for the horizon. For the generic device, this is defined as the corresponding cost factor times the default flow variable, averaged over all timesteps in the horizon.

$$\text{O\&M}_{\text{cost}} = \frac{1}{t_{\text{H}}} \sum_{t \in \mathbb{T}} c_{\text{O\&M}} \cdot f. \tag{3.4}$$

The objective function also depends on the average startup costs. While the O&M cost parameter is per time unit, the startup cost parameter is per timestep, and the corresponding cost calculation is consequently divided by the length of a timestep to obtain a comparable value to the O&M cost calculation,

$$\text{startup}_{\text{cost}} = \frac{1}{t_{\text{H}} \cdot \Delta t} \sum_{t \in \mathbb{T}} c_{\text{start}} \cdot y_{\text{start}}(t). \tag{3.5}$$

Another value used in the objective function is the average CO_2 cost for the horizon. For the generic device, the value 0 is returned.

3.2.2 Energy carrier sources

There are several energy carrier source devices implemented, but the only one used here is the electric power source. In addition to the generic device, the electric power source has electricity as the output carrier flow, and this is also set to be the default flow variable, $f_{\text{out,el}}$.

[7] All variables and time-dependent parameters listed in these constraint lists are implicitly assumed to be for the current timestep, so $f(t)$ is written as f. In the case that a constraint depends on several timesteps, the time is explicitly included for all members of the constraint.

[8] While average values over the optimization horizon are used in the objective function, the actual values at each timestep are also computed after the simulation to be used in the discussion of different simulation cases.

3.2.3 Energy carrier sinks

The sink devices are where energy carriers terminate. Here the electricity sink has electricity as the input carrier flow and default flow variable, $f_{\text{in,el}}$, while the heat sink has heat as the input carrier flow and default flow variable, $f_{\text{in,heat}}$.

3.2.4 Electrical energy storage

An electrical energy storage device, like a battery, has electricity as both input and output energy carriers, and the default flow variable is the electric output, $f_{\text{out,el}}$. The device has several additional parameters, variables, and constraints on top of the ones inherited from the generic device, with the parameters relevant for this work being,

- E_{min}: The minimum energy storage level.
- E_{max}: The maximum energy storage level.
- E_{init}: The initial energy storage level.
- η: The efficiency of converting electrical energy to stored energy.

The added optimization variables along with their domains are,

- E, $\mathbb{R}^+$: The energy storage level.
- P_{max}, $\mathbb{R}^+$: The maximal electric power the storage device can supply at each timestep.

The resulting constraints for the electrical energy storage device are then,

- $\left(f_{\text{in,el}}(t) \cdot \eta - f_{\text{out,el}}(t)/\eta\right) \cdot \Delta t = E(t) - E(t-1)$:
  The change in energy stored in the device from the previous timestep to the current timestep equals the energy flow in or out during the timestep.
- $E_{\text{min}} \leq E \leq E_{\text{max}}$:
  The amount of stored energy must be within the lower and upper energy bounds.
- $f_{i,\text{el}} \leq f_{\text{max}}$:
  Both the flow in and out of the device must be smaller than the maximum flow parameter.
- $P_{\text{max}} = \min\left(f_{\text{max}}, \frac{E}{\Delta t}\right)$:
  The maximum power the energy storage device can supply for a timestep is the smallest of the maximum flow parameter, and the current energy storage level divided by the length of the timestep[9].

3.2.5 Heat pump

The heat pump device converts electricity to heat, and consequently has electricity as the input energy carrier and heat as the output energy carrier. The default flow variable is set to be the input electricity flow, $f_{\text{in,el}}$.

There is one parameter in addition to the generic device,

- η: The efficiency of converting electrical energy to heat energy.

With no additional variables, there is one extra constraint to this device,

- $f_{\text{out,heat}} = f_{\text{in,el}} \cdot \eta$:
  The heat output equals the electricity input times the conversion efficiency.

3.2.6 Hydrogen system

The hydrogen gas energy carrier has an additional parameter compared to the other energy carriers mentioned thus far,

- c_{E}: The energy density of the hydrogen energy carrier.

Electrolyser

The electrolyser device has electricity as the input carrier flow, and hydrogen and heat as output carrier flows. The default flow variable is the input electricity, $f_{\text{in,el}}$.

The additional parameters defined for this device are,

- η: The efficiency of converting electrical energy to energy contained in hydrogen gas.
- η_{heat}: The efficiency of recovering the waste heat energy from electrolysis.

There are no extra variables, and the added device constraints are,

- $f_{\text{out,hydrogen}} \cdot c_{\text{E}} = f_{\text{in,el}} \cdot \eta$:
  The output hydrogen gas flow times the hydrogen energy density must equal the input electricity flow times the electrolyser efficiency.
- $f_{\text{out,heat}} = f_{\text{in,el}} \cdot (1 - \eta) \cdot \eta_{\text{heat}}$:
  The output heat flow must equal the input electrical energy not converted to hydrogen energy times the waste heat recovery efficiency.

[9] To convert this constraint to linear expressions, the *Big-M* approach is used to decompose the constraint to four linear inequality constraints with an additional binary variable [22].

Fuel cell

The fuel cell device has hydrogen as the input carrier flow, and both electricity and heat as output carrier flows. The default flow variable is the output electricity, $f_{\text{out,el}}$.

The additional parameters defined for this device are,

- η: The efficiency of converting hydrogen gas energy to electrical output flow.
- η_{heat}: The efficiency of recovering the waste heat energy from the fuel cell.

There are no extra variables, and the added device constraints are,

- $f_{\text{out,el}} = f_{\text{in,hydrogen}} \cdot c_{\text{E}} \cdot \eta$:
  The output electricity flow must equal the input hydrogen flow times the hydrogen energy density times the fuel cell efficiency.
- $f_{\text{out,heat}} = f_{\text{in,el}} \cdot c_{\text{E}} \cdot (1-\eta) \cdot \eta_{\text{heat}}$:
  The output heat flow must equal the input hydrogen energy not converted to electrical energy times the waste heat recovery efficiency.

3.3 Devices implemented in Oogeso as part of this work

To simulate and compare different variations of potential new energy systems in Longyearbyen, additions were made to some devices in the model, while several new devices were also implemented. The code for this model is available at its own GitHub branch [23].

A global simulation parameter that has been added is,

- $r_{\text{min,heat}}$: The minimum heat power reserve required in case of unforeseen power losses or needs.

Correspondingly, a global constraint that must be satisfied is that the sum of reserve heat power $r_{\text{heat}}(d,t)$ for all devices d must be greater than or equal to the minimum heat power reserve parameter $r_{\text{min,heat}}$ for all timesteps t,

$$\left(\sum_{d \in \mathbb{D}} r_{\text{heat}}(d,t)\right) \geq r_{\text{min,heat}} \quad \forall \quad t \in \mathbb{T}. \tag{3.6}$$

3.3.1 Additions to the generic device

Several parameters have been added to the generic device, listed here,

- $c_{\text{r,heat}}$: The fraction of the unused heat output capacity that counts toward the heat power reserve.
- $c_{\text{O\&M,fixed}}$: The fixed operational and maintenance cost factor.
- $c_{\text{investment}}$: The investment cost factor.
- c_{lifetime}: The lifetime of the investment.

The three last parameters are not used in the optimization itself, but are used to compare investment, fixed, and variable costs for different devices and configurations for an energy system after simulating it.

Analogously to the global electric reserve parameter and constraint, the global heat reserve parameter and constraint is implemented for the model to be able to ensure that a minimum reserve heat power is available for all timesteps. The reserve heat power for each timestep for each device will be the total amount of heat power the device can supply, minus the heat power that is already supplied, multiplied by the $c_{\text{r,heat}}$ parameter of the device.

This reserve heat power calculation utilizes different parameters depending on device properties, and the main variants are implemented in the generic device calculation. While the calculation only applies to devices having heat as an output carrier, the term calculating the total amount of heat power the device *can* supply is different for different devices due to the f_{max} parameter relating to electricity flow if the device has electricity as an energy carrier, and heat flow if electricity is not present.

If electricity is an *output* energy carrier of the device, the maximum heat flow is the max electricity flow times share of the input energy not converted to electricity times the heat recovery efficiency. This gives the heat reserve as,

$$r_{\text{heat}} = c_{\text{r,heat}} \left(f_{\text{max}} \cdot pr \cdot \frac{1-\eta}{\eta} \cdot \eta_{\text{heat}} - f_{\text{out,heat}} \right). \tag{3.7}$$

If electricity on other hand is an *input* carrier, there are two cases; either the device produces heat as a byproduct and has the η_{heat} parameter, or the device has heat production as its primary function with η being the production efficiency. The two cases give,

$$r_{\text{heat}} = c_{\text{r,heat}} \left(f_{\text{max}} \cdot pr \cdot (1-\eta) \cdot \eta_{\text{heat}} - f_{\text{out,heat}} \right). \tag{3.8}$$

$$r_{\text{heat}} = c_{\text{r,heat}} \left(f_{\text{max}} \cdot pr \cdot \eta - f_{\text{out,heat}} \right). \tag{3.9}$$

The final case, where no electric carrier is involved, will have the default flow variable be the heat output, simply yielding,

$$r_{\text{heat}} = c_{\text{r,heat}} \left(f_{\text{max}} \cdot pr - \cdot f_{\text{out,heat}} \right). \tag{3.10}$$

3.3.2 Diesel system

As the current backup energy system in Longyearbyen, which is planned to be used as both a transitional energy system and a future backup system, is fully diesel-based, diesel devices are implemented into the optimization model. Firstly, the diesel energy carrier is added, with the following parameters,

- c_{E}: The energy density of the diesel energy carrier.
- ρ_{CO_2}: The CO_2 density of the diesel energy carrier.

Diesel generator

The main diesel device used in the current system is the diesel generator, which has diesel as the input energy carrier, and electricity and heat as output energy carriers. The default flow variable is the output electricity, $f_{\mathrm{out,el}}$, and the device has the following additional parameters,

- A_{fuel}: The fuel parameter scaling with output electric power.
- B_{fuel}: The fuel parameter independent of output electric power.
- η: The efficiency of the generator at maximum electricity generation.
- η_{heat}: The efficiency of the waste heat recovery.

The way the diesel generator device calculates fuel usage is based on the assumption of the delivered power being a linear function of the input diesel amount. This also gives the inverse relation of fuel usage being possible to write as a linear function of the power output, with dimensionless constants, as

$$\frac{f_{\mathrm{in,diesel}} \cdot c_{\mathrm{E}}}{f_{\mathrm{max}}} = A_{\mathrm{fuel}} \cdot \frac{f_{\mathrm{out,el}}}{f_{\mathrm{max}}} + B_{\mathrm{fuel}}. \tag{3.11}$$

The generator efficiency at maximum power, which is used in the heat reserve calculation, is then found as $\eta = \dfrac{1}{A_{\mathrm{fuel}} + B_{\mathrm{fuel}}}$.

The constraints for the diesel generator device are then,

- $\dfrac{f_{\mathrm{in,diesel}} \cdot c_{\mathrm{E}}}{f_{\mathrm{max}}} = A_{\mathrm{fuel}} \cdot \dfrac{f_{\mathrm{out,el}}}{f_{\mathrm{max}}} + B_{\mathrm{fuel}}$:
  The relation between fuel consumption and output power must hold.
- $f_{\mathrm{out,heat}} = \left(f_{\mathrm{in,diesel}} \cdot c_{\mathrm{E}} - f_{\mathrm{out,el}}\right) \cdot \eta_{\mathrm{heat}}$:
  The output heat flow equals the diesel energy not converted to electricity, times the waste heat recovery factor.

Diesel boiler

The other diesel device added to the model is the diesel boiler, which has diesel as the input energy carrier and heat as the output energy carrier. The default flow variable is set to be the heat output, $f_{\text{out,heat}}$, and a single additional parameter is set,

- η: The efficiency of extracting usable heat energy from diesel.

The device also only has one additional constraint,

- $f_{\text{out,heat}} = f_{\text{in,diesel}} \cdot c_{\text{E}} \cdot \eta$:
  The heat energy output equals the efficiency factor times the energy contained in the diesel input.

Since usage of both the diesel generator and diesel boiler devices directly produce CO_2 emissions, the carbon dioxide flow calculation is modified for both device types to read,

$$f_{\text{CO}_2} = \frac{1}{t_{\text{H}}} \sum_{t \in \mathbb{T}} c_{\text{E}} \cdot f_{\text{in,diesel}}. \tag{3.12}$$

3.3.3 Compressed hydrogen storage

Another new device implemented into the model is compressed hydrogen storage, which is an extension of the existing hydrogen storage device using the theory of compression work on hydrogen from Section 2.2. To implement compression into the model, a few more parameters for the hydrogen energy carrier must be defined,

- ρ: The density of the hydrogen gas energy carrier.
- M: The molar mass of hydrogen gas.
- γ: The adiabatic index, being the ratio of heat capacity at constant pressure to the heat capacity at constant volume, of the hydrogen gas.

The compressed hydrogen storage device has electricity and hydrogen as input energy carriers, and heat and hydrogen as the output energy carriers. The default flow variable is the hydrogen output, $f_{\text{out,hydrogen}}$, and the additional device parameters are,

- **Target profile**: The name of the target profile, pr_{profile}, giving the storage level target at each timestep.
- $c_{\text{belowtarget}}$: The cost parameter for the storage level being below the target value.
- E_{min}: The minimum energy storage level.
- E_{max}: The maximum energy storage level.
- E_{init}: The initial energy storage level.
- η: The share of the hydrogen gas input that ends up as stored energy.
- $\eta_{\text{compressor}}$: The energy efficiency of the hydrogen compressor.
- $\eta_{\text{heat,compressor}}$: The efficiency of waste heat recovery from hydrogen compression.
- $T_{\text{compressor}}$: The initial temperature of the hydrogen to be compressed.
- $p_{\text{in,compressor}}$: The pressure of the hydrogen input to the compressor.
- $p_{\text{max,compressor}}$: The maximum pressure of the hydrogen storage tanks.
- $c_{\text{iso,ad,compressor}}$: The coefficient stating how close the compression is to the isothermal ($c_{\text{iso,ad,compressor}} = 0$) and adiabatic ($c_{\text{iso,ad,compressor}} = 1$) limits.

The added optimization variables along with their domains are,

- E, $\mathbb{R}^+$: The energy storage level.
- $E_{\text{compressor}}$, $\mathbb{R}$: The energy per time required for compression to the tank pressure in the previous timestep.
- $E_{\text{compressor,iso}}$, $\mathbb{R}$: The energy per time associated with isothermal compression or expansion to the tank pressure in the previous timestep.
- $P_{\text{compressor,iso}}$, $\mathbb{R}^+$: The actual electricity demand needed for isothermal compression to the tank pressure in the previous timestep.
- $y_{\text{below target}}$, $\mathbb{Z}_2$: A binary variable denoting whether the storage level is below the target profile value or not.

To create the constraints for this device, the hydrogen compression work must be defined in terms of the parameters and variables listed above.

The amount of gas in the hydrogen storage containers is, $n = \frac{E \cdot \rho}{M}$, giving the volume of the storage containers as

$$V = \frac{E_{\text{max}} \cdot \rho}{M} \cdot \frac{Z\left(p_{\text{max}}, T_{\text{compressor}}\right) R T_{\text{compressor}}}{p_{\text{max}}}, \tag{3.13}$$

where R is the universal gas constant and $Z\left(p_{\text{max}}, T_{\text{compressor}}\right)$ is found using the Lemmon equation, Equation (2.33), for the compressibility factor of hydrogen.

The pressure, p_{init}, in the hydrogen tank at the beginning of a timestep is then found by first considering the ideal gas case, $p_0 = \frac{nRT_{\text{compressor}}}{V}$. This yields a compressibility factor $Z\left(p_0, T_{\text{compressor}}\right)$, and a new estimate for the pressure is $p = p_0 \cdot Z\left(p_0, T_{\text{compressor}}\right)$. By setting $p_0 = p$ and iterating over the last two steps; finding a new compressibility factor and a new pressure estimate, the initial pressure can be estimated to arbitrary precision[10]. The initial pressure is then denoted p_{init}, and the corresponding compressibility factor is denoted as $Z_{\text{init}} = Z\left(p_{\text{init}}, T_{\text{compressor}}\right)$.

It is then estimated that the additional hydrogen gas added to the storage in a single timestep is small compared to the full storage capacity, meaning that the compressibility factor of the isothermally compressed additional gas will be approximately equal to Z_{init}. Furthermore, this assumption yields that compressing the additional gas to p_{init} gives a good approximation of the required work.

The isothermal compression work required to compress the additional hydrogen gas flowing into the compressed storage in one timestep is then approximately, as found in Equation (2.36),

$$W_{\text{iso}} = \frac{f_{\text{in,hydrogen}} \cdot \Delta t \cdot \rho}{M} RT_{\text{compressor}} \frac{Z_{\text{in}} + Z_{\text{init}}}{2} \ln\left(\frac{p_{\text{init}} Z_{\text{in}}}{p_{\text{in,compressor}} Z_{\text{init}}}\right), \quad (3.14)$$

where $Z_{\text{in}} = Z\left(p_{\text{in,compressor}}, T_{\text{compressor}}\right)$ is the compressibility factor of the hydrogen gas flowing into the compressor.

Similarly, the adiabatic compression work is approximately, as found in Equation (2.38),

$$W_{\text{ad}} = \frac{f_{\text{in,hydrogen}} \cdot \Delta t \cdot \rho}{M} RT_{\text{compressor}} \frac{\gamma}{\gamma - 1}\left(\left(\frac{p_{\text{init}}}{p_{\text{in}}}^{\frac{\gamma-1}{\gamma}}\right) - 1\right). \quad (3.15)$$

The hydrogen compressor energy demand is then,

$$W_{\text{compressor}} = (1 - c_{\text{iso,ad,compressor}}) \cdot W_{\text{iso}} + c_{\text{iso,ad,compressor}} \cdot W_{\text{ad}}. \quad (3.16)$$

This value is linearly dependent on the optimization variable $f_{\text{in,hydrogen}}$.

[10] In this implementation the iteration is stopped when the new pressure $p = p_0 \cdot Z\left(p_0, T_{\text{compressor}}\right)$ deviates from p_0 by less than 1%.

The constraints for the compressed hydrogen storage device thus become,

- $\left(f_{\text{in,hydrogen}}(t) \cdot \eta - f_{\text{out,hydrogen}}(t)/\eta\right) \cdot \Delta t = E(t) - E(t-1)$:
  The difference between effective hydrogen flow in and out must equal the change in hydrogen storage level.
- $E_{\min} \leq E \leq E_{\max}$:
  The hydrogen storage level must be in between the lower and upper bounds.
- $\dfrac{pr_{\text{target}} - E}{E_{\max}} \leq y_{\text{below target}}$:
  This and the following constraint ensure that the binary variable $y_{\text{below target}}$ is set to 1 if the storage level is below the target profile value.
- $y_{\text{below target}} - 1 \leq \dfrac{pr_{\text{target}} - E}{E_{\max}} \cdot y_{\text{below target}}$:
  If the storage level is above the target profile value, $y_{\text{below target}}$ is set to 0.
- $E_{\text{compressor}} \cdot \eta_{\text{compressor}} = W_{\text{compressor}}/\Delta t$:
  $W_{\text{compressor}}/\Delta t$ gives the power associated with compressing or expanding the additional gas to the pressure currently in the storage tanks.
- $f_{\text{in,el}} = \max\left(0, E_{\text{compressor}}\right)$:
  The compressor will not expend any electrical energy to let gas *expand* in the storage[11]. This constraint is implemented using the Big-M approach with 3 linear constraints and one extra binary variable.
- $f_{\text{in,hydrogen}}$ and $f_{\text{out,hydrogen}}$ are not nonzero simultaneously:
  Hydrogen is not simultaneously flowing into and out from the storage device. This constraint is implemented using the Big M approach with three linear constraints and two extra binary variables.
- $E_{\text{compressor,iso}} \cdot \eta_{\text{compressor}} = W_{\text{iso}}/\Delta t$:
  $W_{\text{iso}}/\Delta t$ gives the power associated with compressing or expanding the additional gas isothermally to the pressure currently in the storage tanks.
- $P_{\text{compressor,iso}} = \max\left(0, E_{\text{compressor,iso}}\right)$:
  The required compressor compressor power usage is zero in the case of the gas expanding when placed in storage. This is implemented using the Big M approach with 3 linear constraints and one extra binary variable.
- $f_{\text{out,heat}} = \left(f_{\text{in,el}} - P_{\text{compressor,iso}}\right) \cdot \eta_{\text{heat}}$:
  The output heat flow equals the difference between the compressor power and the isothermal compressor power, times the waste heat recovery efficiency[12].

[11] The gas does not need compression in the cases where $p_{\text{in}} \geq p_{\text{init}}$.
[12] The waste heat from maintaining an isothermal compression is assumed to not be recovered.

To incentivize keeping the energy storage level above the target storage level, a function giving a cost if the storage is below the target at the end of the optimization horizon is defined using the parameters and variables defined for this device,

$$\mathrm{E}_{\mathrm{cost}} = \frac{1}{t_{\mathrm{H}}} \cdot c_{\text{below target}} \cdot \big(E - pr_{\text{target}}(t + t_{\mathrm{H}})\big) \cdot y_{\text{below target}}. \tag{3.17}$$

3.4 Final objective function

Combining all of the above device types yield the following objective function,

$$\sum_{d \in \mathbb{D}} \sum_{t \in \mathbb{T}} \big(\mathrm{O\&M}_{\mathrm{cost}}(d,t) + \mathrm{startup}_{\mathrm{cost}}(d,t) + E_{\mathrm{cost}}(d,t) + c_{\mathrm{CO}_2} \cdot f_{\mathrm{CO}_2}(d,t)\big). \tag{3.18}$$

The optimization task is then to minimize Equation (3.18) for every optimization horizon such that all the constraints for every device are satisfied. The full, modified python code is available on GitHub [23].

The Oogeso optimization model creates a set of linear constraints that must all be satisfied, with the objective function being an expression, linear in every variable, that must be minimized. The task of solving this mixed integer linear program is done by an external numerical solver. Oogeso supports calling several common mathematical programming solver executables, and the one used in this work is Gurobi Optimizer [24].

Chapter 4

Energy system devices and data sources

While Longyearbyen is operated mainly by coal power today, the coal power plant is planned to be decommissioned by the end of 2023 [5]. The data related to the different existing, planned, and possible future alternative energy sources is outlined in the following. These are parameter values used in the extended Oogeso optimization model discussed in the previous chapter.

When choosing which devices to use to meet the demand of electricity and heat, the cost for doing so is minimized. While a full and accurate financial comparison of choosing different combinations of energy sources and storage options is outside of the scope of this work, some information about investment costs, fixed operational and maintenance costs (fixed O&M costs), and variable operational and maintenance costs (variable O&M costs) in 2022 NOK are provided for most devices if relevant. Unless otherwise stated, both this information and specific technology parameters like lifetime, efficiency, and minimum production levels are obtained from the technology data catalogue from the Danish Energy Agency (DEA) using the estimated 2030 values [1] [27].

For all cases, a CO_2-tax, c_{CO_2}, of 2 NOK per kilogram (2000 NOK per ton) is used, which is the political ambition for 2030 [28]. Furthermore, the modeled cases operate in timesteps, Δt, of 1 hour with a forecast horizon, t_H, of 240 timesteps (10 days) for the profile-dependent devices. The chosen optimization frequency, $t_{between}$, is every 24 timesteps, giving one optimization per day. Furthermore, both the minimum electrical reserve, r_{min}, and the minimum heating reserve, $r_{min,heat}$, are set to 5 MW. Unless stated in the following device descriptions, the fractions of unused electricity, c_r, and heat, $c_{r,heat}$, power that counts toward their respective reserve calculations are set to 0.

[1] In many cases, the financial data is initially given in 2015€, which is translated to 2022€ using an inflation value of 12.7%. In other cases, the initial financial data is given in 2020€, which is then translated to 2022€ using an inflation value of 8.8% [25]. The result is then converted to 2022 NOK using an exchange rate of 10.0 NOK/€ [26].

4.1 Existing diesel system

There is an existing diesel powered backup system already in place for the settlement of Longyearbyen. This system is planned to function as the transitional energy supply between the shutdown of the coal power plant and the finalization of a fully renewable solution [5]. There are thus no investment costs included relating to this system[2].

4.1.1 Diesel as an energy carrier

The energy content and CO_2 content of diesel are obtained from an energy and fuel data overview [29]. These values are given per normal cubic meter (Nm^3), which is the amount at the *normal* conditions of a temperature of 273.15 K (0°C) and a pressure of 101.3125 kPa (1 atmosphere)[3] [30]. A common way to measure the energy content of a fuel compound is the *higher heating value* (HHV), which is the energy produced by complete combustion of the fuel [31].

For the cost of the diesel, the value of 8033 NOK/Nm^3 is obtained from the THEMA report on Svalbard energy systems [7][4]. This cost includes transport of the fuel to Longyearbyen, as well as storage costs. Along with the fuel properties, this parameter is listed in Table 4.1.

Table 4.1: Diesel data used in the optimization model.

Parameter	Value	Unit
Energy content (HHV), c_E	37940	MJ/Nm^3
CO_2 content, ρ_{CO_2}	2629	kg/Nm^3
Cost, $c_{O\&M}$	7590	NOK/Nm^3

[2]There are politically approved refurbishments of the current diesel system that do have a significant cost, but since these are already underway, and necessary for all cases phasing in renewable sources, the costs are not included as *new* investment expenses.

[3]For a liquid fuel such as diesel, variations in pressure and temperature only minorly effect the density per volume properties. For hydrogen gas discussed later, however, the impact of temperature and pressure on volumetric density is of major importance. The convention of using normal cubic meters (Nm^3) for all volume measurements is thus adopted.

[3]Also sometimes called *gross calorific value* (GCV), *higher calorific value (HCV)*, and heat of combustion.

[4]The values given in this report are in estimated 2020 NOK, which have been converted to 2022 NOK using an inflation value of 5.84% [32].

Table 4.2: Diesel generator data used in the optimization model.

	Parameter	Value	Unit
Backup power east	Installed capacity, $f_{\max}$	3 × 1.8	MW
	Minimum load, $f_{\min}$	0.54	MW
	A_{fuel}	2.699	1
	B_{fuel}	0.1642	1
	Heat recovery efficiency, η_{heat}	0	%
	Electric reserve factor, c_{r}	100	%
Backup power west	Installed capacity	3 × 2.0	MW
	Minimum load	0.60	MW
	A_{fuel}	2.698	1
	B_{fuel}	0.1632	1
	Heat recovery efficiency, η_{heat}	60	%
	Electric reserve factor, c_{r}	100	%
	Heat reserve factor, $c_{\text{r,heat}}$	100	%
	Investment cost, $c_{\text{investment}}$	0	NOK/MW
	Fixed O&M cost, $c_{\text{O\&M,fixed}}$	0.003145	NOK/(MW · s)
	Variable O&M cost, $c_{\text{O\&M}}$	0.01878	NOK/(MW · s)

4.1.2 Diesel generators

There are two small diesel farms in Longyearbyen, the *Backup power east* with three 1.8 MW generators, and the *Backup power west* with three 2.0 MW generators [2]. The former was built in 2009, while the latter was recently finished in 2021. For both sites, a minimum load per generator of 30% of the rated capacity is assumed [27].

The diesel usage of the generators is assumed to be a linear function of the output power with two dimensionless coefficients, A_{fuel} and B_{fuel} as in Equation (3.11). These coefficients are typically different for different generator sizes, and data[5] from Generator Source [33] was used with linear regression to find values for the coefficients.

For the generators at Backup power west, a waste heat recovery system for the district heating system will be installed before the coal power plant is shut down. Such a system can reclaim 60% of the heat energy produced from diesel generators [34].

The diesel generator data[6] used in the Oogeso model is given in Table 4.2.

[5]For the western backup plant, data points for 2 MW generators were used, while for the eastern plant data points for 1.75 MW generators were used as estimates for the slightly larger generators at that site.

[6]The O&M data used here are the 2015 values (which also equal the 2020 values) from the Danish Energy Agency, as the system is already installed using existing components. (The 2030 estimates take into account estimated technological advancements reducing maintenance costs).

Table 4.3: Diesel boiler data used in the optimization model.

	Parameter	Value	Unit
Backup diesel boilers	Installed capacity, $f_{\max}$	2×8.5	MW
	Minimum load, $f_{\min}$	1.28	MW
	Efficiency (HHV), η	88	%
	Heat reserve factor, $c_{\text{r,heat}}$	100	%
Backup boiler houses	Installed capacity, $f_{\max}$	17.0	MW
	Minimum load, $f_{\min}$	0.18	MW
	Efficiency, η	87	%
	Heat reserve factor, $c_{\text{r,heat}}$	100	%
	Investment cost, $c_{\text{investment}}$	0	NOK/MW
	Fixed O&M cost, $c_{\text{O\&M,fixed}}$	0.0006204	NOK/(MW · s)
	Variable O&M cost, $c_{\text{O\&M}}$	0.003019	NOK/(MW · s)

4.1.3 Diesel boilers

Unless otherwise stated, the efficiency, load and cost data for the diesel boiler devices is acquired from the technology data for industrial process heat catalogue from the Danish Energy Agency (DEA)[7] [35].

There are two backup diesel boiler systems in place to cover district heating needs. In 2021 two 8.5 MW boilers were installed at the power plant, while there are six diesel boiler houses along the heating grid with a total power output of 17 MW [2]. For the latter, the smallest installation is 1.2 MW, while the largest is 4.5 MW [7]. Both systems are taken to have a minimum load of 15% of the smallest boiler capacity, while the large system at the power plant is assumed to have an HHV efficiency of 88%[8] [35]. The smaller boiler house installations are assumed to have the slightly lower efficiency of 87% found in smaller diesel boilers [36].

The diesel boiler data used in the Oogeso model is given in Table 4.3.

4.2 Battery

A modular battery system is under delivery and installation in Longyearbyen, and is planned to be an integrated part of the energy system from 2023 [37]. The battery will mitigate power demand spikes, and can in the future alleviate power demand while backup diesel generators are started up.

The battery pack will have a maximum power output of 6 MW, and a storage capacity of 7 MWh, while efficiency and cost data is obtained from the technology data catalogue for energy storage from the DEA [38]. This data used in the Oogeso model, is summarized in Table 4.4.

[7] The cost data is given in 2019€, which is converted to 2022€ using an inflation value of 8.71% [25].

[8] The data given in the DEA industrial heat catalogue has efficiencies for lower heating value (LHV), which is converted to HHV values by dividing by the diesel HHV/LHV factor of 1.063 [29].

Table 4.4: Battery data used in the optimization model.

Parameter	Value	Unit
Maximum power output, $f_{\max}$	6	MW
Storage capacity, $E_{\max}$	7	MWh
Efficiency, η	91	%
Electric reserve factor, c_{r}	100	%
Lifetime, c_{lifetime}	20	Years
Investment cost, $c_{\mathrm{investment}}$	0	NOK/MWh
Fixed O&M cost, $c_{\mathrm{O\&M,fixed}}$	0.0001930	NOK/(MW · s)
Variable O&M cost, $c_{\mathrm{O\&M}}$	0.006261	NOK/(MW · s)

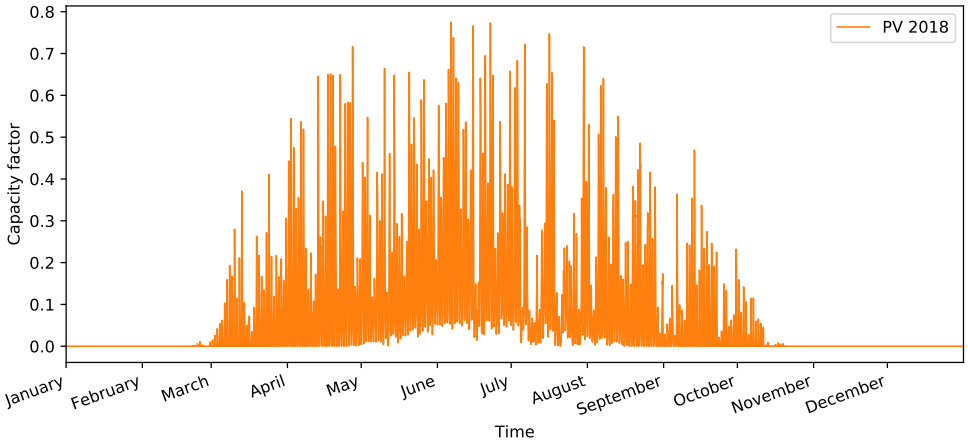

Figure 4.1: The hourly photovoltaic (PV) power capacity factors for Longyearbyen for 2018 calculated from the MERRA-2 reanalysis dataset.

4.3 Photovoltaic power

Solar power on Svalbard is already being utilized on for example the airport [39]. An advantage on the archipelago is that photovoltaic (PV) cells have an increasing efficiency with decreasing temperatures, making the power production in summertime an enticing option.

In addition, this power source can have a low local footprint, as panels can be mounted on walls and roofs of existing buildings in the town. A report from 2018 found the capacity for solar power on the roofs of Longyearbyen to be between 26.7 MWp[9] and 33.3 MWp, depending on the type of solar panel used. For the cases with photovoltaic power studied here, a conservative value of 25 MWp has been chosen as the fully installed capacity.

[9] *Megawatt-peak* (MWp) signifies the power produced by a photovoltaic cell under the standard conditions of an irradiation intensity of 1000 W/m, a cell temperature of 25°C, and a sun spectrum of AM1.5 [40].

Table 4.5: Photovoltaic (PV) data used in the optimization model.

Parameter	Value	Unit
Installed capacity, $f_{\max}$	25	MWp
Electric reserve factor, c_{r}	50	%
Lifetime, c_{lifetime}	40	Years
Investment cost, $c_{\mathrm{investment}}$	6156000	NOK/MWp
Fixed O&M cost, $c_{\mathrm{O\&M,fixed}}$	0.003048	NOK/(MWp · s)
Variable O&M cost, $c_{\mathrm{O\&M}}$	0.0	NOK/(MW · s)

The actual amount of solar irradiation in Longyearbyen at a given time is estimated from the MERRA-2 reanalysis dataset with data up to and including 2019 using the *Renewables.ninja* interface[10] [41] [42] [43]. The resulting capacity factors for the year 2018 are shown in Figure 4.1. As expected, there is no power production during the winter months, while in the summer months there is production at all times of the day. It is also interesting to note that the capacity factor never surpasses 80%, meaning the power production never surpasses 80% of the MWp of the installed photovoltaic cells. This is because of the lower solar irradiance in polar latitudes than for the standard conditions for solar panel ratings.

The photovoltaic (PV) data used in the Oogeso model, in addition to the capacity factor profile in Figure 4.1, is given in Table 4.5. Due to uncertainties in the forecasts of intermittent power production, the electric reserve factor for the PV installation is chosen to be a conservative 50%.

4.4 Wind power

A potential future renewable electricity source for Longyearbyen is local wind power. Though intermittent, it can provide power throughout the year, making it a suitable part of the energy mix in the future. The energy demands of the town that the future energy system needs to be able to cover is of limited scale, though, making a large offshore installation improbable. To see the effects of the greater winds typically experienced offshore, however, a case with such an installation is included. In all cases, the wind turbine parameters are obtained for the Vestas

[10]Hourly data from 2011 up to and including 2019 is obtained from this reanalysis model using the location for Longyearbyen (latitude 78.220 and longitude 15.645) with the default parameters of 10% system loss, and panels with no tracking having 35° panel tilt and facing at an azimuth of 180°.

V105 3.45 MW turbine [44]. This turbine is installed in both onshore and offshore wind farms, and has a robust design intended for harsh climatic conditions, making it a suitable candidate for analyzing wind power feasibility on Svalbard[11]. The turbine has a hub height[12] of 72.5 meters, a cut-in speed[13] of 3 meters per second, a cut-out speed[14] of 25 meters per second, and a re cut-in speed[15] of 23 meters per second. The power curve showing power output as a function of wind speed for the V105 turbine is displayed in Figure 4.2 [45].

This power curve is for the wind speed at wind turbine hub height. To translate measured wind speeds from the height of a weather station to the hub height, the logarithmic wind profile, Equation (2.30), is used. For all weather stations considered here, the ground is snow covered for the majority of the year, with negligible vegetation levels in the summer months. Correspondingly, the roughness parameter is taken to be $Z_0 = 0.005$ meters [46] and the displacement height is taken to be $d = 0$ meters.

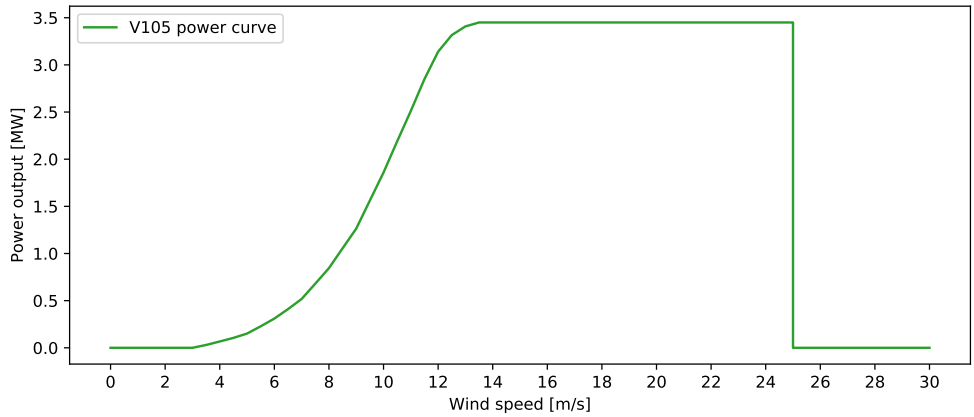

Figure 4.2: The produced power as a function of hub height wind speed for the Vestas V105 wind turbine.

[11]Other turbine models will likely better suit the wind conditions on Svalbard, but a timeseries of wind measurements at elevations up to the hub height for each potential wind farm location is needed to select the optimal wind turbine. In this work, the V105 is selected for its robustness, while it also gives a conservative estimate of possible wind power production at each location.

[12]The *hub height* is the height above the ground that the nacelle is mounted.

[13]The *cut-in speed* is the minimum wind speed at hub height at which the turbine can produce power.

[14]The *cut-out speed* is the wind speed at hub height at which the turbine stops and halts power generation.

[15]The *re cut-in speed* is the wind speed at hub height for which the turbine restarts power generation after having halted due to reaching the cut-out speed.

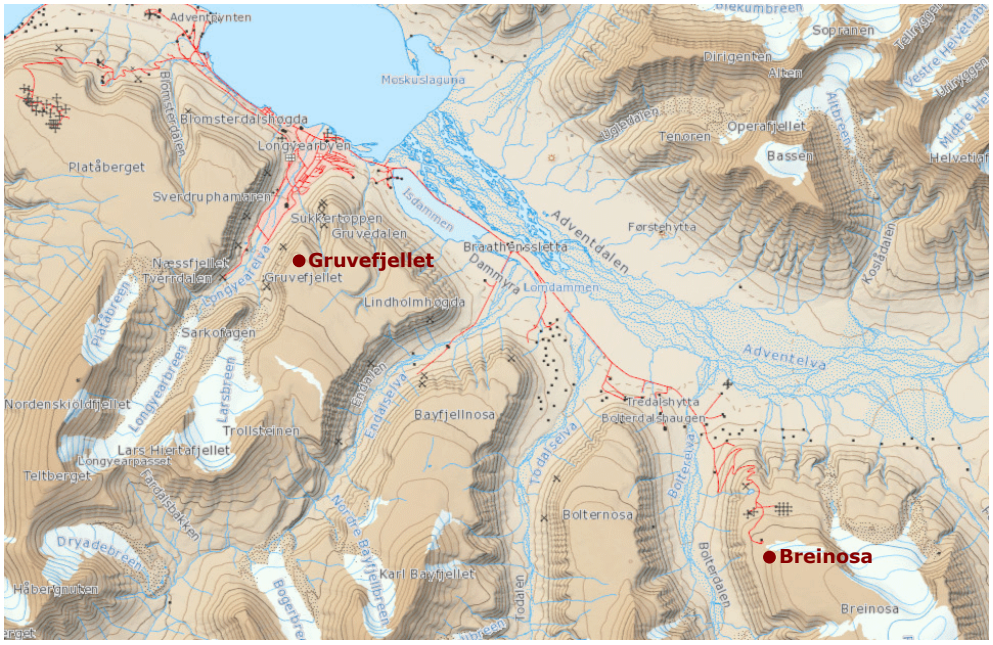

Figure 4.3: The location of two weather stations, *Breinosa* and *Gruvefjellet* in the area around Longyearbyen.

4.4.1 Onshore

There is a weather station on the Breinosa mountain, about 10 kilometers from the town, shown in Figure 4.3 [47]. The station has coordinates 78.148°N, 16.043°E, is located at 520 meters above sea level, and takes wind measurements 4 meters above ground level [48]. The surroundings consist of the current coal mine, *Gruve 7*, as well as the scientific installations of *EISCAT* and *Kjell Henriksen Observatory*. This region is thus already significantly industrialized, and deemed by Store Norske to be a suitable place to install an onshore wind farm.

Wind measurements from the Breinosa weather station are thus used in this work, along with Equation (2.30), to estimate the wind power output for a given turbine height. The resulting capacity factors for the year 2018 are displayed in Figure 4.4. Besides showing great variability in wind power production, the figure also displays long periods of continuous low production, necessitating large energy storage facilities and/or other power sources. The intermittency of onshore wind in the Longyearbyen area for the period from 2011 to 2019 has been studied before [49], and the year 2018 was found to be an average wind year for the capacity factors calculated from the Breinosa weather data.

It is still of interest to see how this capacity factor correlates with the corresponding capacity factor from the MERRA-2 reanalysis dataset. Using a hub height of 72.5 meters and the same coordinates as the Breinosa weather station for the year 2018, wind data is obtained from the Renewables.ninja API. Combining this data with the V105 wind turbine power curve yields the capacity factors based on

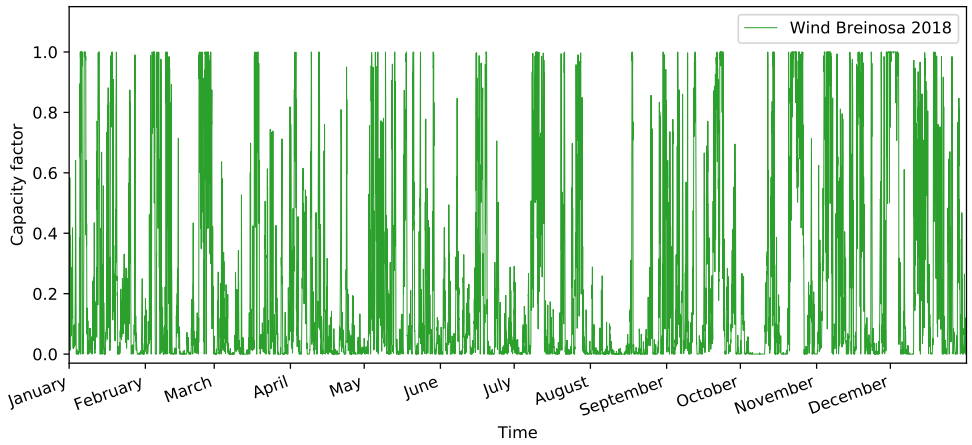

Figure 4.4: The hourly capacity factors for the Vestas V105 wind turbine at a hub height of 72.5 meters for the year 2018 for the Breinosa weather station location.

wind model data. Both this data based on wind data from ninja, and the previous capacity factor data based on actual wind measurements are shown as duration curves in Figure 4.5.

These duration curves show that the capacity factors calculated from wind measurement data is significantly higher than the case calculated from model wind data. For the measurement case, the average capacity factor over the year was 0.22, while it was only 0.16 for the model case. The wind speed timeseries in both cases showed the same trends, but the model wind speeds tend to be lower than the measured wind speeds scaled up to the hub height.

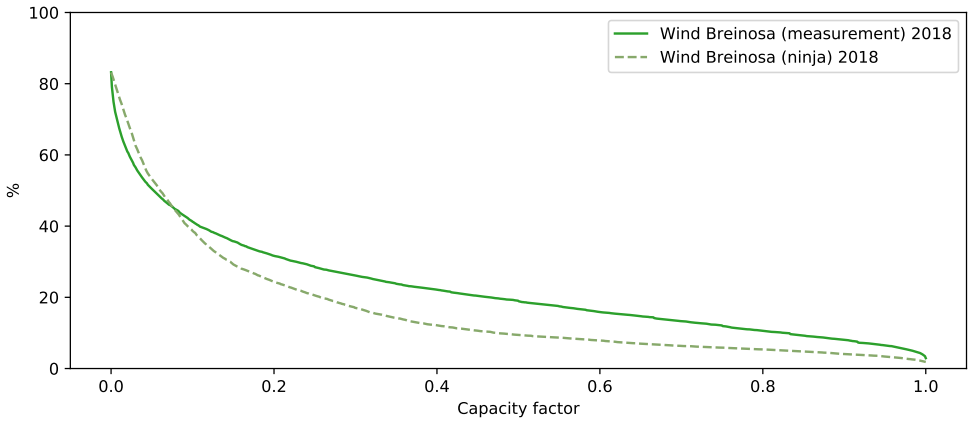

Figure 4.5: Duration curves for the capacity factors for the V105 wind turbine with a hub height of 72.5 meters at the Breinosa location in 2018 from both local wind measurement data and wind data from the Renewables.ninja API. The measurement-based data has a higher percentage of capacity factors above 0.1 than the model-based data.

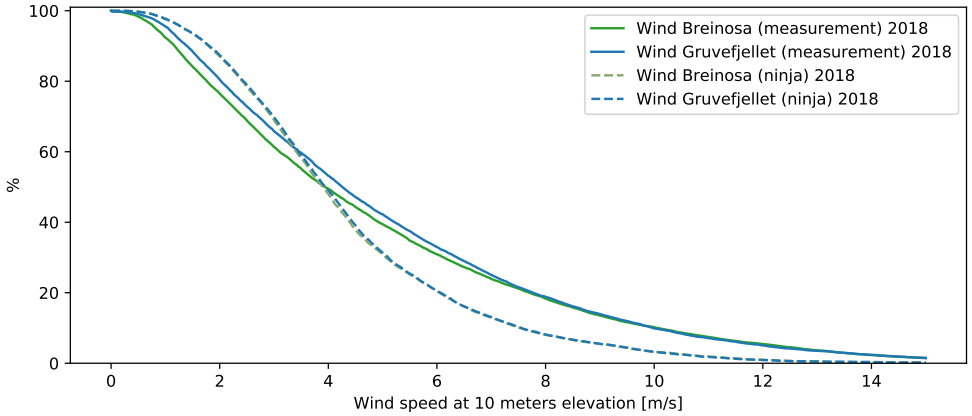

Figure 4.6: Duration curves for the wind speeds at 10 meters elevation in the year 2018 for the Breinosa and Gruvefjellet weather station locations. Both data from measurements and from the Renewables.ninja API are included.

To investigate this discrepancy, the MERRA-2 wind speeds at the lowest possible height of 10 meters were obtained from Renewables.ninja, and compared with the measured wind speeds scaled up from 4 meters to 10 meters using the logarithmic wind profile.

Since the Breinosa weather station is positioned on the northwest side of the Breinosa mountain, and thus possibly affected by the proximity to the much taller top, wind data from the measurement station at Gruvefjellet, shown in Figure 4.3, were also obtained. This weather station is located at 78.200°N, 15.624°E, at 464 meters above sea level, and gathers wind speed measurements at 2.8 meters above ground level [48]. As for the Breinosa data, values from Gruvefjellet were also scaled up to 10 meters using the logarithmic wind profile, and MERRA-2 data for those coordinates and elevation was obtained using the Renewables.ninja API. Because the Gruvefjellet weather station is located on a plateau with no nearby mountains affecting the wind, it might give a better representation of the wind patterns found closer to the top of Breinosa, where a potential onshore wind farm could be located.

Duration curves for all the four datasets were made for the year 2018, and are shown in Figure 4.6. Here it is evident that the model gives significantly lower wind speeds at 10 meters elevation than the actual measurements. Further, the model has very similar wind estimates for Breinosa and Gruvefjellet, while the measurements show slightly more wind measurements below 8 m/s on Gruvefjellet than on Breinosa. As the latter weather station is located in a more sheltered region, it is expected to measure lower wind speeds than the weather station located on a plateau.

With two comparable, on-site weather stations agreeing on wind conditions, the measured Breinosa wind data is chosen to be the basis for wind power output from an onshore wind farm.

Table 4.6: Onshore wind data used in the optimization model.

Parameter	Value	Unit
Installed capacity per turbine	3.45	MW
Electric reserve factor, c_r	50	%
Lifetime, c_{lifetime}	30	Years
Investment cost, $c_{\text{investment}}$	11720000	NOK/MW
Fixed O&M cost, $c_{\text{O\&M,fixed}}$	0.004503	NOK/(MW · s)
Variable O&M cost, $c_{\text{O\&M}}$	0.004226	NOK/(MW · s)

The onshore wind farm data used in the Oogeso model, in addition to the capacity factor profile in Figure 4.4, is given in Table 4.6. As for the photovoltaic device, the electric reserve factor is chosen to be 50% to account for forecast uncertainties.

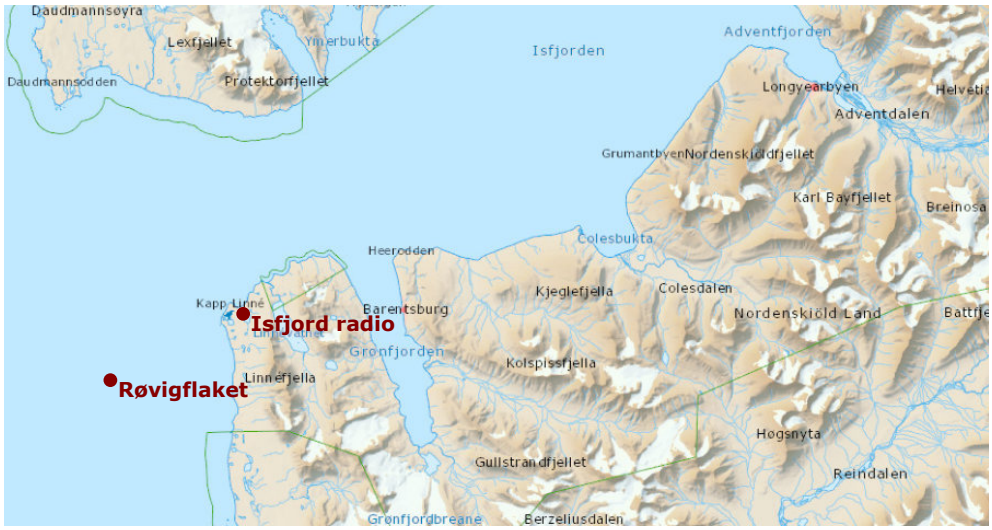

Figure 4.7: The location of the weather station at *Isfjord radio* about 50 kilometers west of Longyearbyen is shown, as well as the location of *Røvigflaket* 15 kilometers southwest of this weather station.

4.4.2 Offshore

Offshore wind farms benefit from more stable and favorable wind conditions that often are present at sea. On Svalbard, however, such wind farms have two main environmental drawbacks. An installation will industrialize an untouched region of the archipelago a significant distance away from existing industrialized areas, which is generally avoided in the Arctic region [50]. The other drawback is that offshore wind turbines will likely affect the very rich bird life surrounding the coastal areas in the summer months [51]. Hence, an offshore wind installation

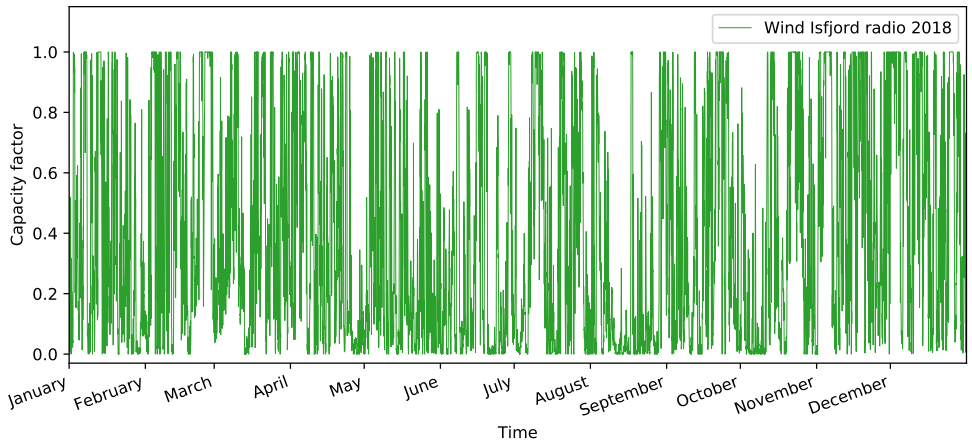

Figure 4.8: The capacity factors for the Vestas V105 wind turbine at a hub height of 72.5 meters in hourly resolution for the year 2018 for the Isfjord radio weather station location.

on Svalbard is likely not viable if other renewable energy sources with lower environmental impacts are feasible within a similar economic regime. To investigate the effect on the power production of the offshore wind conditions, however, data for such wind conditions are also obtained.

Fixed foundation offshore wind turbines are typically limited to a water depth of up to 50 meters [52]. The fjords around Longyearbyen with water depths of several hundreds of meters are thus unsuited, but there are some shallows on the west coast of Spitsbergen. Notably, *Røvigflaket* has large areas with a water depth of 30 meters or less. This location is about 65 kilometers from Longyearbyen along the fjords. 15 kilometers northeast of Røvigflaket there is a weather station at *Isfjord radio*. Both of these locations are shown in Figure 4.7 [47].

The weather station at Isfjord radio has coordinates 78.063°N, 13.619°E, is located at 7 meters above sea level, and takes wind measurements 10 meters above ground level [53]. It is next to the coast, and the surroundings are flat and free of obstructions in the form of hills or mountains in all directions for at least three kilometers[16]. The wind conditions are thus assumed to be similar to those 15 kilometers southwest of the weather station.

Wind measurements from Isfjord radio are scaled to the wind turbine hub height of 72.5 meters using Equation (2.30), and combined with the V105 power curve, Figure 4.2, to find the capacity factors, shown in Figure 4.8 for 2018. Although there is great variability in wind power production, high capacity factors are more frequent, and low production periods are shorter, than for the onshore data from the same time period.

As for the onshore case, it is of interest to see how this capacity factor correl-

[16]In fact, the closest point where the elevation has risen to 25 meters above sea level is over 2.5 kilometers away.

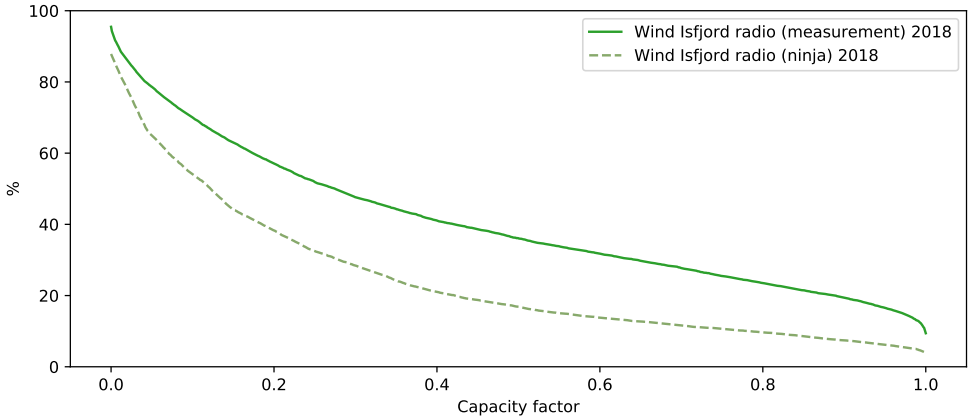

Figure 4.9: Duration curves for the capacity factors for the V105 wind turbine with a hub height of 72.5 meters at the Isfjord radio location in 2018 from both local wind measurement data and wind data from the Renewables.ninja API.

ates with the corresponding capacity factor from the MERRA-2 reanalysis dataset. Using a hub height of 72.5 meters and the coordinates of the Isfjord radio weather station for the year 2018, the Renewables.ninja API gives model wind data. Both the capacity factors based on this wind data from ninja, and the factors based on actual wind measurements are shown as duration curves in Figure 4.9.

A clear discrepancy is seen, with the percentage of measurement-based capacity factors greater than any value being much larger than the model-based capacity factors greater than the same value. For the measurement case, the average capacity factor over the year was 0.40, while it was only 0.24 for the model case. To look into this, the raw model wind data for Isfjord radio at 10 meters above

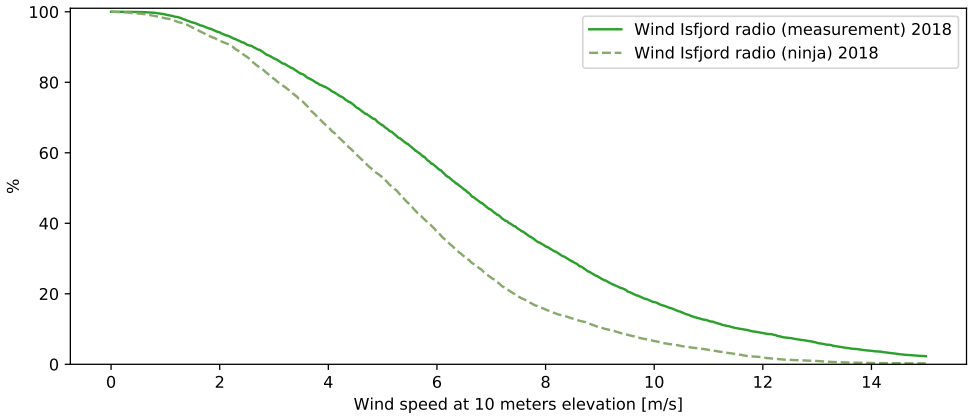

Figure 4.10: Duration curves for the wind speeds at 10 meters elevation in the year 2018 for the Isfjord radio weather station locations. Both data from measurements and from the Renewables.ninja API are included.

Table 4.7: Offshore wind data used in the optimization model.

Parameter	Value	Unit
Installed capacity per turbine	3.45	MW
Electric reserve factor, c_r	50	%
Lifetime, c_{lifetime}	30	Years
Investment cost, $c_{\text{investment}}$	19440000	NOK/MW
Fixed O&M cost, $c_{\text{O\&M,fixed}}$	0.01336	NOK/(MW · s)
Variable O&M cost, $c_{\text{O\&M}}$	0.01170	NOK/(MW · s)

ground level is obtained and compared with the actual wind measurements at the same height. Both cases, as duration curves, are shown in Figure 4.10.

It is evident that higher wind speeds are significantly more frequent in actual measurements, than predicted by the weather model at the same location and height[17].

The offshore wind farm data used in the Oogeso model is given in Table 4.6.

The measured wind data from Isfjord radio is chosen to be used for calculating the offshore wind power output, and consequently the capacity factors in Figure 4.8 enter as the profile in the model. Duration curves for both this capacity factor, and the onshore one, are shown in Figure 4.11. Here it is clear that an offshore installation will be able to utilize much more of the installed capacity more often than an onshore installation.

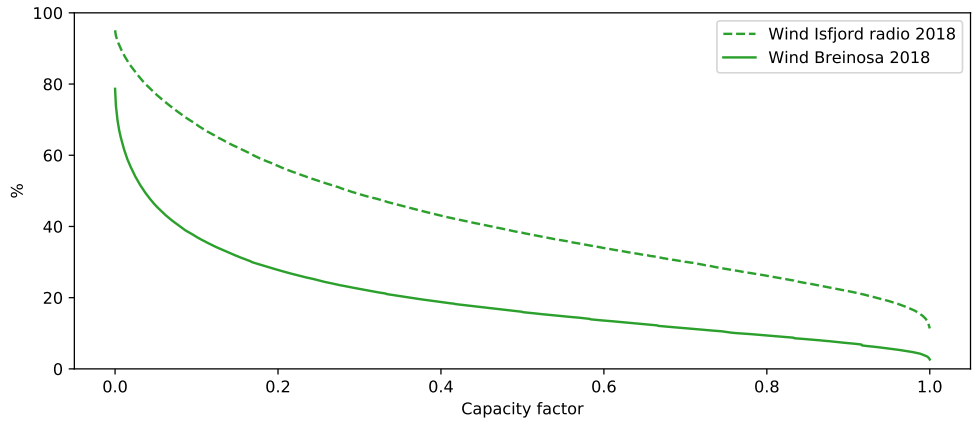

Figure 4.11: Duration curves for the capacity factors based on the measured wind speeds at both the Breinosa and Isfjord radio weather stations. The latter results in significantly higher possible power production per installed capacity than the former.

[17]The reason for the model underestimating the wind speeds to such an extent in this location, may be related to the region being in the vicinity of large mountains possibly disturbing wind flows, though actually being far enough away to experience wind conditions more like those further out at sea. More speculation around the MERRA-2 model will not be done here.

Table 4.8: Electric boiler data used in the optimization model.

Parameter	Value	Unit
Installed capacity per boiler	5	MW
Efficiency, η	99	%
Heat reserve factor, $c_{\text{r,heat}}$	50	%
Lifetime, c_{lifetime}	20	Years
Investment cost, $c_{\text{investment}}$	1578000	NOK/MW
Fixed O&M cost, $c_{\text{O\&M,fixed}}$	0.0003645	NOK/(MW · s)
Variable O&M cost, $c_{\text{O\&M}}$	0.001565	NOK/(MW · s)

4.5 Electric boiler

While the existing coal power plant produces more heat than electricity, potential wind and photovoltaic power sources replacing the electricity production give no heating. To partially replace the heat production in a less emissive future energy system, an electric boiler device is added to the model. Each boiler device is chosen to have a maximum heat output of 5 MW with no minimum output, and an efficiency of 99 %. This and cost data used in the Oogeso model is shown in Table 4.8.

4.6 Geothermal heat pump

Store Norske is doing studies on geothermal energy for Longyearbyen and the company is in the planning phase of a potential pilot drilling project to verify the studies [54]. The proposed full scale geothermal energy installation consists of 13 1600 meter deep wells and connected heat pumps with a thermal power output 4 times the electrical power input. The maximal heat output will be 5.2 MW in the winter half of the year and 2.6 MW in the summer[18] [55]. The resulting geothermal capacity factors for a year, used as the device profile are shown in Figure 4.12.

The proposed system has a lifetime of 40 years. The cost data for such a system is obtained from the DEA technology catalogue using the 2030 estimated geothermal data for wells that are 2000 meters deep[19]. The geothermal data used in the Oogeso model in addition to the capacity factor profile is given in Table 4.9.

[18] By halving the thermal energy extraction in the summer, the reservoir will recharge sufficiently before the next winter season.

[19] Due to remoteness and Arctic conditions often causing industrial projects to be more expensive than their mainland counterparts, the cost data for a deeper geothermal installation is taken to be a representative estimate for the cost of the proposed Svalbard system.

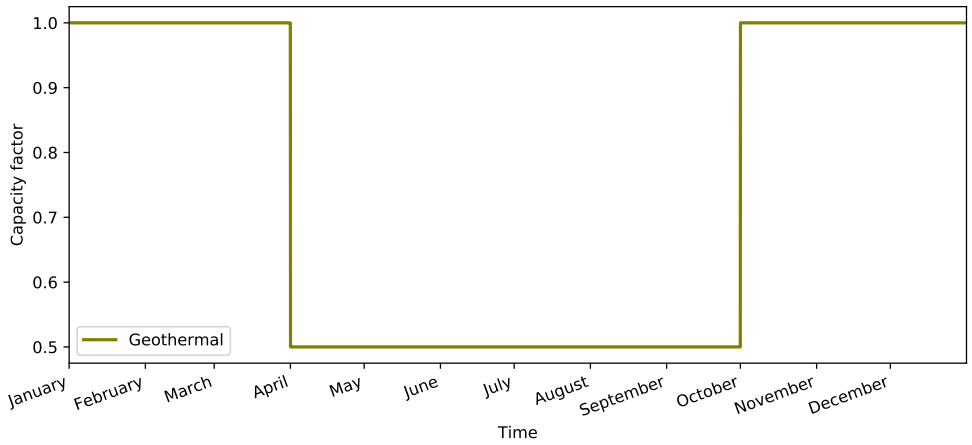

Figure 4.12: The capacity factors for the geothermal heat installation for a year.

Table 4.9: Geothermal heat pump data used in the optimization model.

Parameter	Value	Unit
Installed capacity, $f_{\max}$	5.2	MW
Efficiency, η	400	%
Heat reserve factor, $c_{\text{r,heat}}$	100	%
Lifetime, c_{lifetime}	40	Years
Investment cost, $c_{\text{investment}}$	30320000	NOK/MW
Fixed O&M cost, $c_{\text{O\&M,fixed}}$	0.008041	NOK/(MW · s)
Variable O&M cost, $c_{\text{O\&M}}$	0.01440	NOK/(MW · s)

4.7 Hydrogen system

At times when there is a greater renewable energy supply than demand, excess electricity production can be used to produce hydrogen and store the energy for later availability. Because of a much larger energy storage capacity for the same installation cost, a hydrogen system is more viable for long term energy storage than batteries, despite the lower electricity-to-electricity round-trip efficiency. Such a system can thus supplement an energy system based on intermittent sources like wind and photovoltaics.

Cost and lifetime data[20] for electrolyser and fuel cell devices is obtained from the U.S. Department of Energy [58]. For investment costs, the 2030 cost estimates were used, while for the other cost parameters only the 2018 cost data was provided and subsequently used in the model.

[20]This data is given in 2018$, which is translated to 2022$ using an inflation value of 13.4% [56], and converted into 2022 NOK using an exchange rate of 8.81 NOK/$ [57].

Table 4.10: Hydrogen data at a temperature of 273.15 K and a pressure of 1 atmosphere.

Parameter	Value	Unit
Density, ρ	0.0898	kg/Nm^3
Molar mass, M	2.016	g/mol
Ratio of heat capacities, γ	1.41	1
Energy content (HHV), c_{E}	12.7	MJ/Nm^3

4.7.1 Hydrogen as an energy carrier

Hydrogen gas (H_2) has a low volumetric density, while having a high gravimetric energy density, making storage at high pressures beneficial. The molar mass of the compound is 2.016 g/mol [59], while the ratio of heat capacities, the adiabatic index γ, is 1.41 [16]. Here the amount of hydrogen is, unless otherwise stated, measured in normal cubic meters (Nm^3). At these conditions the density of hydrogen gas is 0.0898 kg/Nm^3 [30]. The energy content is given as the higher heating value (HHV), which for hydrogen at normal conditions is 12.7 MJ/Nm^3 [30]. The information is summarized in Table 4.10.

4.7.2 Electrolyser

The electrolyser device uses electrical power to produce hydrogen gas and oxygen gas from water. A modern proton exchange membrane (PEM) electrolyser delivers hydrogen gas at a pressure of 3 MPa [60] and has an electrical efficiency of 73% [61], which is the proportion of the HHV of hydrogen produced to the amount of supplied electrical energy. In addition to this, 23 % of the HHV of hydrogen is produced as recoverable heat [61], which gives a waste heat recovery efficiency of 85%.

The hydrogen electrolyser data used in the Oogeso model is given in Table 4.11.

Table 4.11: Electrolyser data used in the optimization model.

Parameter	Value	Unit
Efficiency (HHV), η	73	%
Heat recovery efficiency, η_{heat}	85	%
Delivery pressure, $p_{\mathrm{in,\ compressor}}$	3	MPa
Lifetime, c_{lifetime}	30	Years
Investment cost, $c_{\mathrm{investment}}$	4366000	NOK/MW
Fixed O&M cost, $c_{\mathrm{O\&M,fixed}}$	0.004055	NOK/(MW $\cdot$ s)
Variable O&M cost, $c_{\mathrm{O\&M}}$	0.001388	NOK/(MW $\cdot$ s)

4.7.3 Compression and storage

The work required to compress hydrogen gas for long term storage will be between the isothermal and adiabatic cases, both of which are shown in Figure 2.7. Certain compressor technologies are nearly isothermal, like the ionic liquid piston compressor [62], while multi-stage[21] reciprocating compressors typically lie halfway between the isothermal and adiabatic regimes [63]. For the relevant cases simulated in this work, the compression of hydrogen is taken to require the average of the isothermal and adiabatic work, giving a compressor regime, $c_{\text{iso,ad, compressor}}$, of 50%. For the modeled compressor, the typical motor efficiency of 95% is used [64].

As heat recovery is part of the electrolyser device, the temperature of the hydrogen gas input to the compressor is taken to be already cooled down to 300 K[22]. The maximum pressure to which hydrogen gas is compressed and stored is chosen to be 70 MPa, which is the common limit of high pressure hydrogen storage tanks [65].

The energy difference between the hydrogen gas compression and the ideal isothermal compression is assumed recovered as heat for the district heating system with a recovery efficiency of 90%[23].

Predicted[24] 2030 storage costs[25], as well as the lifetime for compressed hydrogen storage tanks, is obtained from the *Technology Roadmap - Hydrogen and Fuel Cells* report by the International Energy Agency (IEA) [66]. The fixed O&M costs for such a storage solution is taken to be 1% of the investment cost per year [67], while the variable O&M costs are zero.

The hydrogen compressor and storage data used in the Oogeso model is given in Table 4.12.

[21] In multi-stage compressors the gas is cooled down in between each compression stage, with adiabatic compression during each stage. The process thus approaches being isothermal as the the number of compression stages increases.

[22] The electrolyser can thus be thought of as having an initial compression stage in a multi-stage compressor system, supplying cooled hydrogen gas at the delivery pressure to the next stage, which is the compressed storage device.

[23] This estimate is likely conservative, as heat removal throughout an isothermal process could also be partially recovered, in addition to the waste heat energy recovered here.

[24] It should be noted that the predicted investment cost of 1 2013$ per kWh of hydrogen storage is significantly lower, by a factor 6, than the investment cost given in various reports the past decade. Hence, it is possible that this prediction from 2013 may underestimate the actual cost of compressed hydrogen storage in 2030. As the investment cost has no impact on running the optimization model, it will not be further explored here.

[25] The storage costs are given in 2013$, which are translated to 2022$ using an inflation value of 22.1% [56].

Table 4.12: Hydrogen compressor and storage data used in the optimization model.

Parameter	Value	Unit
Compressor regime, $c_{\text{iso,ad, compressor}}$	50	%
Compressor efficiency, $\eta_{\text{compressor}}$	95	%
Heat recovery efficiency, $c_{\text{r,heat}}$	85	%
Input hydrogen pressure[26], $p_{\text{in, compressor}}$	3	MPa
Input hydrogen temperature, $T_{\text{compressor}}$	300	K
Maximum storage pressure, $p_{\text{max, compressor}}$	70	MPa
Storage system lifetime, c_{lifetime}	20	Years
Investment cost, $c_{\text{investment}}$	37.95	NOK/Nm^3
Fixed O&M cost, $c_{\text{O\&M,fixed}}$	0.00000001203	NOK/(Nm^3 · s)
Variable O&M cost, $c_{\text{O\&M}}$	0.0	NOK/(Nm^3 · s)

For long term energy storage in the form of hydrogen, the seasonal variations of factors like energy demand and production capacities are of interest to plan storage levels, though typically outside the optimization horizon of the model. To take into account the trend of wanting to increase the hydrogen storage level during the summer in order to have sufficient energy for the winter, a target profile is created and given in Figure 4.13. The target level oscillates sinusoidally between 40% and 80%, and is offset by two months from the assumed minimum and maximum production time periods. This is to account for the time delay in attaining and using the stored energy.

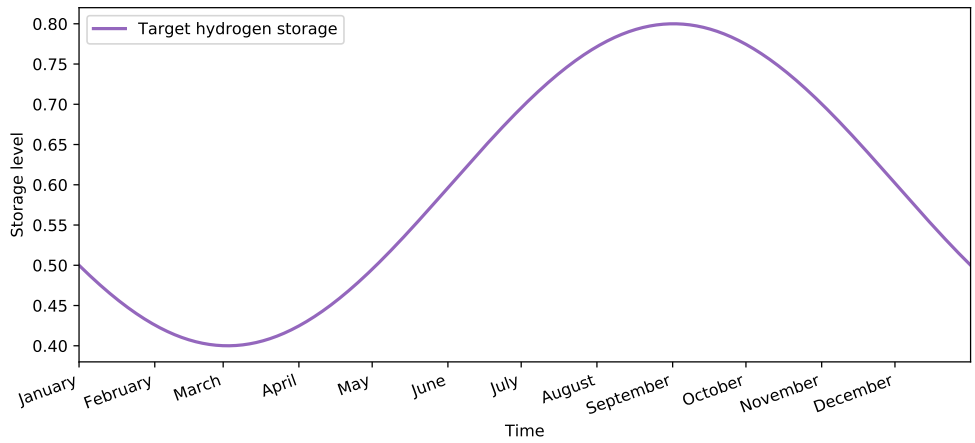

Figure 4.13: The target hydrogen storage profile. The profile varies sinusoidally, with the minimum at 40% set for March 1st, and the maximum at 80% set for September 1st.

[26]The input hydrogen pressure is the delivery pressure from the electrolyser device.

Table 4.13: Fuel cell data used in the optimization model.

Parameter	Value	Unit
Efficiency (HHV), η	50	%
Heat recovery efficiency, η_{heat}	80	%
Electric reserve factor, c_{r}	100	%
Heat reserve factor, $c_{\text{r,heat}}$	100	%
Lifetime, c_{lifetime}	30	Years
Investment cost, $c_{\text{investment}}$	9481000	NOK/MW
Fixed O&M cost, $c_{\text{O\&M,fixed}}$	0.004055	NOK/(MW · s)
Variable O&M cost, $c_{\text{O\&M}}$	0.001388	NOK/(MW · s)

4.7.4 Fuel cells

A proton exchange membrane (PEM) fuel cell is here considered for converting the chemical energy stored in hydrogen gas to electrical power. Such a fuel cell typically has an (HHV) efficiency of about 50% [68], meaning that half of the HHV energy of hydrogen is turned into electrical energy. In addition, as for the electrolyser, a lot of heat is emitted in the process, and 40% of the HHV of hydrogen is produced as recoverable heat in the fuel cell [68], giving a waste heat recovery efficiency of 80%.

The fuel cell data used in the Oogeso model is given in Table 4.13.

4.8 Load

The historical electricity and heat load for Longyearbyen have been obtained for the years 2017 and 2018 [69]. This data is the output power from the coal power plant, which is equivalent to the load covered by the energy system of the town as long as the diesel system is not used. This is most frequently the case, though the diesel system has sporadically provided between 1 and 2 MW of thermal power at peak load times during the winter [7]. In this work, it is presumed that the coal power plant production gives a sufficiently accurate representation of the time-dependent electricity and heat load[27], and the timeseries for 2018 used in the model are shown in Figure 4.14.

It is worth noting the 9-day period in July with significantly reduced load. At this time the coal mine ceases production, reducing the needed electricity load enough for part of the power plant to also shut down. The result is a much lower electricity and heat production, and the diesel boiler systems, for which data is not obtained, cover the remaining heat demand of the settlement.

[27]The current energy transition plan has the aim of reducing heating demands for the existing network by 30% towards 2030, through increasing the energy efficiency [6]. The future energy system would thus require less heat energy, justifying using the heat load profile from the coal power plant without including the peak load covered by the diesel system.

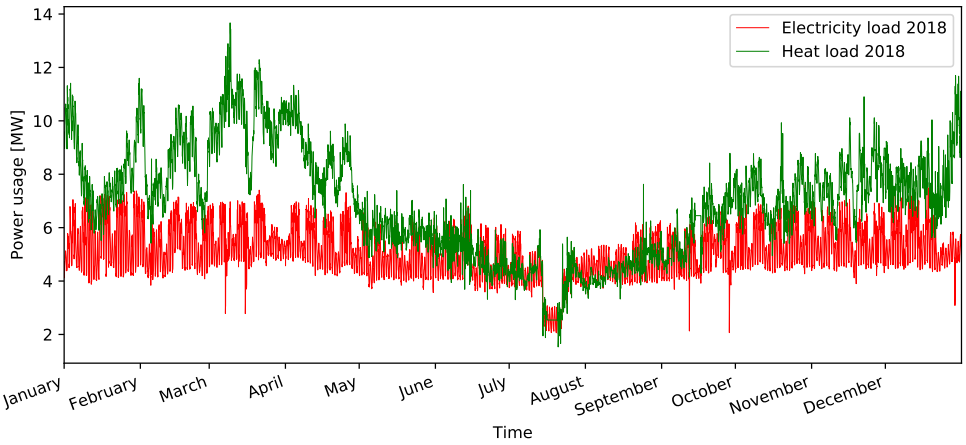

Figure 4.14: The electricity and heat load of the Longyearbyen energy system in 2018. In July there were 9 days where the coal mine had a production break, and consequently one of the coal power plant generators was switched off. These two effects reduce the needed production of electricity substantially, causing the heat load to be covered by the external diesel system for which data is not obtained.

This reduced load period illustrates the relatively large electricity demands for the coal-related parts of the energy system. The coal power plant uses 17% of the produced electrical power, while the coal mine uses 13% [7]. The former will be decommissioned in the autumn of 2023 [5], while the latter will be decommissioned in September of the same year [70]. Although this will reduce the electricity demand by 30%, the load data used in the Oogeso model includes the usage by these two electricity users to account for future growth and possible energy-intensive industry establishments.

Chapter 5

Different modeling cases

The Oogeso program, explained in Chapter 3, is supplemented with the data given in Chapter 4 to simulate different potential renewable energy systems for Longyearbyen. As actual wind and load data, in addition to sun data from a weather model, is available for the year 2018, all simulated cases use data for that year.

Six different year-long simulations will be analyzed here[1], with an overview of the devices used in each case given in Table 5.1. All of the cases include the battery pack under construction, while all cases except the final, fully renewable alternative include the existing diesel system.

In all cases an additional electricity sink and heat sink device are included as "dump" devices. This is the curtailed power[2], and the purpose of these devices is for the flow of heat and electricity to have an outlet in the case where more power is produced than can be used. A small variable O&M cost to discourage usage unless necessary is added to the curtailment devices[3].

Table 5.1: The installed capacities of different energy systems for the six cases studied.

Device	Case 1	Case 2	Case 3	Case 4	Case 5	Case 6
Diesel system	Current	Current	Current	Current	Current	-
Battery	7 MWh	7 MWh	7 MWh	7 MWh	7 MWh	7 MWh
PV	-	25 MWp	25 MWp	25 MWp	25 MWp	25 MWp
Wind	-	-	17.25 MW	31.05 MW	17.25 MW	44.85 MW
Electric boiler	-	-	5 MW	5 MW	5 MW	10 MW
Geothermal	-	-	5.2 MW	5.2 MW	5.2 MW	5.2 MW
Electrolyser	-	-	-	35 MW	25 MW	50 MW
Fuel cell	-	-	-	10 MW	10 MW	15 MW
H_2 storage	-	-	-	1.2 MNm^3	1.2 MNm^3	4 MNm^3

[1] Results from additional cases are given in Appendix A.

[2] It can be noted that this is curtailed power that is already produced, as opposed to curtailed power from intermittent energy sources, like wind power, that is never produced.

[3] The O&M cost for the dump devices are excluded from the post-simulation cost analyses.

5.1 Case 1: base case

The first simulated case utilizes the existing diesel generator and boiler system as well as the battery system currently being installed. This is the planned transitional energy system that will be used after the coal power plant is shut down, until a more renewable energy system is in place. A diagram showing the flow of energy carriers at a certain timestep of the simulation of this base case is given in Figure 5.1. Some key results from the simulation are given in Table 5.2.

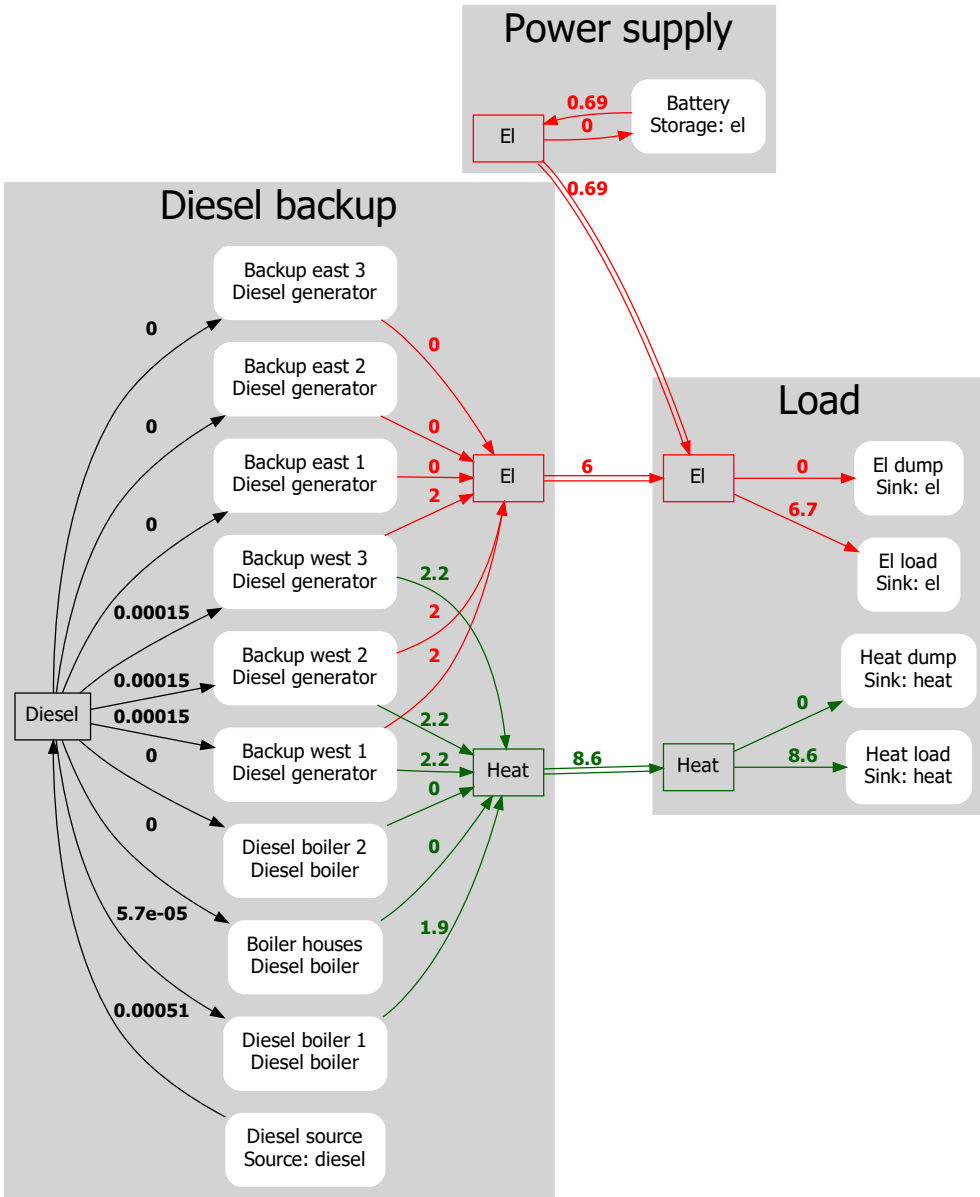

Figure 5.1: Case 1: The base case of the diesel and battery system. The energy carrier flows at a specific timestep are shown.

5.2 Case 2: PV installation

In the second case, the base case is supplemented by a 25 MWp photovoltaic installation. Though this will only aid electricity production during the summer, the installation can be done on the ceilings and walls of existing buildings. This case thus requires no major alterations to the landscape near Longyearbyen, while still reducing emissions. A diagram showing the flow of energy carriers at a certain timestep of the simulation of this case is given in Figure 5.2. Some key results from the simulation are given in Table 5.3.

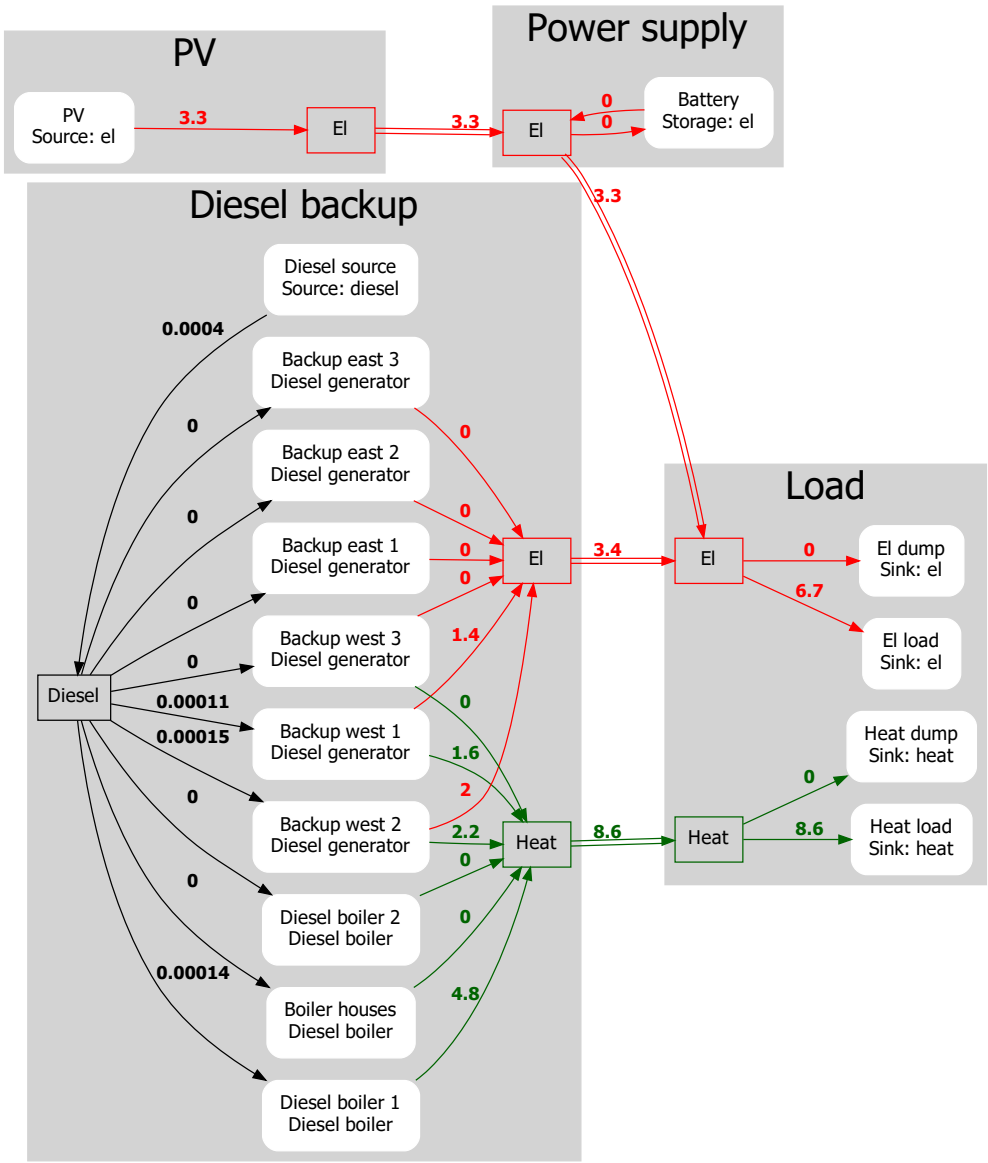

Figure 5.2: Case 2: The base case supplemented by a 25 MWp PV installation. The energy carrier flows at a specific timestep are shown.

Table 5.2: Key results after simulating the base case for one year.

Parameter	Value
CO_2 emissions per year	$35.49 \cdot 10^6$ kg
Diesel consumption per year	$12.31 \cdot 10^3$ Nm^3
Electricity consumption per year	$45.98 \cdot 10^3$ MWh
Average electricity consumption	5.25 MW
Curtailed electric energy per year	0.17 MWh
Heat consumption per year	$60.06 \cdot 10^3$ MWh
Average heat consumption	6.86 MW
Curtailed heat energy per year	$1.26 \cdot 10^3$ MWh
Diesel generator starts per year	1103
Diesel generator running hours per year	24990
Diesel boiler starts per year	1348
Diesel boiler running hours per year	5571

Table 5.3: Key results after simulating case 2 for one year.

Parameter	Value
CO_2 emissions per year	$30.16 \cdot 10^6$ kg
Diesel consumption per year	$8.99 \cdot 10^3$ Nm^3
Electricity consumption per year	$46.42 \cdot 10^3$ MWh
Average electricity consumption	5.30 MW
Curtailed electric energy per year	0.00 MWh
Heat consumption per year	$60.06 \cdot 10^3$ MWh
Average heat consumption	6.86 MW
Curtailed heat energy per year	74.28 MWh
Diesel generator starts per year	1453
Diesel generator running hours per year	18352
Diesel boiler starts per year	1633
Diesel boiler running hours per year	8266
PV production per year	$12.25 \cdot 10^3$ MWh
Curtailed PV energy	$3.88 \cdot 10^3$ MWh

5.3 Case 3: PV, geothermal, and small onshore wind installations

Building on the previous case, case 3 is additionally supplemented by 5 onshore wind turbines yielding an installed wind capacity of 17.25 MW. Additional electric energy not covering the electric load can be used to supply part of the heating demand using a geothermal heat pump with a winter capacity of 5.2 MW and a summer capacity of 2.6 MW. Additionally an electric boiler that can supply up to 5 MW of heat is included. The energy system then has an intermittent supply of renewable electricity, and by extension renewable heating, year round, while relying on the diesel backup system to fill the gaps in electricity and heat production. As there is no long term energy storage, significant wind production will be curtailed in times with high wind capacity factors. A diagram showing the flow of energy carriers in the system is given in Figure 5.3.

Some key results from the simulation are given in Table 5.4.

Table 5.4: Key results after simulating case 3 for one year.

Parameter	Value
CO_2 emissions per year	$16.06 \cdot 10^6$ kg
Diesel consumption per year	$5.64 \cdot 10^3$ Nm^3
Electricity consumption per year	$61.66 \cdot 10^3$ MWh
Average electricity consumption	7.04 MW
Curtailed electric energy per year	0.00 MWh
Heat consumption per year	$60.06 \cdot 10^3$ MWh
Average heat consumption	6.86 MW
Curtailed heat energy per year	8.37 MWh
Diesel generator starts per year	1651
Diesel generator running hours per year	11568
Diesel boiler starts per year	1060
Diesel boiler running hours per year	2136
PV production per year	$15.16 \cdot 10^3$ MWh
Curtailed PV energy	$0.97 \cdot 10^3$ MWh
Wind production per year	$23.65 \cdot 10^3$ MWh
Curtailed wind energy	$10.11 \cdot 10^3$ MWh

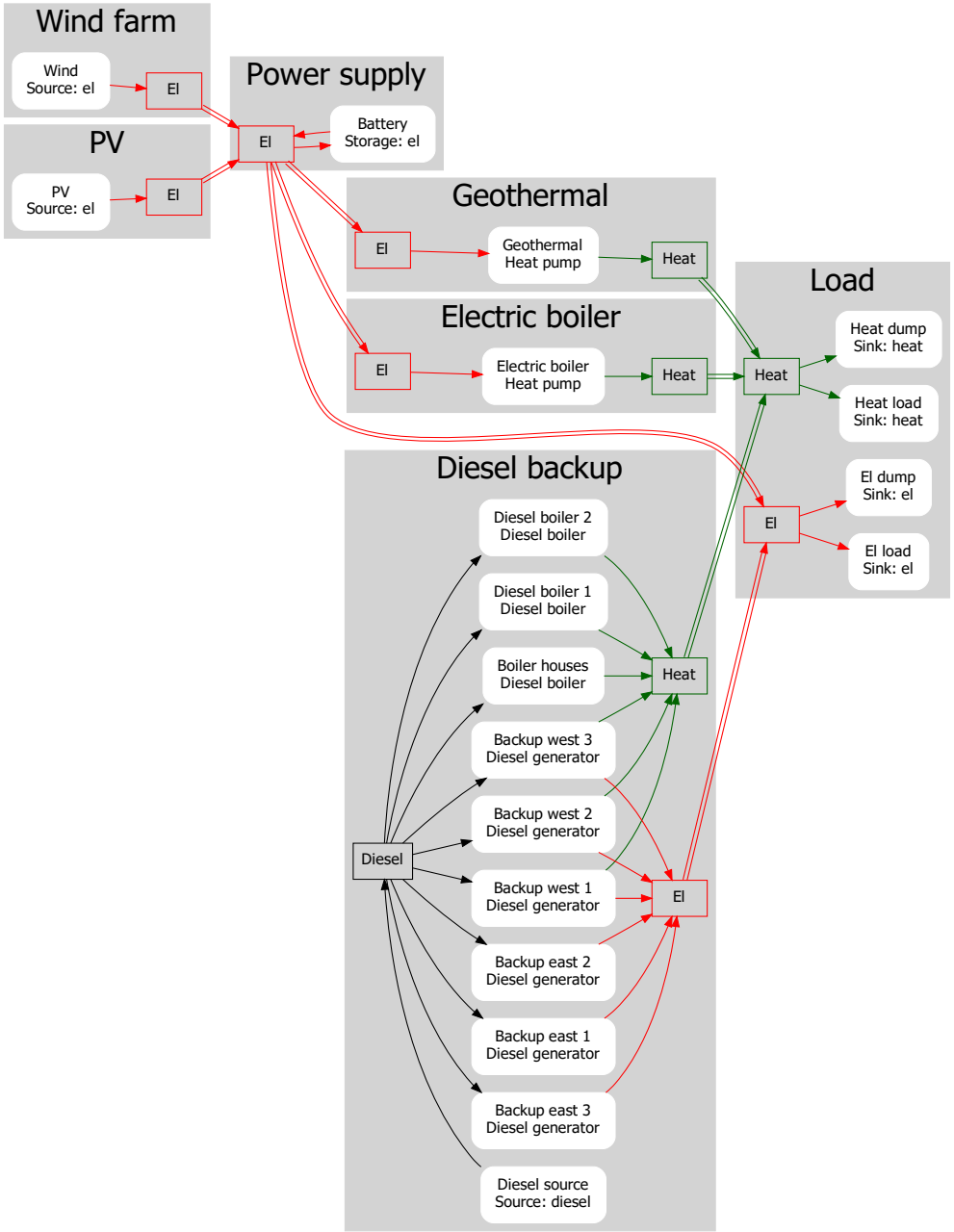

Figure 5.3: Case 3: The base case supplemented by a 25 MWp PV installation, a 17.25 MW wind power installation, a 5.2 MW geothermal installation, and a 5 MW electric boiler. Only the flow edges, without flow values, of the different energy carriers are shown.

5.4 Case 4: all devices - onshore

For the fourth case, the previous case is further supplemented by nearly doubling the wind power installation to 9 turbines and an installed capacity of 31.05 MW. A full hydrogen production, storage, and usage facility is included to store renewable energy produced during high wind periods for usage in low wind periods. An electrolysis capacity of 35 MW is thus installed in addition to a storage capacity of 1 200 000 Nm^3 (≈107 900 kg) and a fuel cell production capacity of 10 MW. A diagram showing the flow of energy carriers in the system is given in Figure 5.4.

The hydrogen storage level at every timestep is shown in Figure 5.5. The storage level at the beginning[4] and end of the simulated year is at 450 000 Nm^3 (≈40 400 kg).

Some key results from the simulation are given in Table 5.5.

Table 5.5: Key results after simulating case 4 for one year.

Parameter	**Value**
CO_2 emissions per year	$4.75 \cdot 10^6$ kg
Diesel consumption per year	$1.42 \cdot 10^3$ Nm^3
Electricity consumption per year	$98.57 \cdot 10^3$ MWh
Average electricity consumption	11.25 MW
Curtailed electric energy per year	0.00 MWh
Heat consumption per year	$60.06 \cdot 10^3$ MWh
Average heat consumption	6.86 MW
Curtailed heat energy per year	226.83 MWh
Diesel generator starts per year	918
Diesel generator running hours per year	2681
Diesel boiler starts per year	552
Diesel boiler running hours per year	1228
PV production per year	$16.13 \cdot 10^3$ MWh
Curtailed PV energy	$0.00 \cdot 10^3$ MWh
Wind production per year	$60.76 \cdot 10^3$ MWh
Curtailed wind energy	$0.00 \cdot 10^3$ MWh
Hydrogen production per year	$8.40 \cdot 10^6$ Nm^3
Average hydrogen storage level	$0.34 \cdot 10^6$ Nm^3

[4]For all cases with hydrogen storage, the initial storage level value is chosen such that it is approximately the same as the storage level at the end of the simulation.

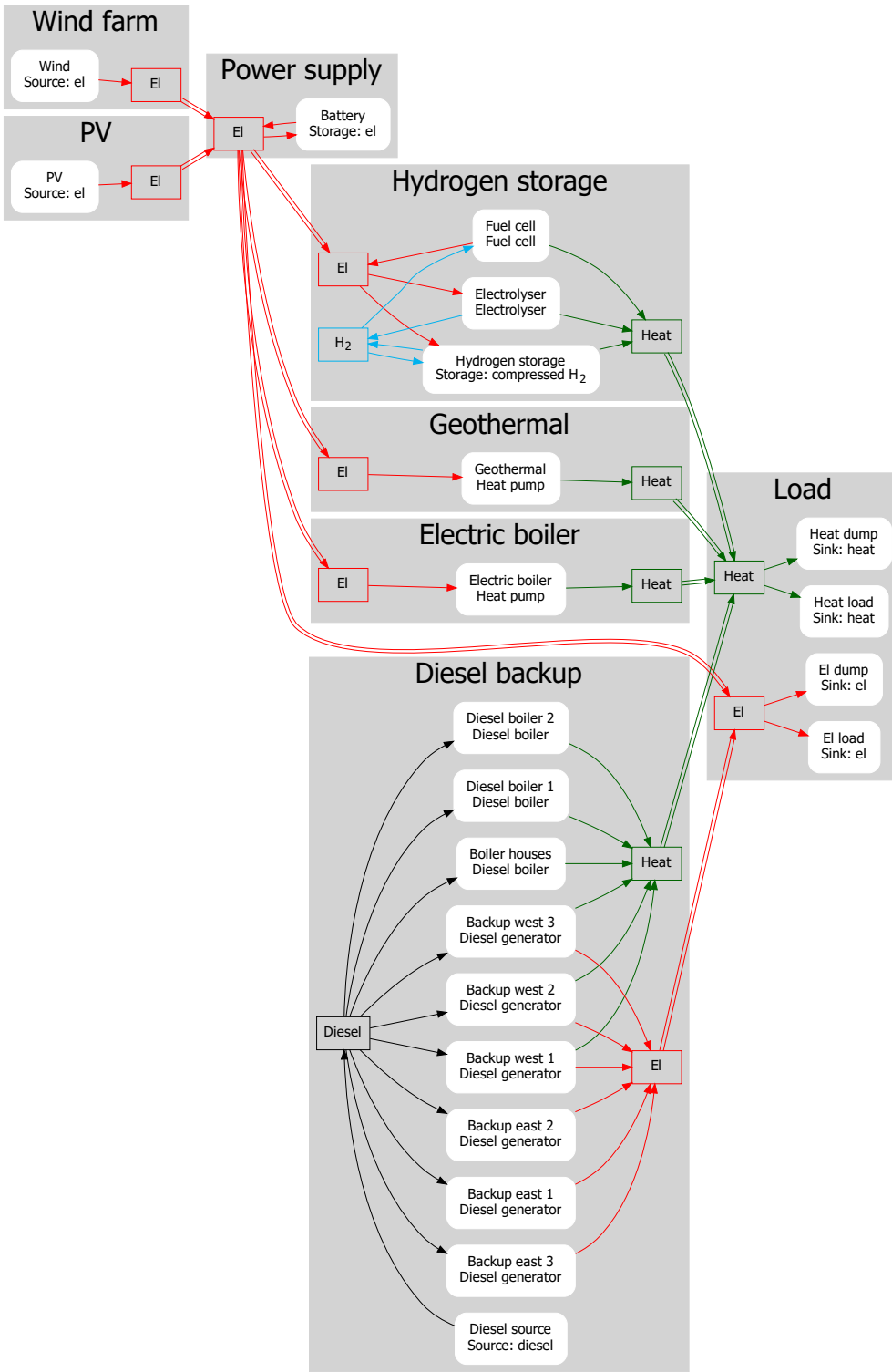

Figure 5.4: Case 4 and 5: A case utilizing all discussed energy devices, including a hydrogen system for long term energy storage.

5.5 Case 5: all devices - offshore

The fifth case utilizes the same devices as the fourth case, but the offshore wind capacity factors are used instead of the onshore ones. As the average offshore capacity factor of 0.40 is almost twice the corresponding onshore value of 0.22, only 5 offshore wind turbines, yielding a maximum capacity of 17.25 MW, are installed in this case. A lower maximum electricity production necessitates a smaller hydrogen production system, and a 25 MW electrolyser is installed. The higher capacity factors, however, still necessitate large storage capacities, and hydrogen tanks for storing at maximum 1 200 000 Nm^3 (≈107 900 kg) are installed, in addition to a fuel cell production capacity of 10 MW. The energy system diagram is identical to that of case 4, shown in Figure 5.4.

The hydrogen storage level at every timestep is shown in Figure 5.6. The storage level at the beginning and end of the simulated year is at 60 000 Nm^3 (≈5 400 kg).

Some key results from the simulation are given in Table 5.6.

Table 5.6: Key results after simulating case 5 for one year.

Parameter	**Value**
CO_2 emissions per year	$3.18 \cdot 10^6$ kg
Diesel consumption per year	$0.66 \cdot 10^3$ Nm^3
Electricity consumption per year	$91.55 \cdot 10^3$ MWh
Average electricity consumption	10.45 MW
Curtailed electric energy per year	0.00 MWh
Heat consumption per year	$60.06 \cdot 10^3$ MWh
Average heat consumption	6.86 MW
Curtailed heat energy per year	39.98 MWh
Diesel generator starts per year	545
Diesel generator running hours per year	1277
Diesel boiler starts per year	861
Diesel boiler running hours per year	1962
PV production per year	$16.13 \cdot 10^3$ MWh
Curtailed PV energy	$0.00 \cdot 10^3$ MWh
Wind production per year	$60.56 \cdot 10^3$ MWh
Curtailed wind energy	$0.00 \cdot 10^3$ MWh
Hydrogen production per year	$6.25 \cdot 10^6$ Nm^3
Average hydrogen storage level	$0.29 \cdot 10^6$ Nm^3

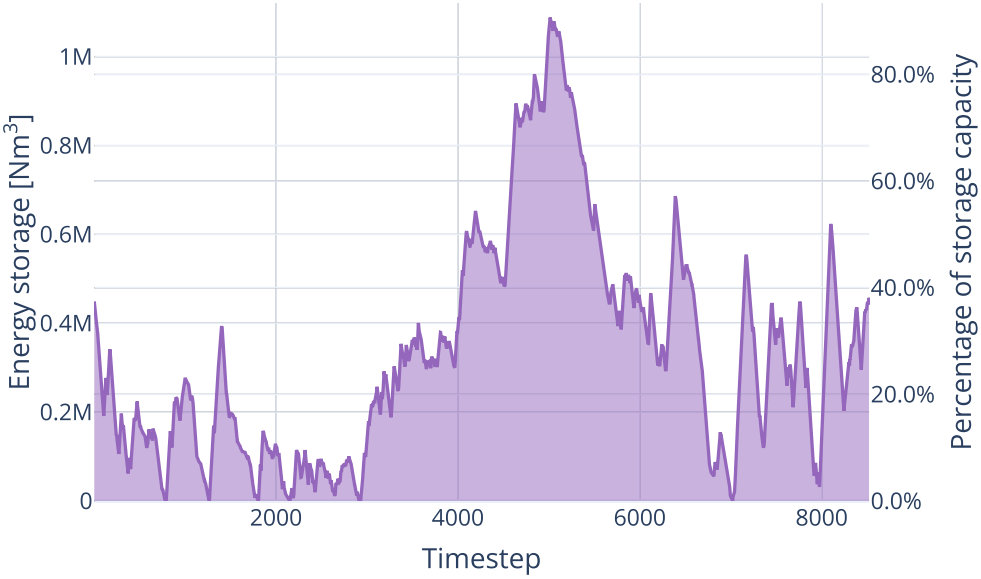

Figure 5.5: The hydrogen storage level evolution over each hour of the year simulated in case 4.

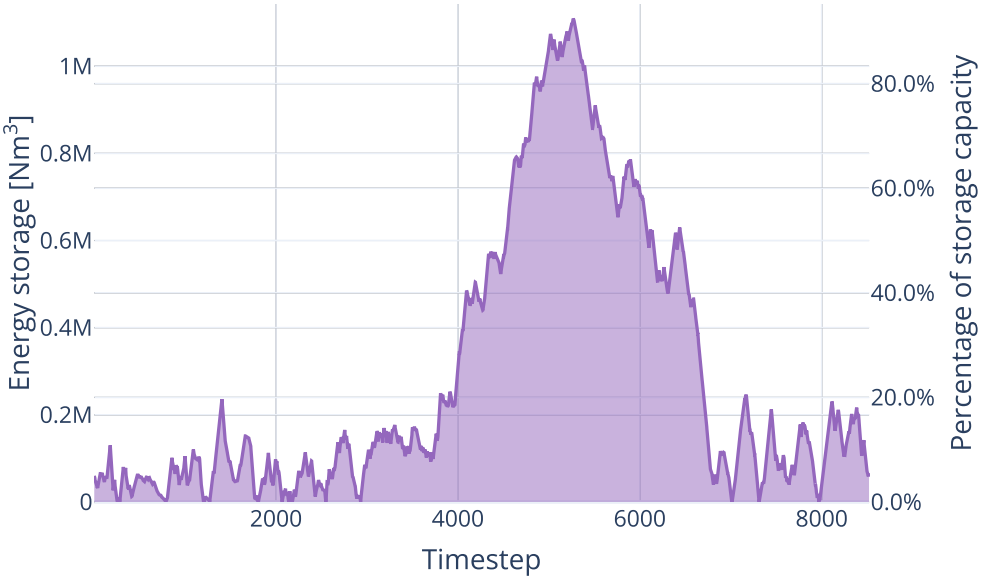

Figure 5.6: The hydrogen storage level evolution over each hour of the year simulated in case 5.

5.6 Case 6: fully renewable - onshore

Case 6 is a modification of case 4 where all the diesel devices are removed from the simulation. To compensate for the diesel system, a total of 13 wind turbines with a total capacity of 44.85 MW are installed onshore. Such a high maximum electricity production necessitates a large hydrogen system, and a 50 MW electrolyser is installed in addition to a storage capacity of 4 000 000 Nm^3 (≈360 000 kg) and a fuel cell production capacity of 15 MW. Finally, to ensure being able to cover the heating demands in addition to having reserve heating capacity, the electric heating system is expanded to having two electric boilers, giving a maximum output of 10 MW. The corresponding energy system diagram is given in Figure 5.7.

The hydrogen storage level at every timestep is shown in Figure 5.8. The storage level at the beginning and end of the simulated year is at 3 500 000 Nm^3 (≈315 000 kg).

Some key results from the simulation are given in Table 5.5.

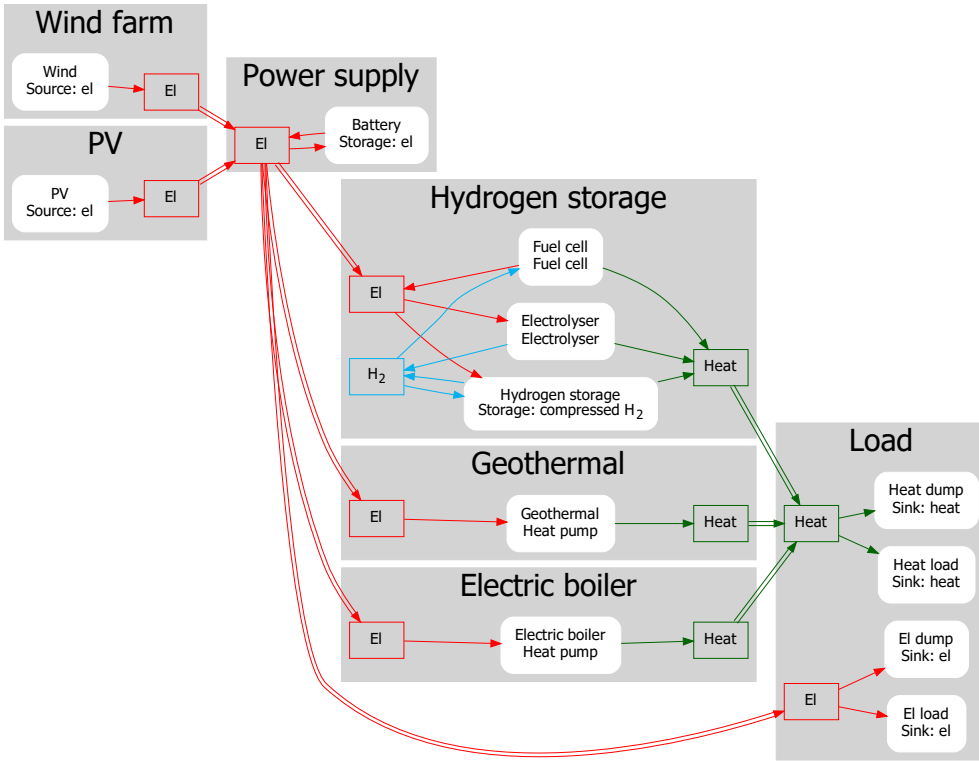

Figure 5.7: Case 6: A case utilizing all renewable energy devices, yielding no CO_2 emissions.

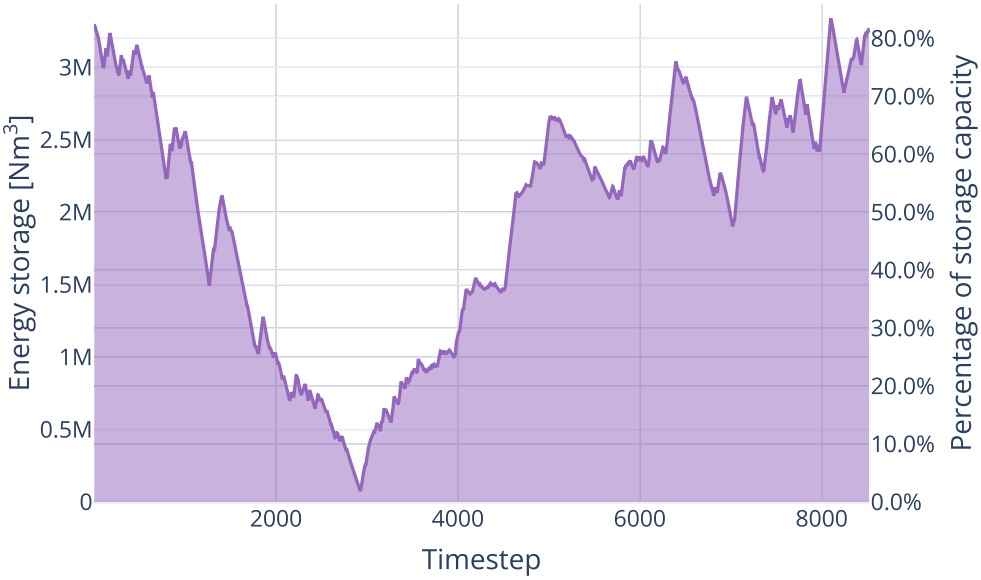

Figure 5.8: The hydrogen storage level evolution over each hour of the year simulated in case 6.

Table 5.7: Key results after simulating case 6 for one year.

Parameter	Value
CO_2 emissions per year	0.00 kg
Electricity consumption per year	$128.02 \cdot 10^3$ MWh
Average electricity consumption	14.61 MW
Curtailed electric energy per year	0.00 MWh
Heat consumption per year	$60.06 \cdot 10^3$ MWh
Average heat consumption	6.86 MW
Curtailed heat energy per year	2037 MWh
PV production per year	$16.13 \cdot 10^3$ MWh
Curtailed PV energy	$0.00 \cdot 10^3$ MWh
Wind production per year	$87.77 \cdot 10^3$ MWh
Curtailed wind energy	$0.00 \cdot 10^3$ MWh
Hydrogen production per year	$13.07 \cdot 10^6$ Nm^3
Average hydrogen storage level	$1.96 \cdot 10^6$ Nm^3

Chapter 6

Discussion of the simulated cases

The different cases simulated all have significantly lower emissions than the current coal power plant. Another factor to consider is how much different parts of the diesel system are utilized for the varying amounts of installed renewable energy devices. It is also of interest to see how the different alternatives affect the overall energy usage of the system, and how much renewable energy is curtailed for the cases with no long term storage. Correspondingly, for the cases with long term storage the amount of hydrogen production is of interest. Finally, an estimation of the costs of the different cases will be looked into. Some of the plots given in this chapter are also constructed for additional cases and shown in Appendix A.

6.1 CO_2 emissions

Since one of the main motivations for closing the coal power plant in Longyearbyen is to reduce the carbon emissions of the energy system, it is of key importance how the emissions of the simulated energy system cases here compare with the current emissions. The yearly CO_2 emissions from the coal power plant are 78 million kg [6], and the emissions from the six simulation cases are given in Figure 6.1.

In these simulations, only the diesel devices give CO_2 emissions, arising from the carbon content of the diesel fuel being burned. The emissions from these devices, split into the diesel generator and diesel boiler device groups are shown explicitly in Figure 6.2. It is evident that the majority of the emissions stem from the diesel generators. This can be attributed to the waste heat recovery installation on the generators being able to supply about 6.6 MW of heat energy as in Figure 5.1, which covers the majority of the heating demand most of the year as seen from Figure 4.14.

The base case utilizing the current diesel system, with waste heat recovery on three generators, and a 7 MWh battery, gives yearly CO_2 emissions of 35.5 million kilograms. This is 45.5% of the current coal power plant emissions and a reduction of 42.5 million kg CO_2. These values correlate very well with the estimates that closing down the coal power plant and using the diesel system will reduce emissions with 43 million kilograms [5]. The model thus yields reasonable values

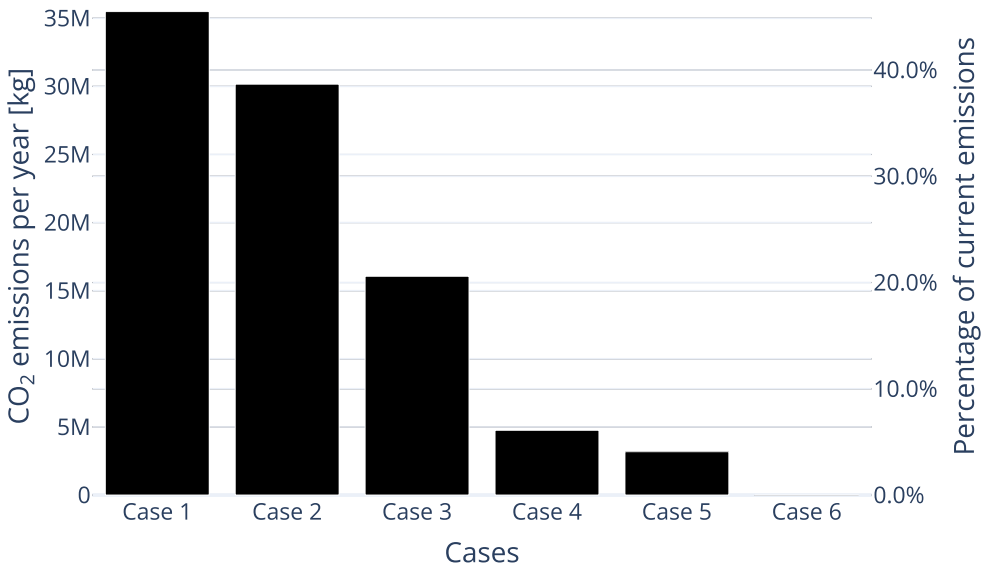

Figure 6.1: The carbon dioxide emissions per year for the simulated energy system cases. The right axis shows the emissions as a percentage of the current coal power plant yearly emissions.

for base case emissions. Of the base case emissions, only 3.1 million kilograms, or 8.8%, arise from the diesel boilers, showing that the combined power and heating diesel generators account for the vast majority of the emissions.

The second case, implementing 25 MWp of photovoltaic (PV) cells to supplement the diesel system during the summer season further reduces the emissions to 30.2 million kilograms, which is 38.7% of the current emissions. Due to a lot of diesel generator power production being replaced by PV power production, less waste heat is supplied to the district heating system. More of the heating energy is then supplied by the diesel boilers instead, increasing the diesel boiler CO_2 emissions to 6.5 million kilograms, or 21.7%, of the total emissions in this case. As the majority of emissions stem from the winter season with increased electricity and especially heat demands, as seen in Figure 4.14, it is expected that the emission reduction from a PV installation will only constitute a minor part of the total emissions. Further reductions require the installation of less emissive energy sources that also operate in the winter season.

The third case implements such a source with a 17.5 MW onshore wind farm in the already industrialized Breinosa area. As the maximum renewable electricity production far exceeds the highest electricity demands, especially during the summer season, both the 5.2 MW geothermal heat pump and a 5 MW electric boiler is included to convert excess electric energy to heat energy. This case thus not only reduces emissions from electricity production, but also from the heat production for the district heating system, which solely relied on diesel devices in the first two cases. The total CO_2 emissions from this case is 16.1 million kilograms, which is

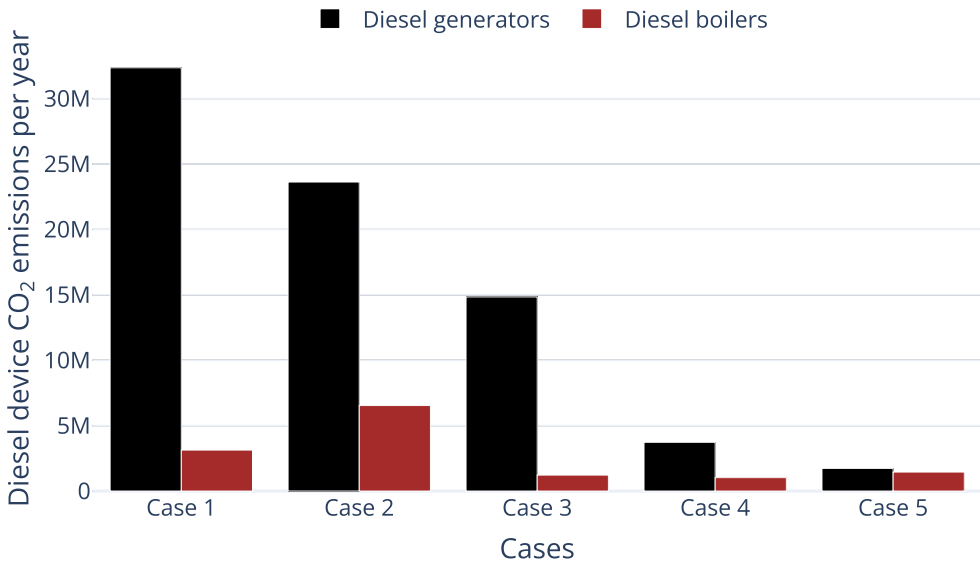

Figure 6.2: The carbon dioxide emissions per year for the simulated energy system cases split into the diesel generator and diesel boiler devices.

20.6% of the current emissions. Of this, 1.2 million kilograms, or 7.6%, arise from the diesel boilers, giving a similar emission split as the base case.

Introducing the hydrogen production and storage system in case 4, along with an expanded onshore wind installation of 30.05 MW, drastically reduces the remaining emissions. In this case there are 4.8 million kilograms of CO_2 emissions, which is only 6.1% of the current energy production emissions in the town. Figure 6.2 show that nearly the entirety of this emission reduction, compared to case 3, comes from reduced diesel generator emissions. The diesel boilers give emissions of 1.0 million kilograms, which is now 21.6% of all emissions. The heat energy no longer supplied by the diesel generator waste heat is instead covered by a combination of the geothermal heat pump and electric boiler, and the waste heat recovery from the electrolyser, hydrogen compressor, and the fuel cells.

As a variation of case 4, case 5 uses a 17.25 MW offshore wind installation with the Isfjord radio weather data instead of an onshore wind farm. Even though the installed wind capacity is only a bit over half of the previous case, the CO_2 emissions after simulating the energy system for one year are markedly lower at 3.2 million kilograms, or 4.1% of the current emissions. The more stable wind conditions lead to the diesel generators emitting less than the previous case, but the lower production capacity also limits the excess electricity available to produce renewable heat energy using the geothermal heat pump and the electric boiler at times when the hydrogen storage is low. The diesel boilers account for 1.5 million kilograms, or 45.6% of all emissions in this case.

The sixth case is a fully renewable case in which no diesel devices are included. Consequently, there are no CO_2 emissions resulting from the system simulation.

6.2 Diesel system usage

Another metric for comparing the different energy system cases is how frequently the diesel generators and boilers need to be turned on, and how many running hours these devices have per year. The device starts are given in Figure 6.3, while the device running hours are given in Figure 6.4.

It can here be noted that all boiler houses are modeled as one device. However, since the boiler house heat output is always below 2.5 MW for all timesteps for all cases modeled here, only up to one of the seven houses needs to be turned on and run at any one timestep. The total actual required device starting times and running hours are then still represented by their respective values summed over all modeled devices over all simulated timesteps.

Even though case 2 and case 3 have much lower emissions, and thus lower fuel consumption, than case 1, the diesel devices for these two cases are started up significantly more often. The intermittent renewable energy sources require the diesel generators to more frequently turn on and off to supplement the renewable electricity generation, which again reduces the availability of heat energy sources in case 2, requiring the diesel boilers to also frequently turn on to cover the heating demand. With long term hydrogen storage supplementing the electricity generation in case 4 and 5, however, there are fewer timesteps requiring diesel generators running. It is notable that the offshore case (5) requires the boilers to turn on almost twice as often as the onshore case (4), attributed to less excess wind energy being available for the electric heating devices.

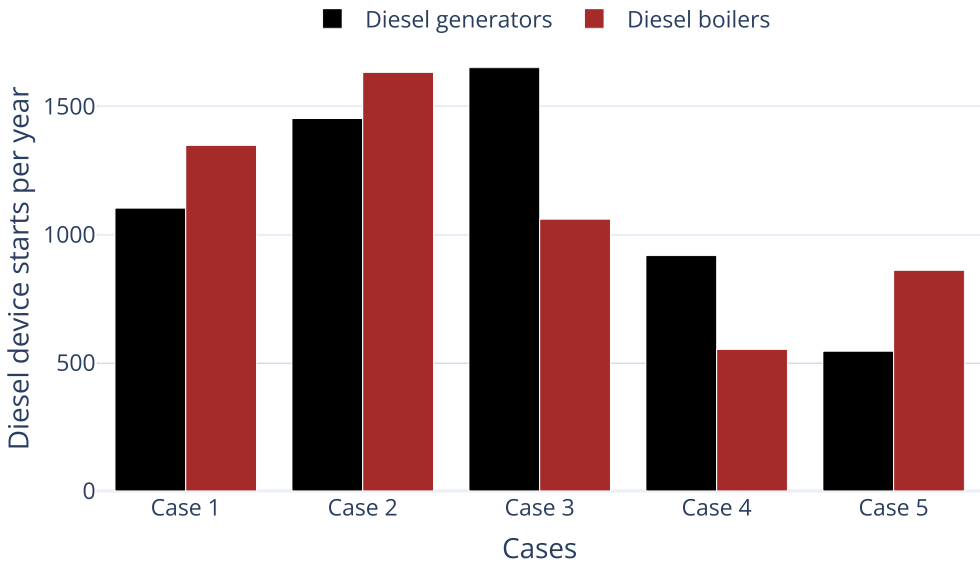

Figure 6.3: The number of times the diesel generator and diesel boiler devices are started up per year for the six simulated cases.

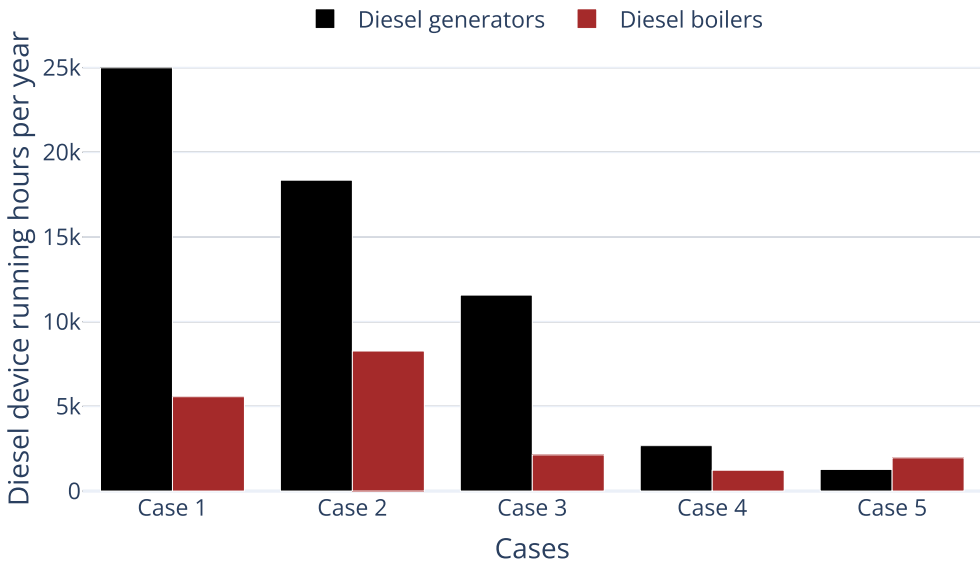

Figure 6.4: The number of hours the diesel generator and diesel boiler devices are running per year for the six simulated cases.

The operational hours per year for the cases follow the same trend as the emissions per device. As the generators are more efficient the higher their power output, it is reasonable that the optimization model chooses to run them at full capacity during the timesteps they are on, giving a very close correlation between the running hours and emissions from these devices. For the diesel boilers, the power output is proportional to the fuel input, giving an exact correlation between operational hours and emissions for each boiler device. The sum over boiler devices with similar efficiencies thus retains much of this correlation.

It is also clear that the emissions per operational hour are significantly lower for the diesel boiler devices than they are for the diesel generator devices, visualized in Figure 6.5. As stated above, the simulation tries to let the generators run at maximum capacity, giving very similar average emissions per hour for the different scenarios. For the diesel boilers, the boiler houses have a lower efficiency than the other boiler devices, but a lower minimum production. As there is no short term heat storage device, like the battery for electricity, the less efficient boiler houses are thus operated more in the cases with intermittent sources to cover small demands not met by the excess electric energy converted to heat. The resulting emissions per running hour is thus higher and more variable for cases 2 through 5, while still being about half of the generator emissions per hour due to the higher energy efficiency of burning diesel for heat than burning it for electricity.

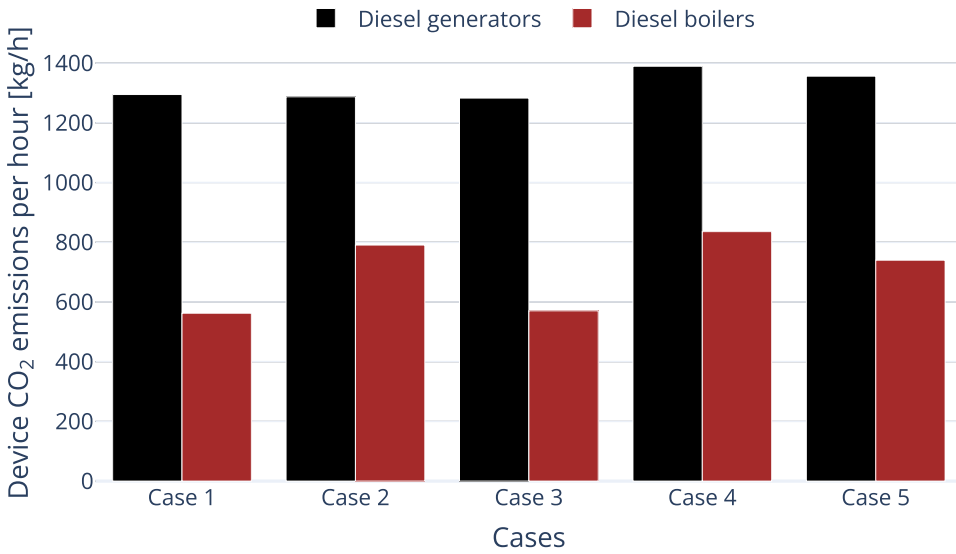

Figure 6.5: The average CO_2 emissions per operational hour of the diesel generator and diesel boiler devices for the six simulated cases.

Another value to inspect is the average device running hours per start up, which is displayed in Figure 6.6. The average diesel boiler running hours per device start is seen to be relatively stable between 2 and 5 hours for all the cases, while the diesel generator average running time drops from 22.5 hours per start to 2.5 hours per start between case 1 and case 5.

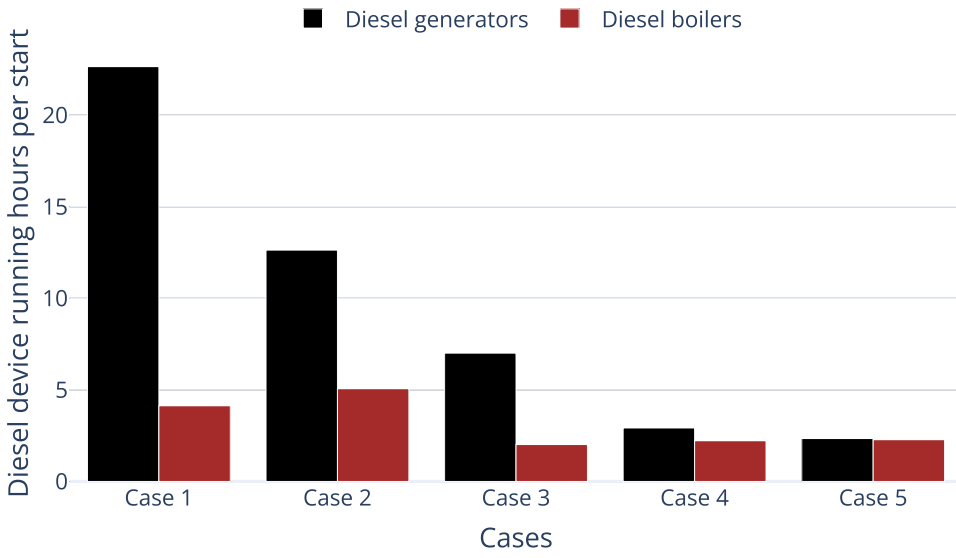

Figure 6.6: The average number of hours the diesel generator and diesel boiler devices are running per start up for the six simulated cases.

6.3 Energy usage

As there are no additional devices using heat in the cases, the heat consumption has the same value of $60.1 \cdot 10^3$ MWh per year for all scenarios. This is not the case for electricity consumption, however, as the battery, electric boiler, geothermal heat pump, electrolyser, and compressed hydrogen storage all add to the electricity demand. The yearly electricity consumption for the six cases are shown in Figure 6.7.

The current electricity demand for Longyearbyen is $44.9 \cdot 10^3$ MWh for all cases, and in the first case the battery uses 1100 MWh, bringing the total electricity consumption up to $46.0 \cdot 10^3$ MWh for the year. The typical use case for the battery is here to allow the diesel generators to operate at maximum efficiency by only having a generator switched on when it can run at full production. The difference between the maximum capacities of the generators that are switched on and the electric load is then used to charge or discharge the battery.

For the second case, the battery is used a bit more, bringing the total demand up to $46.4 \cdot 10^3$ MWh, which is 3.5% higher than the current electricity demand.

For case 3, with an electric boiler and a geothermal heat pump, the electricity consumption increases to $61.7 \cdot 10^3$ MWh, which is 37.5% greater than the demand currently covered by the coal power plant.

With the hydrogen production and storage system installed in case 4, the required electric energy drastically rises to $98.6 \cdot 10^3$ MWh, being an increase of 119.9% compared to the current demand.

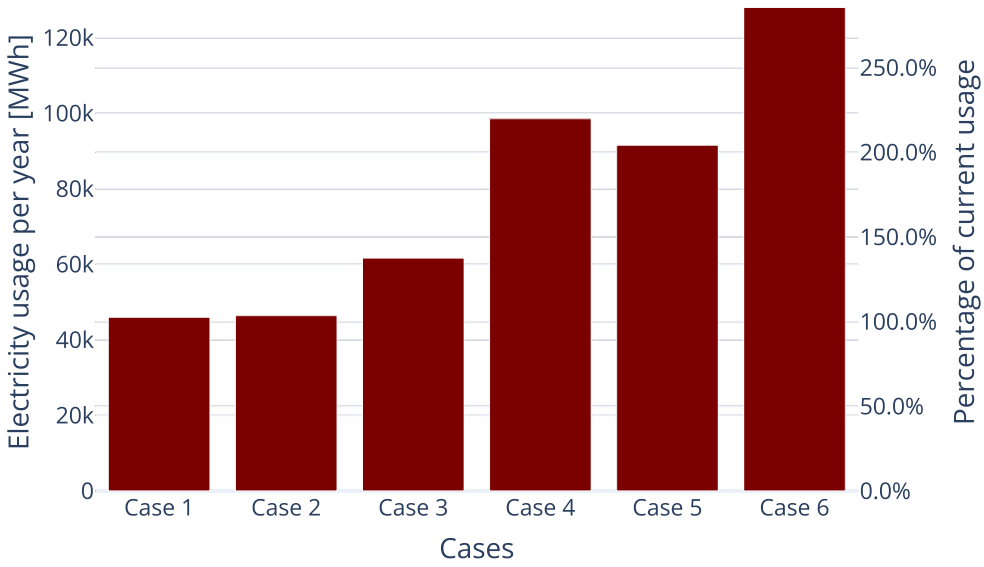

Figure 6.7: Yearly electricity consumption for the six simulated cases. The right axis shows the values as a percentage of the current electricity consumption.

As the offshore installation in case 5 has a smaller maximum production than case 4, the electric energy used in the hydrogen system is also lower, giving a total consumption of $91.5 \cdot 10^3$ MWh, an 104.2% increase from the current energy system.

Finally, the fully renewable case with larger wind, electric boiler, electrolyser, and compressed storage installations, uses $128.0 \cdot 10^3$ MWh over the course of the year, which is an increase of 185.6% from the current energy usage. While significant amounts of the increased electricity consumption in this case is related to providing the required heat energy of $60.1 \cdot 10^3$ MWh from renewable sources, a lot of the energy is simply lost in the round trip long term storage process.

Besides the absolute carbon dioxide emission values for each case, another central metric for the simulated cases is how much of the energy used is provided by renewable sources. Both the total energy demand and the renewable share of the energy production is given for each case in Figure 6.8.

As the first case only includes diesel devices to provide electric and heat energy, this scenario has a renewable share of 0.0%. The second case with photovoltaic cells gives a renewable share of 12.7%, while the third case with wind and electric heating devices added sees a climb to 60.5% renewable energy production.

The added hydrogen system in cases 4 and 5 gives an increase in the renewable share to 90.8% and 93.2% respectively. The more stable wind conditions offshore thus effectively outweigh the near halving of the installed wind capacity when it comes to how renewable the total energy system is.

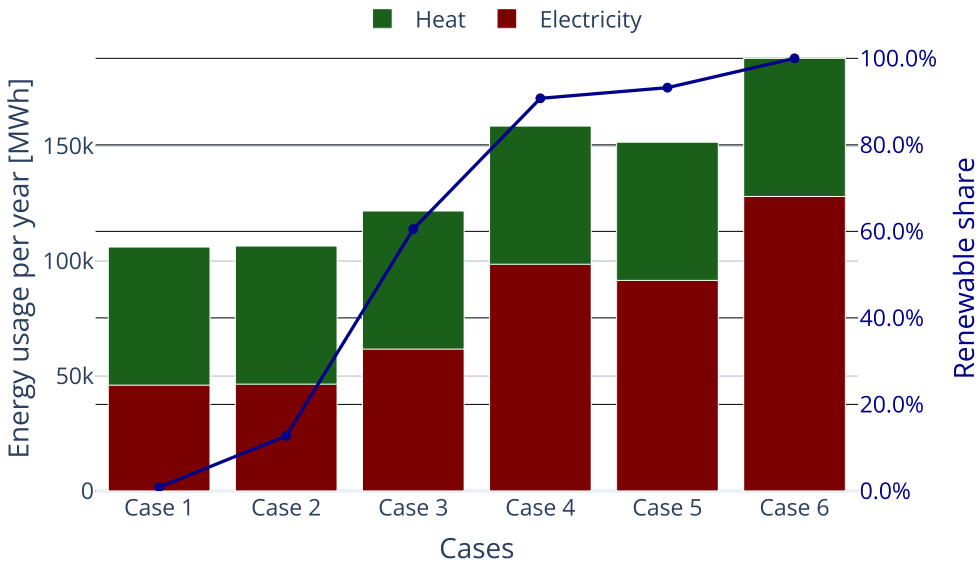

Figure 6.8: The combined energy consumption for each case with the share being covered by renewable sources plotted on the right axis.

Another end point for the produced energy besides storage and demand, is the curtailed energy that is produced but has no device that can make use of it in the current timestep. This energy is discarded, and though there is no significant curtailed electric energy for any of the cases, the curtailed heat energy is given in Figure 6.9.

As the electricity and heat demand profiles show in Figure 4.14, the demand for electricity and heat are nearly equal for the summer months. However, the diesel generators with waste heat recovery are able to supply more heat than electricity, as can be seen in Figure 5.1. For case 1, this yields the heat curtailment value of $1.3 \cdot 10^3$ MWh, which is 2.1% of the total heat demand.

For cases 2, 3, and 5 the discarded heat energy is nearly negligible, owing to PV and wind power supplying sufficient amounts of electrical energy to reduce the diesel generator output to levels where the waste heat produced is not more than demanded by the district heating system.

Case 4 has notable amounts of discarded heat energy, though, at $0.2 \cdot 10^3$ MWh and 0.4% of the total heat demand. This excess heat also mainly arises during the summertime, when periods of high wind and PV production yield more recoverable waste heat from the hydrogen electrolyser and compression than is required for the district heating system at the time.

Similarly, for case 6, with a larger wind farm the excess waste heat occurs in larger amounts and more frequently, giving $2.0 \cdot 10^3$ MWh, or 3.4% of the total heat demand, as discarded heat energy.

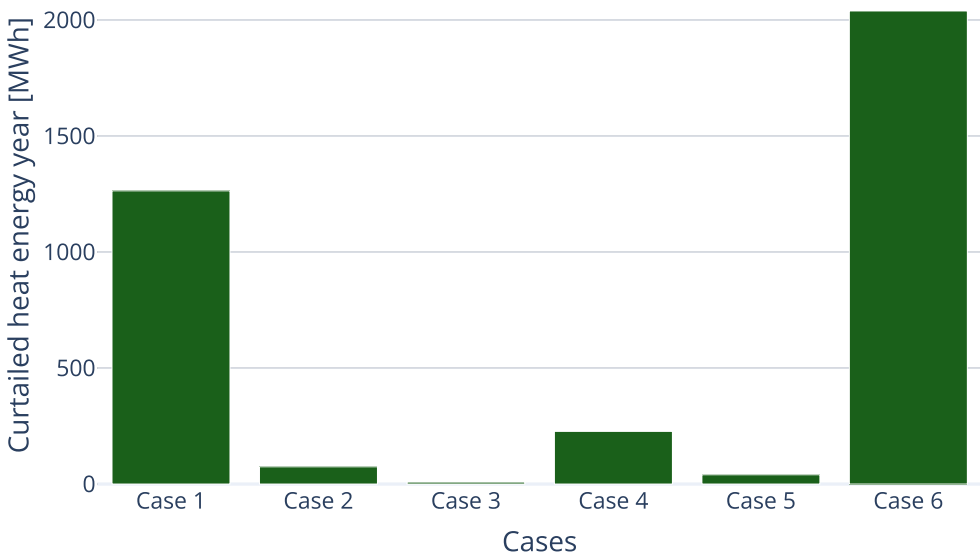

Figure 6.9: The curtailed heat energy for each of the six cases. This energy was recovered from waste heat, but not needed for the district heating system at the time and thus discarded.

6.4 Curtailed power production

Case 2 and case 3 includes intermittent power sources, but no long term storage options for timesteps with a larger electricity supply than demand. As a result, some of the potential power is curtailed, and not put into the energy network. The curtailed PV and wind energy for the two cases is shown in Figure 6.10.

For case 2, the curtailed electric energy from photovoltaic cells amount to $3.9 \cdot 10^3$ MWh, which correspond to 8.4% of the total electric energy consumption and 31.7% of the actually produced PV energy for the case. The absence of long term storage thus results in a significant waste of renewable potential.

In the third case, the installation of an electric boiler and the geothermal heat pump gives a greater opportunity for utilizing intermittent electric energy not required by the town. At timesteps with high intermittent power production, however, more renewable energy is available than is needed to cover both electricity and heating demands[1]. The result is $11.1 \cdot 10^3$ MWh of curtailed electric energy, which is 18.0% of the total electric energy consumption and 28.5% of the produced renewable electric energy. It is thus clear that significant amounts of available renewable energy is obsolete without forms of long term storage supplementing the intermittent sources.

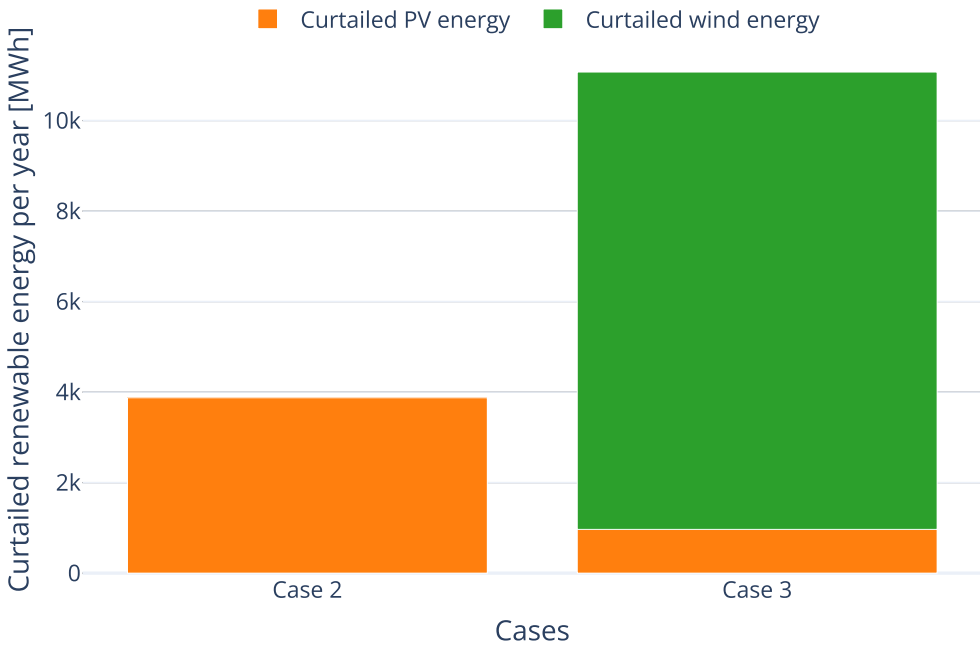

Figure 6.10: The curtailed PV and wind energy for the cases with intermittent sources and no long term storage.

[1]The electric boiler is in these cases preferred to use over the geothermal heat pump, giving a higher energy usage but lower curtailment values.

6.5 Hydrogen production

Long term energy storage is attained with the hydrogen system included in cases 4, 5, and 6. The timeseries showing the stored hydrogen levels are given in Chapter 5. For case 4, Figure 5.5, and case 5, Figure 5.6, the storage profiles are qualitatively similar, with large variations below a third of maximum capacity most of the year, and a more stable and much higher level in the summer due to the presence of PV power production. For the onshore case, however, the variations are greater, corresponding to the greater variation in wind combined with a larger turbine installation for this case. The more stable wind conditions for the offshore scenario, case 5, however, yield a greater summertime hydrogen production relative the smaller wind turbine installation.

For case 6, the fully renewable scenario, the hydrogen storage level exhibits smaller short term variations relative the maximum capacity, as shown in Figure 5.8. The storage is almost used up, however, before the summertime PV production and autumn wind production increases the levels again. The average storage level for this case is at 48.9%, significantly greater than the levels in case 4 and case 5, which are 28.1% and 24.3%, respectively.

The yearly production of hydrogen is given in Figure 6.11. Case 4 has a production (and usage) of hydrogen of $8.4 \cdot 10^6$ Nm^3 per year, while case 5 produces and uses $6.3 \cdot 10^6$ Nm^3. Thus the offshore wind farm case has both a smaller installation of wind turbines and uses less long term energy storage than the onshore case, while still yielding lower CO_2 emissions. The more frequent high wind power capacity factors for this case, and shorter periods with low capacity factors, more than make up for its smaller installation.

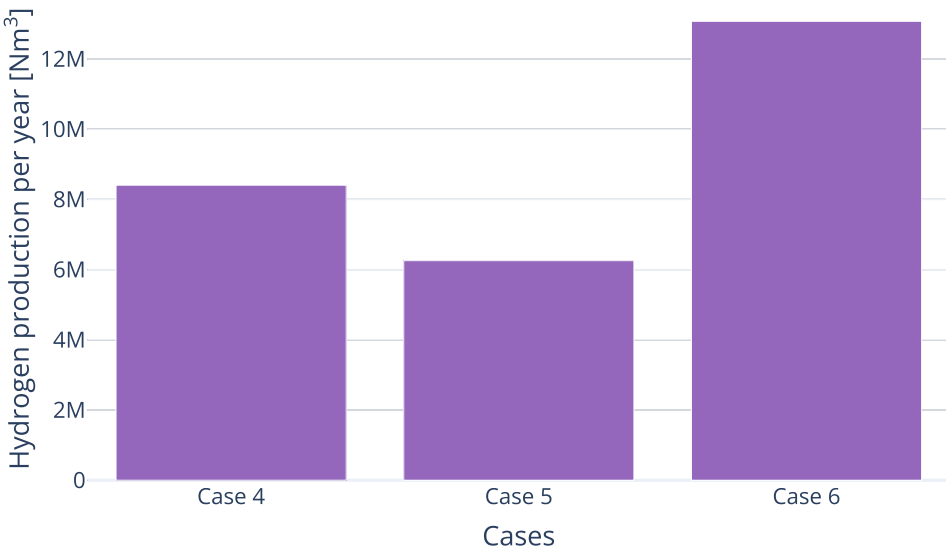

Figure 6.11: The produced hydrogen during the simulated year for the three cases including a hydrogen production and storage system.

For the fully renewable case, the hydrogen production and usage is $13.1 \cdot 10^6$ Nm^3 for the year, which gives a 55.5% increase in long term storage usage from case 4 in order to increase the renewable contribution to the energy system from 90.8% to 100.0%.

6.6 Energy loss

Up to now, curtailed energy has been discussed, and a mention has been made with regards to the loss of energy in the round-trip hydrogen storage process. Combined, in addition to the round-trip energy loss in the battery and the electric boiler energy loss from conversion from electricity to heat, the energy loss for each case is obtained and displayed in Figure 6.12. On the right axis the loss as a percentage of the total produced energy is given[2].

For the base case, the battery round trip energy loss adds up to 190 MWh, which, combined with the curtailed heat energy, gives an energy loss of 1 450 MWh, 1.4% of the produced electrical and heat energy in this case.

The second case sees an increase in battery energy loss to 270 MWh, while the large photovoltaic curtailment in this case brings the total wasted or lost energy to 4 200 MWh, 4.0% of the total produced energy.

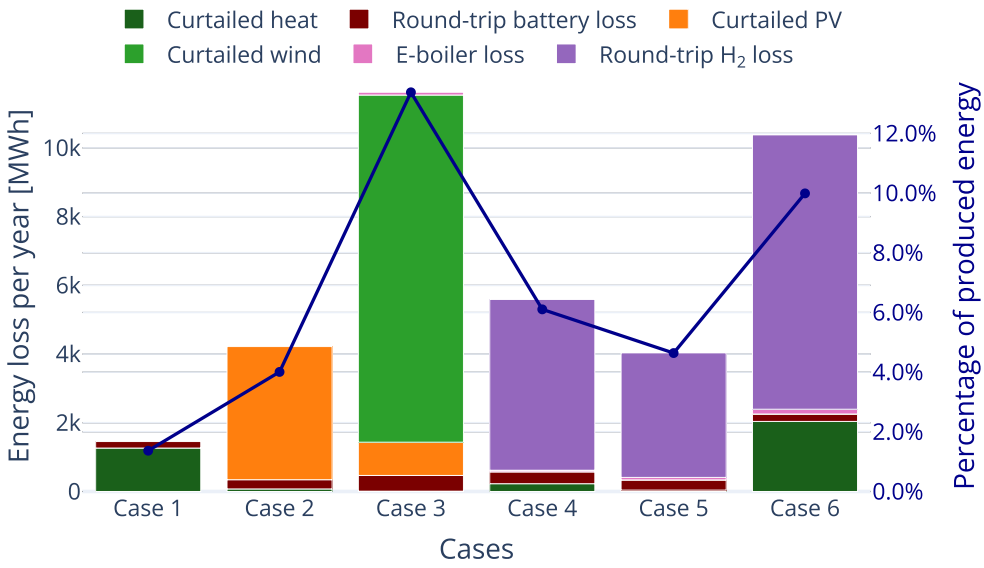

Figure 6.12: The yearly energy lost either due to curtailment or from conversion loss when converting electrical energy to heat or stored energy. On the right axis the energy loss is given as the percentage of the produced energy in each case.

[2]The geothermal heat pump device is not included in for the cases where it is installed. Only devices that give a electricity and/or heat as output with neither of these carriers as input are counted among the devices producing energy.

The wind farm installment in case 3 causes more battery usage, giving the device a round trip energy loss of 460 MWh. Along with the curtailed energy production, the total amount of energy that was not made use of or lost in the system before reaching the demand of the town was 11 600 MWh. This is as much as 13.4% of the entire electricity and heat production in the third case. As the majority of the lost energy is due to curtailment, long term energy storage is a necessary addition to make use of the available energy.

For the cases with electrolysers, compressed storage, and fuel cells, however, it is evident that long term hydrogen storage comes with its own challenges, energy-wise. The second law of thermodynamics yields that conversion between different energy forms increases the entropy of the system, consequently giving round trip processes energy losses [15]. While these losses are relatively small for the battery round-trip process, using electricity to create hydrogen gas, compress it, and then using a fuel cell to convert the gas back to electricity, will have major entropy increases, and thus energy losses, associated with it.

For case 4 the round trip efficiency is only 36.1%, meaning that close to two thirds of the electrical energy was lost in the process. The Longyearbyen energy system, however, can also make use of the lower quality energy produced in the round-trip process; the waste heat. The round trip efficiency of *usable energy* obtained from electrical energy input is 65.1%, greatly improving the prospects of the long term energy storage solution[3]. 5 000 MWh of input electrical energy is still completely lost in the hydrogen round trip process in this case, giving a total energy loss of 5 600 MWh, 6.1% of all produced energy.

The fifth case, with a smaller hydrogen production, naturally yields lower energy losses at 3 600 MWh, giving a total of 4 000 MWh and 4.6% of the produced energy in the offshore case. The electricity and usable energy round trip efficiencies increased to 36.2% and 65.3%, respectively, as a consequence of the lower storage level requiring less compressor usage and thus reducing electrical input to the hydrogen system.

The fully renewable case sees a climb in the hydrogen system energy losses to 8 000 MWh, giving the total loss of 10 400 MWh. It should also be noted that the 2 000 MWh of curtailed heat energy originate from the hydrogen system, as all of this heat energy is electrolyser waste heat that is beyond the heat demand. With losses constituting 10.0% of the total production, this case sees a significant loss comparable to that of case 3 with curtailed power and no long term storage, although the CO_2 emissions are reduced to zero in this case.

[3]The hydrogen system does give a large loss in *energy quality* when operating with the 65.1% efficiency figure, but since the heat energy is, most of the time, used by the district heating system, the hydrogen system can be thought of as having a purpose, along with the geothermal heat pump and electric boiler devices, to replace heating capabilities currently supplied by the coal and diesel systems.

6.7 Costs for each case

While a full cost analysis is not done for each case, the data for different types of expenses for each device obtained in Chapter 4 gives an estimate for how the different scenarios compare from a cost perspective. The cost for operating the current coal power plant is 92.3 million NOK[4] [71].

Figure 6.13 shows the yearly costs for each case. The investment costs for each device is the equivalent annual cost found using its lifetime and a discount rate of 4% as used in an earlier energy system report for Longyearbyen [7]. It is here evident that when annualizing the investment cost, the base case has the highest equivalent annual cost at 149.0 MNOK/year, of which there are no actual investment expenses. The fuel costs of 105.5 MNOK/year stem from the consumption of 13 500 Nm^3 (13.5 million liters) of diesel[5]. The base case will have yearly costs 61.4% higher than the current power plant operational costs.

For each following case the cost is reduced until the offshore wind farm case (5), at 85.0 MNOK/year, which is only 57.0% of the base case equivalent annual cost, and 92.2% of the current energy system cost. For the fully renewable case 6, however, the investment costs outweigh the savings from reduced diesel and CO_2 tax expenses, yielding the fourth highest costs at 101.5 MNOK/year, 10.0% greater than the coal power plant expenses.

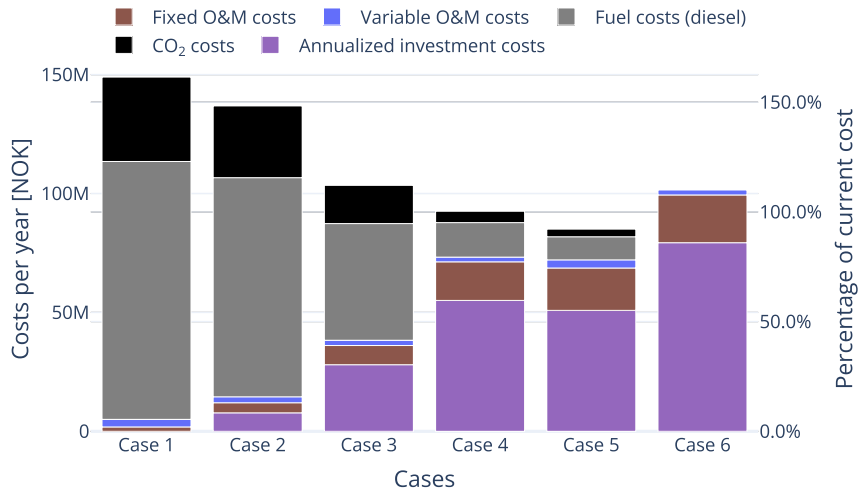

Figure 6.13: The yearly expenses for the six cases. The investment costs for each device is annualized using its lifetime and a discount rate of 4%. The expenses as percentages of the costs of the current power plant are shown on the right axis.

[4]The value is from 2020 and is adjusted to 2022 NOK using an inflation value of 5.84% [32].

[5]This value is higher than the estimated yearly need of just over 12 million liters [72]. The discrepancy comes from the simulated cases assuming the same energy demand as for the year 2018, while the estimated values from the community council likely take into account a demand reduction. As the details for the community council estimates are not publicly available, this will not be explored further than noting the similar diesel demands in the simulation done here, and the public estimates of Longyearbyen Community Council.

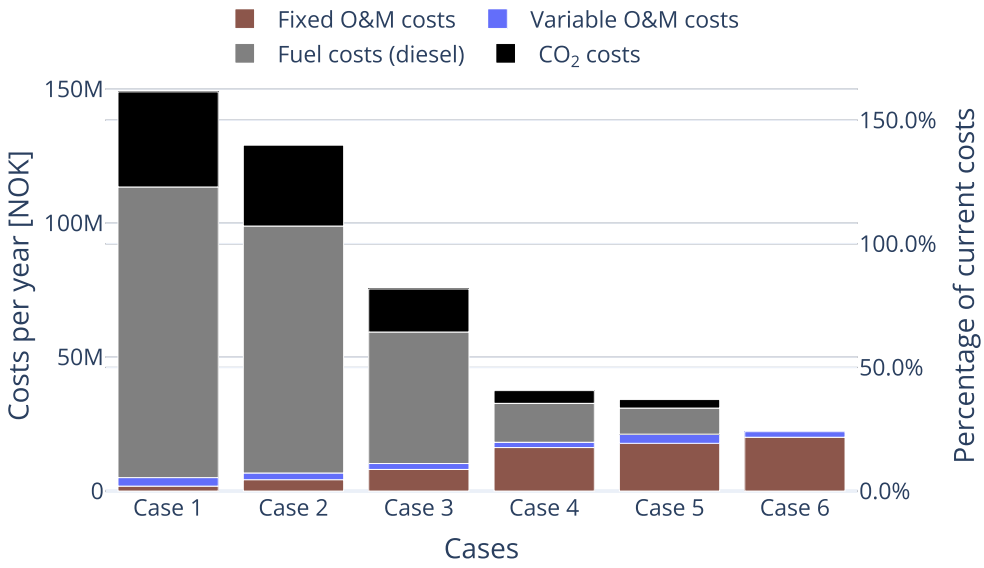

Figure 6.14: All the costs related to the operation of the installed devices for the six cases.

Given an investment into the installation of the devices for each case, the yearly costs for operating a scenario consists of fixed O&M costs, variable O&M costs, diesel costs, and the CO_2 tax. These expenses for the simulated year are illustrated in Figure 6.14. The diesel, and correlated CO_2, costs clearly constitute the greatest part of the expenses in the cases utilizing the diesel system, with the total yearly operational costs for the base case being, the same as in the previous plot, 149.0 MNOK. Although the fixed operational costs drastically increase with a larger renewable energy installation, the total yearly operational cost for the fully renewable case ends up being 22.2 MNOK, only 14.9% of the corresponding base case expenses and 24% of the current coal power plant yearly costs.

The lifetime of the battery, electric boiler, and compressed hydrogen storage devices are all found to be 20 years. Assuming the operational costs for the simulated 2018 year are representative for the foreseeable future[6], the total expenses for installation and 20 years of operation are given in Figure 6.15. Although the investment and fixed operation and maintenance costs for the renewable cases are significant, over two decades the base case diesel system gives higher fuel and emission tax expenses are greater than the total costs for all the other cases in the same time. Although none of the cases studied here correspond exactly to any of the alternatives investigated in the 2018 THEMA report [7], the total expenses for the longer time periods are of comparable magnitude, giving credence to the financial parameter values adopted for the simulations having reasonable values.

[6]The diesel price was in an earlier report taken to be unchanged until 2050 [7], and the other running cost parameters are also taken to be invariant for at least 20 years.

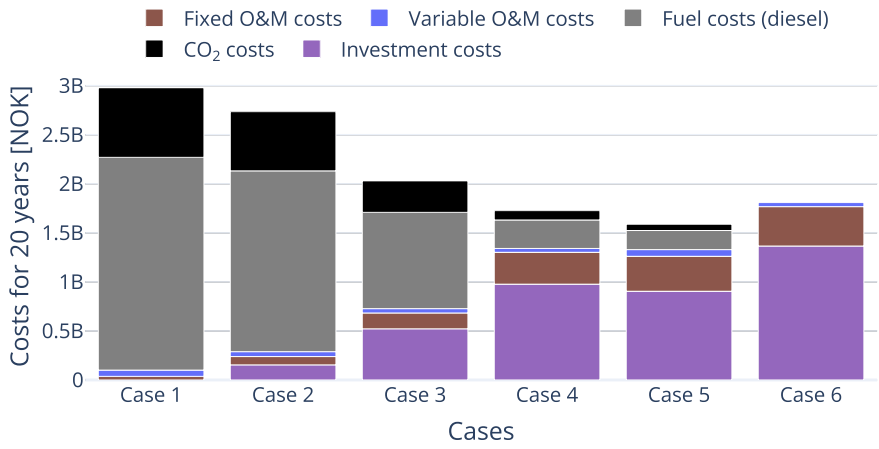

Figure 6.15: The total expenses for installing and operating each case for 20 years, assuming the running costs stay the same for all years.

As an example of how the costs arise internally in each case, Figure 6.16 gives the breakdown for case 4. This case includes all types of devices, and besides the investment costs, it is evident that the fixed operational and maintenance costs for most of the renewable devices exceed those of the diesel devices. The wind farm related expenses give the largest contribution to the total expense, 28.5% of the entire case cost. As both investment, fixed O&M, and variable O&M costs for wind installations are on the higher end compared to the other devices installed, the size of the wind farm is kept moderate in the cases with long term storage. Increasing the electrolysis and storage capacity to fully be able utilize maximum wind and PV production gives lower investment and operational costs than a slightly larger wind farm with less long term storage capabilities and similar CO_2 emissions.

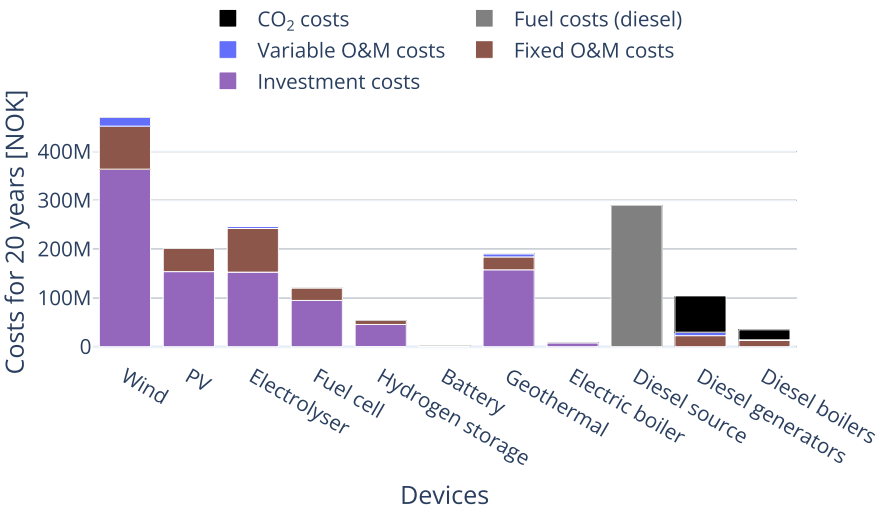

Figure 6.16: The per device investment and operational expenses for case 4.

6.8 The feasibility of the different cases

The base case, case 1, is the transitional energy system that will be fully operational from the autumn of 2023. This system is planned to only be temporary, however, due to both high fuel costs and significant carbon dioxide emissions. As a PV installation is among the cheaper options, modular, and is already being implemented on several buildings and structures in the town, this device is included in all cases with renewable energy production. Fully installing the 25 MWp photovoltaic cell capacity could, without affecting any of the landscape besides the cladding on existing structures, reduce the emissions from the base case by 15.0 %, reduce the equivalent annual cost by 10.8%, and bring the renewable energy share up to 12.7%. By complementing the diesel system, the diesel generators in addition reduce the running hours, increasing the lifetime of this system as well. The second case is thus, based on the simulations in this work, deemed very feasible, and it can be gradually implemented as modules regardless of potential other renewable energy device installations.

For significantly increasing the renewable energy supply, however, it is necessary with electricity and heating devices that can also cover demand during the polar night, when the need is greatest. The geothermal heat pump project could cover a large part of the heating demand with its wintertime 5.2 MW output requiring 1.3 MW of input electric power. To cover the remaining demand a 5 MW electric boiler can be installed, though it would require slightly more electric input power than it can deliver to the district heating system as heat. Both of these devices, however, would increase costs, and the electric boiler would also increase emissions, if used in combination with the diesel generators when no renewable electricity is available. Thus, there is a need for renewable electricity production during the winter season, and the local source chosen in this project is wind power. A small wind turbine farm consisting of 5 turbines yielding an installed capacity of 17.25 MW is installed on the Breinosa mountain in case 3. This area has an existing road connection and is the site of the current coal mine and several research facilities. Besides being already industrialized, the mountain is also sufficiently inland to not have the sprawling wildlife like the bird cliffs along the coast exhibit in the summertime. Case 3 manages a 54.8% reduction in CO_2 emissions compared with the base case, while the renewable energy share increases to 60.5%. The reason for the emissions not being reduced correspondingly much, stems from the electric heating devices causing in an increase in the total energy demand of 14.8% from the base case. The equivalent annual cost is also reduced a significant 30.6% from the base case. Wind power, however, is very intermittent, often being able to produce significantly more or less than required at any moment for such a small grid as Longyearbyen. Case 3 gives a curtailed renewable electric energy for the year of $11.1 \cdot 10^3$ MWh, which equals 18.0% of the electric energy usage in this case. Furthermore, the total energy losses, due to the high curtailment values, equal 13.4% of the total produced energy. Even though the case exhibits significantly reduced emissions and equivalent annual costs compared to the base

case, the high proportion of wasted energy combined with the fact that wind farm installations have relatively high costs compared to the other devices inspected, and the non-negligible landscape altering, leads it to be considered less feasible than case 2.

The missing part in the previous case, is long term energy storage, which is essential for supplying an energy grid based off of intermittent energy sources. Case 4 addresses this shortcoming with the increased onshore wind farm installation of 9 turbines for a capacity of 30.05 MW, as well as the installation of a 35 MW electrolyser, a 10 MW fuel cell, and a 1 200 000 Nm^3 hydrogen storage facility. With an electrolysis capacity that can convert about two thirds of the maximum electric power from both the wind farm and PV installation combined into hydrogen for storage (and recoverable waste heat), there is no renewable energy curtailment in this case. Even though the total energy usage increases by 49.6% from the base case, the redistributive effect of the long term storage gives a renewable energy share of 90.8% and an 86.6% reduction in emissions from case 1. The reduction in equivalent annual cost is also a drastic 37.9% from the base case, owing to the major reduction of fuel and CO_2 costs in this scenario. At 92.5 million NOK, this case exhibits a lower total equivalent annual cost than the yearly fuel costs in the base case, and only marginally higher costs than the current coal power plant gives. With similar landscape alterations as in case 3, but with lower emissions, lower equivalent annual costs, and no wasted renewable energy[7], this case is deemed a very feasible alternative for drastically reducing the emissions in the town.

Case 5, while very similar to case 4, considers an offshore wind farm installation of 5 turbines at the Røvigflaket shallows near Isfjord radio. The much more favorable wind conditions at this location gives very similar emission and renewable share values as for case 4, but with only a bit over half of the installed wind capacity and consequently a smaller elctrolysis installation. The offshore wind turbines have higher investment and operating costs, however, and the final equivalent annual cost is only 8.1% lower than case 4 despite the much lower capacity installations. A big drawback of this case is the offshore wind turbine location, which is in an area with very limited human intervention, close to bird cliffs rich in wildlife in the summertime. In addition, complications regarding drifting sea ice make the financial parameters highly uncertain for this case. The aggregate of these drawbacks yield the fifth case infeasible in comparison with the other cases.

In order to create a fully renewable scenario, the sixth case modifies the fourth case by discarding the diesel system in favor of expanding the onshore wind farm to contain 13 turbines with a combined installed capacity of 44.85 MW. To take advantage of the high wind production periods, the electrolyser capacity is consequently increased to 50 MW and the storage capacity is increased to 4 million Nm^3. To cover the 5 MW electric reserve requirement without the diesel system, the fuel cell installation is scaled up to 15 MW. Similarly, to always meet the 5 MW heat reserve requirement, the electric boiler installation is doubled to 10 MW. The

[7]Though, of course, the hydrogen system has significant round-trip energy losses.

simulated year now uses 100.0% renewable energy, while the energy usage has increased by 77.4% from the base case. The scale of this hydrogen system, although making a fully renewable system possible, gives total energy losses of 10% of the, relatively large, energy production. Even though the yearly operational costs at 22.2 MNOK and 14.9% of the base case is the lowest of all cases, the equivalent annual cost for the installation and operation at 68.1% of the base case is 9.7% greater than the corresponding cost for case 4, and 10.0% higher than the current power plant operational costs. Costs related to the large wind farm installation, thus end up being greater than the what is saved in fuel and CO_2 expenses. Due to the much higher investment cost and higher equivalent annual cost than case 4, and with a relatively small emission reduction compared to that case, the sixth case is deemed less feasible than case 4.

One further factor that make case 4 and 6 more viable, is the requirement for energy security for the off grid settlement. With a wind farm consisting of 9 or 13 turbines, there is still high production capacity should a few of them malfunction at the same time. The same applies to the geothermal heat pump installations, which contain 13 individual wells. Similarly, the modular nature of the PV, electrolyser, and fuel cell installations give a high redundancy and energy security for these devices. The hydrogen storage facility will also consist of several storage tanks and, as the full capacity is rarely approached in these simulations, thus have redundancy as well. A further note on the hydrogen long term energy storage system is that hydrogen could also be imported from the mainland if needed. Hydrogen import from northern Norway was studied by Statkraft in 2018 [8], and in 2020 the discussed hydrogen production from the Raggovidda wind park began [73]. As a last resort energy redundancy, the current non-renewable diesel system will still be in place with its own redundant production of both electricity and heat. Thus, the energy security aspects of the cases with long term hydrogen storage make those alternatives even more appealing, on top of the reduction of carbon dioxide emissions and equivalent annual costs.

Chapter 7

Discussion of the modelling approach

The main topic aimed to be researched in this work, is how an energy system based upon wind power and hydrogen could look for the remote, Arctic, off grid settlement of Longyearbyen. Additional energy sources and systems have been included in the study, and different alternatives have been simulated for one year to take into account the large seasonal variability of both the supply and demand for both electricity and heat in the town.

7.1 The chosen modelling framework

A combined heating an electric system has here been modeled by expanding and modifying the Oogeso python package. With hydrogen and diesel as energy carriers as well as electricity and heat as energy flows, a variety of system *devices* that can supply, expend, or both supply and expend different energy carriers and flows are defined according to a set of constraints. These devices were explained in some detail in Chapter 3, while the full implementation is freely available as well [23].

This model creates a set of linear equations with both continuous and integer variables based on the aforementioned device constraints. These equations must then all be satisfied for all timesteps in a time horizon, here 240 timesteps, while an objective function, here the running costs, is minimized. The solution obtained is for 240 timesteps, but after 24 timesteps the optimization is again done for the next 240 timesteps. The *mixed integer linear programming* (MILP) optimization problem with a rolling horizon thus takes into account a set of initial conditions and device parameters, and simulates the resulting energy system evolution over time.

With timesteps of one hour, the simulation has a forecast of 10 days for the devices with associated profiles, and every day the simulation is thus reran with hourly resolution for the subsequent 10 days. An advantage of this approach,

rather than optimizing for the entire simulation time, which is one year in this case, is that the device profiles become analogous to actual forecasts. As the profiles of for example wind and PV power production, as well as profiles for the electricity and heating demands, are not known a year in advance, simulations optimizing the full year at once may not make the same energy flow decisions for each timestep, especially with regards to energy storage, as a rolling horizon optimization would. Rather, a more realistic approach, is knowing the current status of parameters like energy storage levels, and having a good forecast for available production and demand in the near term. This approach thus finds the best choice for meeting the heat and electricity demand with the available energy system devices and expected intermittent production and demand in the short term, which is just like the decision needing to be made by the energy supplier in the town. The model can as such, as is one of its intended functionalities, be used as a real-time decision aid, and the results are thus a realistic representation of how different renewable technologies would fare as part of the energy mix on Svalbard.

A disadvantage of the current simulation, however, is that long term predictable seasonal variability is not fully implemented. While wind production and electricity consumption varies greatly and unpredictable throughout the year, it is well established that there will be significant PV production potential in the months with midnight sun, and none in the months of polar night. Similarly, the heating demands will be predictably about two times as high in the winter as in the summer. These are factors that may affect the decisions taken in a real life energy system.

Take, for example, a case where the long term energy storage is down to half of the maximum capacity, and there are two renewable alternatives to meeting the demand; one alternative being more energy efficient, and the other being cheaper. If it is mid-spring, an operator would know that renewable electricity production will greatly increase in the coming months while the energy demand will decrease, and perhaps a reduction in the current hydrogen storage is needed to be guaranteed to avoid curtailing curtailing renewable production in the summer[1]. All these considerations make the best choice to use the cheapest alternative. If the situation occurs during mid-autumn, on the other hand, it is known that future demand will increase and that the potential for increasing the storage will decrease with the decreasing hours of sunlight, and that the storage level is likely too low to make it through the winter. With these considerations in mind, the best choice is using the more efficient alternative in order to postpone having to start the diesel system, which is even more expensive, for as long as possible.

The alternatives in the above case will, if no target profile is specified for the hydrogen storage device, look identical to the model, which will choose the cheapest alternative for all timesteps. When the long term storage would, with only choosing the cheap alternative, run out within the 10 day simulation hori-

[1]Curtailment in the cases with hydrogen storage is after all only avoided as long as there is capacity in the hydrogen storage tanks so that the electrolyser can operate.

zon, however, the model will start making the more efficient choice to postpone having to use the expensive backup devices. This will be after the simulated system has already wasted stored energy that would predictably have been cheaper to keep stored in the long term.

As indicated, though, specifying a target profile for the hydrogen storage will also affect the optimal choice at each timestep. Thus, although known seasonal variability of energy sources like photovoltaics and energy sinks like heat demand are not directly taken into account in the model, the assumed effect of this variability on energy storage can currently be used in the optimization. As given in Chapter 4, the target hydrogen storage profile in all modeled cases here is simply a sinusoidal function with its maximum towards the end of the period with PV production and low heating demands, and the minimum towards the end of the period with no PV production and high heating demands. Because a term in the objective function scales with how far the storage level is below the target level, the more efficient alternative will be chosen if the storage level is significantly below the target level for the given timestep.

7.2 The parameters used in the Oogeso model

While the majority of the parameters affecting both the optimization and analysis were obtained from external sources and listed in Chapter 4, other parameters were decided based on the scope of the work and to create simulation cases distinct in both emissions and costs.

7.2.1 Diesel fuel costs

The cost for diesel fuel has, in the simulations and equivalent annual cost calculations, been assumed in the coming decades to be the same as the cost was in 2018, as assumed in a Svalbard energy system report from the same year [7]. Through the course of this work, however, the global energy situation has drastically changed, and the diesel costs have greatly increased. In addition to a more volatile price in the present, the future price predictions have a much greater uncertainty connected to them. The forecasts for the coming years, however, contain significantly higher diesel costs than previously assumed [74]. A considerably higher price for diesel fuel would make each numbered case studied in this work have more favorable equivalent annualized costs compared to the lower numbered cases, as the yearly diesel usage decreases for each simulated case. The more renewable cases would thus seem even more favorable than the less renewable cases than the current simulations show. Due to the, at the time, very high uncertainty when it comes to future costs of diesel, the value from the 2018 report has been used in the simulations carried out here.

7.2.2 CO_2 emissions

All devices in the modeling framework have the parameter $CO_{2,em}$ that specify the carbon dioxide emissions per flow of the default flow variable of the device[2]. In this work, however, only emissions from the consumption of diesel by diesel generators and diesel boilers are calculated and counted towards the total system emissions, with $CO_{2,em}$ having the default value of 0 for all devices. There are likely emissions related to the operation of other devices as well, though. Such emissions have been assumed to be negligible in the grand picture compared to the diesel emissions, and sufficiently independent of variable device flow to not have an impact on the optimization of the studied cases. Another source of CO_2 emissions that are not negligible, but still not impacting the optimization, are related to the installation of the different cases. These will be varying and considerable in magnitude, though no attempt to quantify them has been made in this work.

7.2.3 Wind farm dimensioning

In order to maintain a high degree of redundancy in the electricity supply, all cases with wind farms are chosen to have at least 5 independent wind turbines. The only parameter that must be decided per case is then the actual number of turbines. This was done with the aid of PyPSA, which is an optimization model that can find the optimal installation capacities of different devices in an energy system [75]. A previously configured version of this model, PyPSA-Longyearbyen [76], was further extended using the data for PV, wind, electric demand, and heat demand from Chapter 4. With simplified implementations of the renewable energy devices, the model found the necessary wind installation for a fully renewable system to be 15 turbines for the onshore case, and 8 turbines for the offshore case. These values were then scaled down to cases that were not fully renewable in the Oogeso model, which also includes the existing diesel system. This downscaling of installed capacity in cases 4 and 5 was chosen such that there would be significantly smaller variable and fixed wind farm expenses, while also allowing smaller hydrogen production and storage investments. Despite the downscaling, the installed wind farms in those cases were still large enough to be capable of, in a timestep with maximum capacity factor, fully cover the demand of the town.

7.2.4 Hydrogen system and electric heating

The size of the fuel cell was chosen to be 10 MW to be able to supply the demand of electricity and heat, in conjunction with the electric heating devices, on any timestep given enough hydrogen storage. Similarly, the electric boiler was chosen to be 5 MW in order to be able to supply the heat load for the majority

[2]Though the carbon dioxide flow variable calculation is easily modifiable as an alternative to use other flow variables as well.

of the timesteps in conjunction with the 5.2 MW geothermal installation[3], given enough electric power available. For the fully renewable case, however, both of these device capacities were increased by 5 MW to also have the required electric and heating reserve requirements available from renewable devices.

The electric boiler is much cheaper than the geothermal installation, using the financial data in Chapter 4. Thus, the discussion around long term energy storage and two alternatives to cover the demand, one cheap and the other efficient, comes into effect. The dimensioning of the wind farm, hydrogen electrolyser, and compressed hydrogen storage is thus dependent on the target hydrogen storage level. The implementation of the target profile for the device had a significant impact on the necessary installations for the different cases, compared to having no such target profile.

For case 4, the system became efficient enough to reduce the turbine count from 10 to 9, while still reducing emissions by 1.2%. The total electricity consumption was reduced by 7.1%, and the electrolyser installation could be reduced by 12.5% to 35 MW. The hydrogen storage level, however, was increased by 50% to 1.2 million Nm^3 to accommodate the more efficient energy usage. The indirect implementation of predictable seasonal variety handling thus could significantly reduce both the investment and operational costs, while also slightly reducing emissions.

Case 5, which was already chosen to have similar emissions as case 4 but with an offshore wind farm, was already on the minimum turbine count before the implementation of the hydrogen target profile. The more efficient hydrogen usage thus didn't alter the chosen production capacity of a 25 MW electrolyser, but the storage was similarly increased to 1.2 million Nm^3. This gave emission reductions of 23.0%, and hence in total cost reductions due to correspondingly lower fuel and CO_2 costs.

The fully renewable case 6, which due to the large hydrogen storage capacity often chose the cheap heating alternative because the storage for most timesteps wouldn't run out within the optimization horizon with this choice, had the most to gain from the target profile implementation. The number of wind turbines could be reduced by 13.3% from 15 to 13, consequently giving an electrolyser reduction of 16.7% to 50 MW. While the total hydrogen storage was left unchanged at 4 million Nm^3, the total electricity consumption and hydrogen production was reduced by 11.3% and 13.9%, respectively. With such significant cost reductions following from the reduced installations, the fully renewable case became a considerably more viable alternative for the energy system in Longyearbyen.

The above finding illustrates the importance of high seasonal variability when simulating mixed energy systems with several alternatives for covering energy demands at every timestep. For self-sustained off grid energy systems, such predictable long term variability is key to consider in order to appropriately scale the components of the system.

[3]The hydrogen fuel cell or electrolyser could supply the remaining amount on the few timesteps heating demand exceeded 10.2 MW

7.3 Further work

While the current model both functions as a tool for studying the feasibility of various potential energy systems for Longyearbyen and a decision aid in operating such a system, it could be improved in several areas. Constraints for the devices could be adjusted or added to more accurately simulate desired behavior.

One possible modification is in regard to the diesel generators. Store Norske has indicated that the typical diesel generators present on Svalbard have an optimal power delivery when operating at about 75% of their capacity, which is currently not supported within the model. The current linear relationship between fuel consumption and output power for the device gives the maximal efficiency at either no production, maximum production, or at all production levels. Implementing for example a piecewise linear relationship as a device constraint instead is a possible modification, though time has not been found to investigate it in this work as the aim was mainly to model renewable devices.

Another important model feature to further investigate is implementing a parameter for the predicted seasonal variability of a source or sink device. While the indirect method employed on the long term storage device significantly improved the results, it required assuming the impact of the seasonal variations on the storage level at every timestep. For the current case using two predictable timeseries that affect the storage level in the same direction at the same timesteps gave a reasonable simple estimation, but adding more complicated predicted timeseries make the process in general non-trivial. A possibility for further improving the optimization could be to accept an optional predicted profile for each relevant device, and have the model, based on those profiles and additional storage parameters and bounds, create an estimate for a long term storage target profile to be used in the optimization.

A final thing to consider for further developing the model would be to add additional devices. Some power generation devices that possibly could be investigated for the coastal settlement are wave and tidal power generators[4]. Other short to medium term energy storage devices that could be implemented are hot water, hot rocks, and molten salt storage, all of which store heat energy.

Besides improving the functionality of the optimization model, further work could also be done in regards to choosing the parameter values used in the model. While some values wereassumed to be negligible or obtained from reports and assessments specific to the Longyearbyen energy system, the majority of the parameter values come from international studies and predictions, in some cases for large-scale applications. Costs, for example, are generally found to be higher for projects on Svalbard due to the remote, harsh Arctic environment. More realistic values would naturally yield more realistic results, so verifying the validity of the currently chosen parameter values, and potentially altering them, is a good ob-

[4]For such devices, analysis of their viability in areas with sea ice should also be done. The technology is however not considered mature enough for inclusion in this study of near term renewable energy installations for Longyearbyen.

jective for further work.

A final notion on topics for further work on the local model, is assessing whether different energy systems are politically feasible and environmentally justifiable in the delicate Arctic nature, especially with regards to potential offshore wind turbine installations.

On a more global level, it is important to note that there is nothing inherent in the simulation model itself that ties it to the Longyearbyen energy system properties. Using weather measurement data and energy demand timeseries from other closed energy systems, the model can simulate and optimize various renewable installations for those systems as well. There are over 1500 off grid energy systems in the polar regions, and Store Norske has ambitions, along with the University Centre in Svalbard (UNIS) and other industry in Longyearbyen, of establishing Longyearbyen as a knowledgebase for developing and exporting hybrid and renewable energy solutions to such communities [77]. The Oogeso simulation model expanded here models off grid systems, and with the focus on long term energy storage and seasonal variability, the model is typically tailorable to the energy systems of polar communities. In addition to implementing more direct predictable seasonal variability handling, an idea for further work is thus also to apply the model to other settlements to assess its applicability for simulating a general of grid polar energy system.

Chapter 8

Conclusion

The renewable energy transition of the Longyearbyen settlement on Svalbard creates challenges to meet the electricity and heating demands of the town using variable energy sources. While the current coal power plant and transitional diesel system are fully controllable, the intermittent nature of photovoltaics and wind power necessitate long term energy storage systems to be able to fully utilize such electrical energy sources.

In this work, potential future energy systems for Longyearbyen have been simulated for a full year of operations by extending the Offshore Oil and Gas Energy System Optimisation (Oogeso) python package. This package, which solves a mixed integer linear programming (MILP) optimization problem with a rolling horizon, was extended to include diesel generators and boilers, as well as compressed hydrogen storage using compression properties of hydrogen gas under the isothermal and adiabatic regimes. Further energy devices included in the mixed energy system were wind farms, photovoltaic installations, battery packs, geothermal heat pumps, electric boilers, hydrogen electrolysers, and hydrogen fuel cells. The wind power timeseries was obtained by using actual measurement data for the year 2018 from several weather stations, scaling it up to the turbine height using the logarithmic wind profile, and then combining it with the production power curve for a specific turbine. The photovoltaic capacity timeseries was obtained from a global weather model for the same year, while the seasonal variations in the capacity for a geothermal installation was provided by Store Norske. Using timeseries from 2018 for the electricity and heat demands of Longyearbyen, and a simple estimation for the ideal hydrogen storage utilization timeseries, the optimal flow of energy and energy carriers in hourly resolution was reoptimized every 24 hours for the upcoming 10 days using 10 days of the timeseries data. The simulation thus operated with a forecast, approximating real life scenarios where near-term production capacity and load estimations are used for making the present decisions on optimal flow in a mixed energy system.

With this optimization model, six different cases were simulated and compared, ranging from the already politically authorized transitional diesel and battery system, to a fully renewable case based on photovoltaics, wind power, geo-

thermal heat pumps, and hydrogen systems for long term storage. The first, diesel based case achieved a carbon dioxide emission reduction of 54.5% compared to the current coal power plant, which is the same as the estimates from the Longyearbyen Community Council for the base case, lending credence to the model. The preliminary estimates for costs in this case ended up at 149.0 million NOK per year, of which 143.9 million were for the diesel fuel and correlated CO_2 tax. With the introduction of a 25 MW photovoltaic installation, a 31.05 MW onshore wind farm, a 5.2 MW geothermal installation, a 5 MW electric boiler, and a hydrogen system with compressed storage capacity for 1.2 million normal cubic meters (Nm^3) hydrogen gas ($\approx$ 107 900 kg), the emission reduction from the current coal system was 93.9%. With the investment cost estimates annualized using the expected lifetime for each device and a discount rate of 4%, the equivalent annual cost of this case ended up being 92.5 MNOK, which is a reduction of 37.9% from the base case and the same as the annual costs of operating the current coal power plant. While an offshore variant of this case with a wind farm of only 17.5 MW achieved a slightly better emission reduction of 96.9% due to significantly better wind conditions, the more expensive investment and operation and maintenance costs for such an installation resulted in a comparable equivalent annualized cost of 85.0 MNOK. Due to relatively small estimated emission and cost improvements, combined with the higher uncertainties around environmental, political, and economic factors related to offshore installations in the harsh Arctic environment, an offshore alternative is found to be less feasible and realistic than an onshore alternative with similar emission rates. A fully renewable onshore alternative is then simulated, primarily by increasing the wind farm installation to 44.85 MW and the compressed hydrogen storage capacity to 4 million Nm^3 ($\approx$ 360 000 kg). While this case has no carbon dioxide emissions, the increased investment and operation and maintenance costs outweigh the fuel related savings compared with the previously mentioned onshore wind farm alternative, ending with an equivalent annual cost of 101.5 MNOK This is still 31.9% lower than the yearly costs for the base case, while being 10.0% higher than the current yearly power plant costs. If the diesel costs end up being considerably higher than assumed in the model, however, the yearly costs for the more renewable cases, and especially the fully renewable cases, would seem significantly more favorable than they already do compared to the base case.

The modeling approach for the combined energy system of the remote off grid settlement of the town of Longyearbyen undertaken in this thesis show that an extension of the system focused around the inclusion of photovoltaic cells, geothermal heat pumps, an onshore wind farm, and a hydrogen production and storage system does not only give the prospect of greatly reducing greenhouse gas emissions from the settlement, but it is also anticipated to considerably lower the costs of energy production while providing several layers of redundancy and energy security.

Bibliography

[1] T. B. Arlov, *Svalbards historie*. Tapir, 2003.

[2] Longyearbyen Community Council, *Produksjon ved Longyear Energiverk*. [Online]. Available: https://www.lokalstyre.no/produksjon.545701.no.html (visited on 2022-03-17).

[3] Longyearbyen Community Council, *Lokalsamfunnsplan for Longyearbyen 2022-2033*, 2022-04-06.

[4] United Nations General Assembly, *Transforming our world: the 2030 Agenda for Sustainable Development*, 2015-10-21.

[5] K. O. Ingerød, 'Longyearbyen Lokalstyre tar klimagrep,' 2021-11-03. [Online]. Available: https://www.lokalstyre.no/longyearbyen-lokalstyre-tar-klimagrep.6419643-321755.html (visited on 2022-03-17).

[6] Longyearbyen Community Council, 'Energiomstilling,' 2021-07-05. [Online]. Available: https://www.lokalstyre.no/energiomstilling.509607.no.html (visited on 2022-05-23).

[7] M. Thema, 'Alternativer for fremtidig energiforsyining på Svalbard,' 2018-06. [Online]. Available: https://www.regjeringen.no/contentassets/cdaceb5f6b5e4fb1aa4e5e151a87859a/thema-og-multiconsult---energiforsyningen-pa-svalbard.pdf (visited on 2022-04-27).

[8] G. M. Brekke, 'Fornybar energiforsyning til Svalbard,' Statkraft, 2018-11-09.

[9] The University Centre in Svalbard (UNIS). 'AGF-353 Sustainable Arctic Energy Exploration and Development.' (2021), [Online]. Available: https://www.unis.no/course/agf-353-sustainable-arctic-energy-exploration-development/ (visited on 2022-06-02).

[10] T. Foken, *Micrometeorology*, Second edition. Springer Berlin Heidelberg, 2017, ISBN: 9783642254406.

[11] M. Salby, R. Pielke and R. Dmowska, *Fundamentals of Atmospheric Physics* (ISSN). Elsevier Science, 1996, ISBN: 9780080532158.

[12] R. Stull, *An Introduction to Boundary Layer Meteorology* (Atmospheric and Oceanographic Sciences Library). Springer Netherlands, 2012, ISBN: 9789400930278.

[13] R. Fleagle and J. Businger, *An Introduction to Atmospheric Physics* (ISSN), Second edition. Elsevier Science, 1981, ISBN: 9780080918228.

[14] M. Jacobson and P. Jacobson, *Fundamentals of Atmospheric Modeling*, Second edition. Cambridge University Press, 2005, ISBN: 9780521839709.

[15] P. C. Hemmer, *Termisk fysikk*, Andre utgave. Tapir Akademisk Forlag, 2002, ISBN: 9788251917391.

[16] A. Barber, *Pneumatic Handbook*, Eigth edition. Elsevier Science, 1997, ISBN: 9780080514123. DOI: https://doi.org/10.1016/B978-185617249-3/50002-7.

[17] E. W. Lemmon, M. L. Huber and J. W. Leachman, 'Revised Standardized Equation for Hydrogen Gas Densities for Fuel Consumption Applications,' *Journal of research of the National Institute of Standards and Technology*, vol. 113, no. 6, pp. 341–350, 2008, ISSN: 1044-677X. DOI: https://doi.org/10.6028/jres.113.028.

[18] E. Ludwig, *Applied Process Design: For Chemical and Petrochemical Plants* (Applied Process Design for Chemical and Petrochemical Plants). Gulf Professional Publications, 2001, ISBN: 9780884156512. DOI: https://doi.org/10.1016/B978-1-85617-249-3.X5000-4.

[19] H. G. Svendsen, *Offshore Oil and Gas Energy System Optimisation (OOGESO) Documentation*, 2022-03-15. [Online]. Available: https://github.com/oogeso/oogeso/blob/master/docs/_static/oogeso_manual.pdf (visited on 2022-05-09).

[20] H. G. Svendsen and M. D. Aslesen, *Offshore Oil and Gas Energy System Operational Optimisation Model (oogeso)*, 2022. [Online]. Available: https://github.com/oogeso/oogeso (visited on 2022-05-09).

[21] H. G. Svendsen, 'Optimised operation of low-emission offshore oil and gas platform integrated energy systems,' 2022-02-11. DOI: 10.48550/arXiv.2202.05072.

[22] J. Vielma, 'Mixed Integer Linear Programming Formulation Techniques,' *SIAM Review*, vol. 57, 2015-02. DOI: 10.1137/130915303.

[23] H. G. Svendsen, M. D. Aslesen and S. Wennberg, *Offshore Oil and Gas Energy System Operational Optimisation Model (oogeso) for the Energy System in Longyearbyen*, 2022. [Online]. Available: https://github.com/oogeso/oogeso/tree/longyearbyen-test (visited on 2022-05-09).

[24] Gurobi Optimization, LLC, *Gurobi Optimizer Reference Manual*, 2022. [Online]. Available: https://www.gurobi.com.

[25] Eurostat Data Browser. 'HICP - monthly data (index).' (2022), [Online]. Available: https://ec.europa.eu/eurostat/databrowser/bookmark/d6233597-dc93-4094-971d-a5f31d6fc5b9?lang=en (visited on 2022-04-27).

[26] European Central Bank. 'Euro foreign exchange reference rates - Norwegian krone (NOK).' (2022), [Online]. Available: https://www.ecb.europa.eu/stats/policy_and_exchange_rates/euro_reference_exchange_rates/html/eurofxref-graph-nok.en.html (visited on 2022-04-27).

[27] Danish Energy Agency, *Technology Data for Generation of Electricity and District Heating*, 2022-03. [Online]. Available: https://ens.dk/en/our-services/projections-and-models/technology-data/technology-data-generation-electricity-and (visited on 2022-04-27).

[28] D. kongelige finansdepartement, *Prop. 1 LS Tillegg 1 for budsjettåret 2022*, 2021.

[29] I. Staffell. 'The Energy and Fuel Data Sheet.' (2011-03), [Online]. Available: https://www.claverton-energy.com/wordpress/wp-content/uploads/2012/08/the_energy_and_fuel_data_sheet.pdf (visited on 2022-05-08).

[30] National Research Council and National Academy of Engineering, *The Hydrogen Economy: Opportunities, Costs, Barriers, and R&D Needs*. The National Academies Press, 2004, ISBN: 978-0-309-09163-3. DOI: 10.17226/10922. [Online]. Available: https://nap.nationalacademies.org/catalog/10922/the-hydrogen-economy-opportunities-costs-barriers-and-rd-needs.

[31] U. Bossel and B. Eliasson, 'Energy and the hydrogen economy,' Alternative Fuels Data Center (AFDC), 2002. [Online]. Available: https://afdc.energy.gov/files/pdfs/hyd_economy_bossel_eliasson.pdf.

[32] Statistics Norway (SSB). 'Konsumprisindeksen.' (2022-04-11), [Online]. Available: https://www.ssb.no/priser-og-prisindekser/konsumpriser/statistikk/konsumprisindeksen (visited on 2022-05-08).

[33] Generator Source, *Approximate Diesel Fuel Consumption Chart*. [Online]. Available: https://www.generatorsource.com/Diesel_Fuel_Consumption.aspx (visited on 2022-05-07).

[34] H. Zhang, E. Wang and B. Fan, 'Heat transfer analysis of a finned-tube evaporator for engine exhaust heat recovery,' *Energy Conversion and Management*, vol. 65, pp. 438–447, 2013, Global Conference on Renewable energy and Energy Efficiency for Desert Regions 2011 "GCREEDER 2011", ISSN: 0196-8904. DOI: https://doi.org/10.1016/j.enconman.2012.09.017.

[35] Danish Energy Agency, *Technology Data for Industrial Process Heat*, 2021-11. [Online]. Available: https://ens.dk/en/our-services/projections-and-models/technology-data/technology-data-industrial-process-heat (visited on 2022-05-08).

[36] Danish Energy Agency, *Technology Data for Individual Heating Plants*, 2021-06. [Online]. Available: https://ens.dk/en/our-services/projections-and-models/technology-data/technology-data-individual-heating-plants (visited on 2022-05-08).

[37] Longyearbyen Community Council, 'Longyearbyen kjøper gigantbatteri,' 2022-01-18. [Online]. Available: https://www.lokalstyre.no/longyearbyen-kjoeper-gigantbatteri.6485174-321755.html (visited on 2022-03-17).

[38] Danish Energy Agency, *Technology Data for Energy Storage*, 2020-01. [Online]. Available: https://ens.dk/en/our-services/projections-and-models/technology-data/technology-data-industrial-process-heat (visited on 2022-05-08).

[39] M. Sillesen, 'Solcellene på svalbard dekker opptil 75 prosent av flyplassens forbruk,' *Teknisk ukeblad*, 2019-07-14. [Online]. Available: https://www.tu.no/artikler/solcellene-pa-svalbard-dekker-opp-til-75-prosent-av-flyplassens-forbruk/469726 (visited on 2022-04-27).

[40] K. A. Rosvold, *Watt peak*, in *Store Norske Leksikon*, 2021-11-06. [Online]. Available: https://snl.no/watt_peak (visited on 2022-04-27).

[41] S. Pfenninger and I. Staffell. 'Renewables.ninja Solar PV.' (2022), [Online]. Available: https://www.renewables.ninja (visited on 2022-02-23).

[42] S. Pfenninger and I. Staffell, 'Long-term patterns of european pv output using 30 years of validated hourly reanalysis and satellite data,' *Energy*, vol. 114, pp. 1251–1265, 2016, ISSN: 0360-5442. DOI: https://doi.org/10.1016/j.energy.2016.08.060.

[43] I. Staffell and S. Pfenninger, 'Using bias-corrected reanalysis to simulate current and future wind power output,' *Energy*, vol. 114, pp. 1224–1239, 2016, ISSN: 0360-5442. DOI: https://doi.org/10.1016/j.energy.2016.08.068.

[44] Vestas Wind Systems. '4MW Platform - V105-3.45MW.' (2022-02), [Online]. Available: https://www.vestas.com/en/products/4-mw-platform/V105-3-45-MW (visited on 2022-04-28).

[45] The Wind Power. 'Vestas V105/3450kW.' (2022-01-13), [Online]. Available: https://www.thewindpower.net/turbine_en_1192_vestas_v105-3450.php (visited on 2022-02-23).

[46] J. Wieringa, 'Updating the Davenport roughness classification,' *Journal of Wind Engineering and Industrial Aerodynamics*, vol. 41, no. 1, pp. 357–368, 1992, ISSN: 0167-6105. DOI: https://doi.org/10.1016/0167-6105(92)90434-C. [Online]. Available: https://www.sciencedirect.com/science/article/pii/016761059290434C.

[47] Norwegian Polar Institute, *Map of the Svalbard archipelago (TopoSvalbard)*. [Online]. Available: https://toposvalbard.npolar.no/.

[48] UNIS. 'UNIS Weather stations and CTD stations.' (2022), [Online]. Available: https://www.unis.no/resources/weather-stations/ (visited on 2022-02-23).

[49] A. Grochowicz, D. Heineken and S. Wennberg, 'The reliability of wind power in the Longyearbyen area,' 2021-07-02, Student reports AGF-353/853, UNIS. [Online]. Available: https://www.unis.no/wp-content/uploads/2021/07/Wind_reliability_AGF353.pdf.

[50] The Royal Norwegian Ministry of Climate and Environment, *Lov om miljøvern på Svalbard (Svalbardmiljøloven)*, 2022-03-29. [Online]. Available: https://lovdata.no/lov/2001-06-15-79 (visited on 2022-06-06).

[51] F. Mehlum, L. S. Sømme and S. Barr, *Dyreliv på svalbard*, in *Store Norske Leksikon*, 2020-08-28. [Online]. Available: https://snl.no/Dyreliv_p%C3%A5_Svalbard (visited on 2022-06-06).

[52] EWEA - the European Wind Energy Association, 'Deep water - The next step for offshore energy,' 2013-07. [Online]. Available: http://www.ewea.org/fileadmin/files/library/publications/reports/Deep_Water.pdf (visited on 2022-05-03).

[53] MET Norway, *Weather data for Isfjord radio (SN99790)*, Obtained via the Frost API. [Online]. Available: https://frost.met.no/index.html (visited on 2022-02-23).

[54] Store Norske, *Omstilling til fornybar energi i Arktis - Utviklingsprosjekter*. [Online]. Available: https://www.snsk.no/energi/utviklingsprosjekter (visited on 2022-05-08).

[55] M. Jochmann and G. Nygård. 'Dyp bergvarme: Kan geotermisk energi dekke Longyearbyens oppvarmingsbehov?' Svalbardseminaret 2022, Store Norske. (2022-01-27), [Online]. Available: https://www.youtube.com/watch?v=y5E22Fmy2iU (visited on 2022-05-08).

[56] U.S. Bureau of Labor Statistics, *CPI Inflation calculator*. [Online]. Available: https://www.bls.gov/data/inflation_calculator.htm (visited on 2022-05-03).

[57] Norges Bank, *Valutakurser - Amerikanske dollar (USD)*. [Online]. Available: https://www.norges-bank.no/tema/Statistikk/valutakurser/?tab=currency&id=USD (visited on 2022-05-03).

[58] K. Mongird, V. Viswanathan, J. Alam, C. Vartanian and V. Sprenkle, '2020 Grid Energy Storage Technology Cost and Performance Assessment,' U.S. Department of Energy, 2020-12. [Online]. Available: https://www.pnnl.gov/sites/default/files/media/file/Hydrogen_Methodology.pdf.

[59] National Center for Biotechnology Information. 'PubChem Compound Summary for CID 783, Hydrogen.' (2022), [Online]. Available: https://pubchem.ncbi.nlm.nih.gov/compound/Hydrogen (visited on 2022-05-05).

[60] Nel Hydrogen, *PEM Electrolyser M Series*. [Online]. Available: https://nelhydrogen.com/product/m-series-3/ (visited on 2022-05-03).

[61] A. Ottoson, 'Integration of Hydrogen Production via Water Electrolysis at a CHP Plant - A feasibility study,' Luleå University of Technology, 2021.

[62] The Linde Group. 'Hydrogen technologies - The ionic compressor 50.' (2022-04-28), [Online]. Available: https://www.linde-engineering.com/en/images/DS_IC%2050_tcm19-523715.pdf (visited on 2022-05-06).

[63] A. M. Elberry, J. Thakur, A. Santasalo-Aarnio and M. Larmi, 'Large-scale compressed hydrogen storage as part of renewable electricity storage systems,' *International Journal of Hydrogen Energy*, vol. 46, no. 29, pp. 15 671–15 690, 2021, ISSN: 0360-3199. DOI: https://doi.org/10.1016/j.ijhydene.2021.02.080.

[64] M. A. Khan, C. Young, C. Mackinnon and D. B. Layzell, 'The Techno-Economics of Hydrogen Compression - Technical Brief,' The Transition Accelerator, 2021-10. [Online]. Available: https://transitionaccelerator.ca/wp-content/uploads/2021/10/TA-Briefs-1.2-The-Techno-Economics-of-Hydrogen-Compression-FINALPDF.pdf (visited on 2022-05-06).

[65] International Energy Agency (IEA), 'The Future of Hydrogen - Seizing today's opportunities,' 2019-06. [Online]. Available: https://www.iea.org/reports/the-future-of-hydrogen (visited on 2022-05-06).

[66] International Energy Agency (IEA), 'Technology Roadmap: Hydrogen and Fuel Cells,' 2015-07-15. DOI: 10.1787/9789264239760-en.

[67] C. van Leeuwen and A. Zauner, 'Innovative large-scale energy storage technologies and Power-to-Gas concepts after optimisation - D8.3 - Report on the costs involved with PtG technologies and their potentials across the EU,' EU Horizon 2020, 2018-04-30. [Online]. Available: https://www.storeandgo.info/fileadmin/downloads/deliverables_2019/20190801-STOREandGO-D8.3-RUG-Report_on_the_costs_involved_with_PtG_technologies_and_their_potentials_across_the_EU.pdf (visited on 2022-05-04).

[68] H. Q. Nguyen and B. Shabani, 'Proton exchange membrane fuel cells heat recovery opportunities for combined heating/cooling and power applications,' *Energy Conversion and Management*, vol. 204, p. 112 328, 2020, ISSN: 0196-8904. DOI: https://doi.org/10.1016/j.enconman.2019.112328.

[69] NVE, 'Longyearbyen energy production data 2017-2018,' 2021. [Online]. Available: https://www.nve.no/energy-consumption-and-efficiency/energy-consumption-in-norway/ (visited on 2021-07-01).

[70] K. Haram, 'Norges siste kullgruve legges ned i september 2023,' 2021-09-29. [Online]. Available: https://www.snsk.no/nyheter/6413/norges-siste-kullgruve-legges-ned-i-september-2023 (visited on 2022-05-07).

[71] Longyearbyen Community Council, 'Årsberetning 2020,' 2021-03. [Online]. Available: https://www.lokalstyre.no/getfile.php/4859060.2046.qilankitlbwual/%C3%85rsberetning+2020+LL.pdf (visited on 2022-06-10).

[72] F. Øystå, 'Dette er prislappen - og mer kan det bli,' *Svalbardposten*, 2022-05-12. [Online]. Available: https://www.svalbardposten.no/energiomstilling-longyear-energiverk-longyearbyen-lokalstyre/dette-er-prislappen-og-mer-kan-det-bli/483852 (visited on 2022-06-09).

[73] Varanger Kraft. 'Hydrogenfabrikk - Berlevåg.' (2019-08-28), [Online]. Available: https://www.varanger-kraft.no/hydrogen/ (visited on 2022-05-26).

[74] U.S Energy Information Administration (EIA. 'Short-term energy outlook.' (2022-05-10), [Online]. Available: https://www.eia.gov/outlooks/steo/ (visited on 2022-06-01).

[75] T. Brown, J. Hörsch and D. Schlachtberger, 'PyPSA: Python for Power System Analysis,' *Journal of Open Research Software*, vol. 6, no. 4, 1 2018. DOI: 10.5334/jors.188.

[76] K. van Greevenbroek and L. Klein, *PyPSA-Longyearbyen*, 2021-07-06. [Online]. Available: https://gitlab.com/koenvg/pypsa-longyearbyen (visited on 2022-02-25).

[77] Store Norske, *Omstilling til fornybar energi i Arktis - Om energi*. [Online]. Available: https://www.snsk.no/energi/om-energi (visited on 2022-06-02).

Appendix A

Additional simulated cases

Several cases were simulated in addition to the cases presented in the main text. Results from 12 of the cases, of which 6 are the same as explained in Chapter 5, are given in this appendix. The cases are labeled according to the included devices, with "Base" denoting the existing diesel system and the battery devices. Further additions are photovoltaic cells (PV), Electric boilers (E-boiler), geothermal heat pumps (geothermal), onshore/offshore wind farms, and the hydrogen electrolyser, compressed storage, and fuel cells (hydrogen).

The CO_2 emissions for all cases are shown in Figure A.1. The cases are sorted with decreasing emissions, and the same sorting order is kept for the following figures as well. Emission reductions of up to 65.7% were obtained without wind and hydrogen devices, while reductions of up to 79.4% were obtained without hydrogen devices.

The diesel device running hours per year for all cases that are not fully renewable are displayed in Figure A.2. The diesel generator and diesel boiler usage varies significantly with the varying renewable installations, with the diesel boilers having greater running hours than the diesel generators for only the two offshore wind farm cases.

The combined energy consumption, as well as the renewable share of the corresponding energy production, is given for all 12 cases in Figure A.3. The renewable share climbs significantly with better wind installations, while the total energy consumption is significantly higher for all cases with a hydrogen system, compared to all cases without a hydrogen system.

The curtailed energy for the six cases without the hydrogen system for long term energy storage are shown in Figure A.4. The inclusion of electric heating devices reduced the curtailed PV energy by approximately 74% for all 5 relevant cases. With the geothermal heat pump, more wind power could be curtailed due to the higher efficiency of this heating device compared to the electric boiler. While the latter has lower variable O&M costs, the lower efficiency requires more wind power, and thus yield larger wind O&M costs. As these costs are relatively high for the wind devices, the geothermal heat pump is overall more expensive to use *with wind power* than the electric boiler.

The yearly energy losses for the 12 cases are given in Figure A.5. Of interest in addition to the cases discussed in Section 6.6, is the fully renewable offshore case. The hydrogen system here has energy losses of 10 400 MWh, giving the case energy losses of 10.9% of the total energy production. This makes the share of energy losses almost as large as for the most renewable case without long term storage. Although the efficiencies of electrolysers and fuel cells ultimately are constrained by the laws of thermodynamics, implementing thermal storage devices could minimize the energy loss by recovering as much waste heat as possible at every stage in the hydrogen system.

The equivalent annual costs for all 12 cases is displayed in Figure A.6. The investment costs are included and annualized using the lifetime of each investment and a discount rate of 4%. The diesel related costs constitute over half of the expenses for the cases without a hydrogen system, while the annualized investment costs constitute over half of the expenses for the cases with a hydrogen system. The trend of decreasing equivalent annual costs with decreasing carbon dioxide emissions hold for all cases except the two fully renewable cases, which still have significantly lower costs than the base case.

The O&M costs, fuel costs, and CO_2 costs per year for the 12 cases are given in Figure A.7. These are the costs related to the operation of the different cases that actually arises each year after the investment has been made. The costs clearly decrease with decreasing emissions, as the additional renewable device costs are far outweighed by the reduced costs from reduced diesel usage.

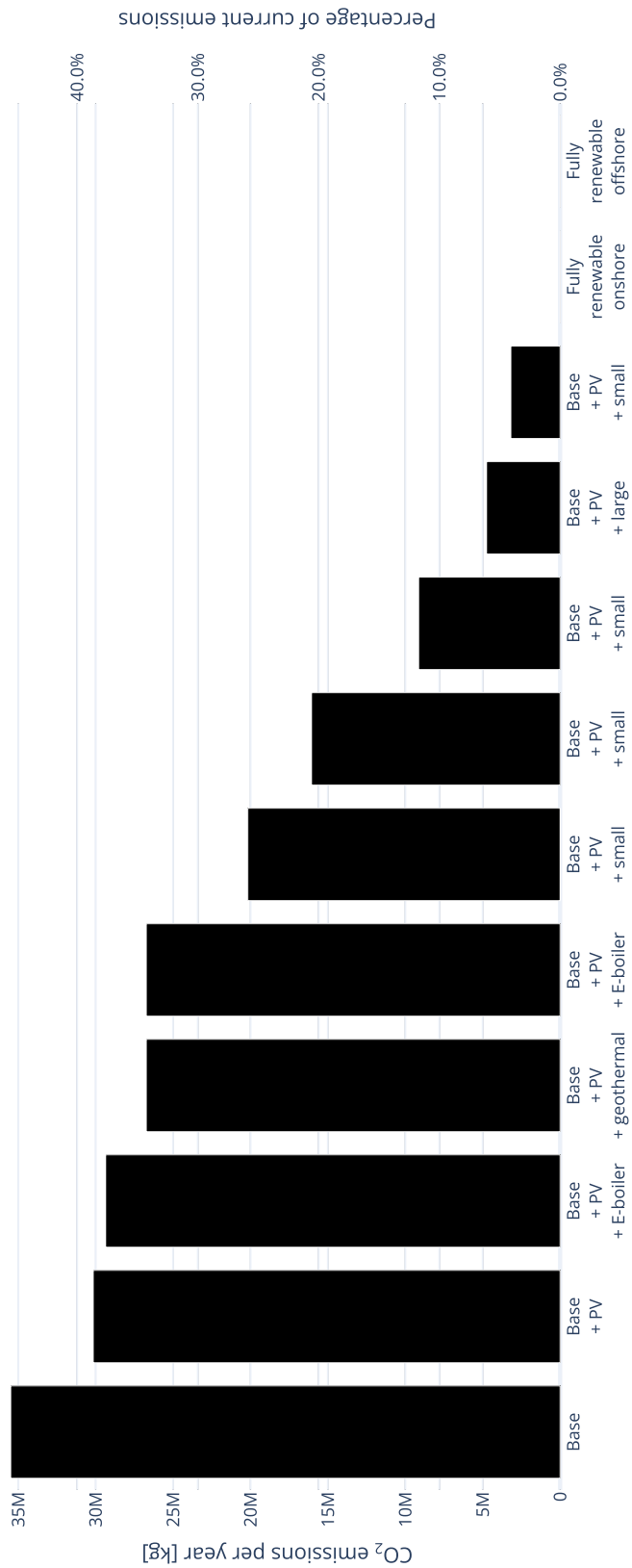

Figure A.1: The carbon dioxide emissions for 12 different simulated cases, compared to the current emissions.

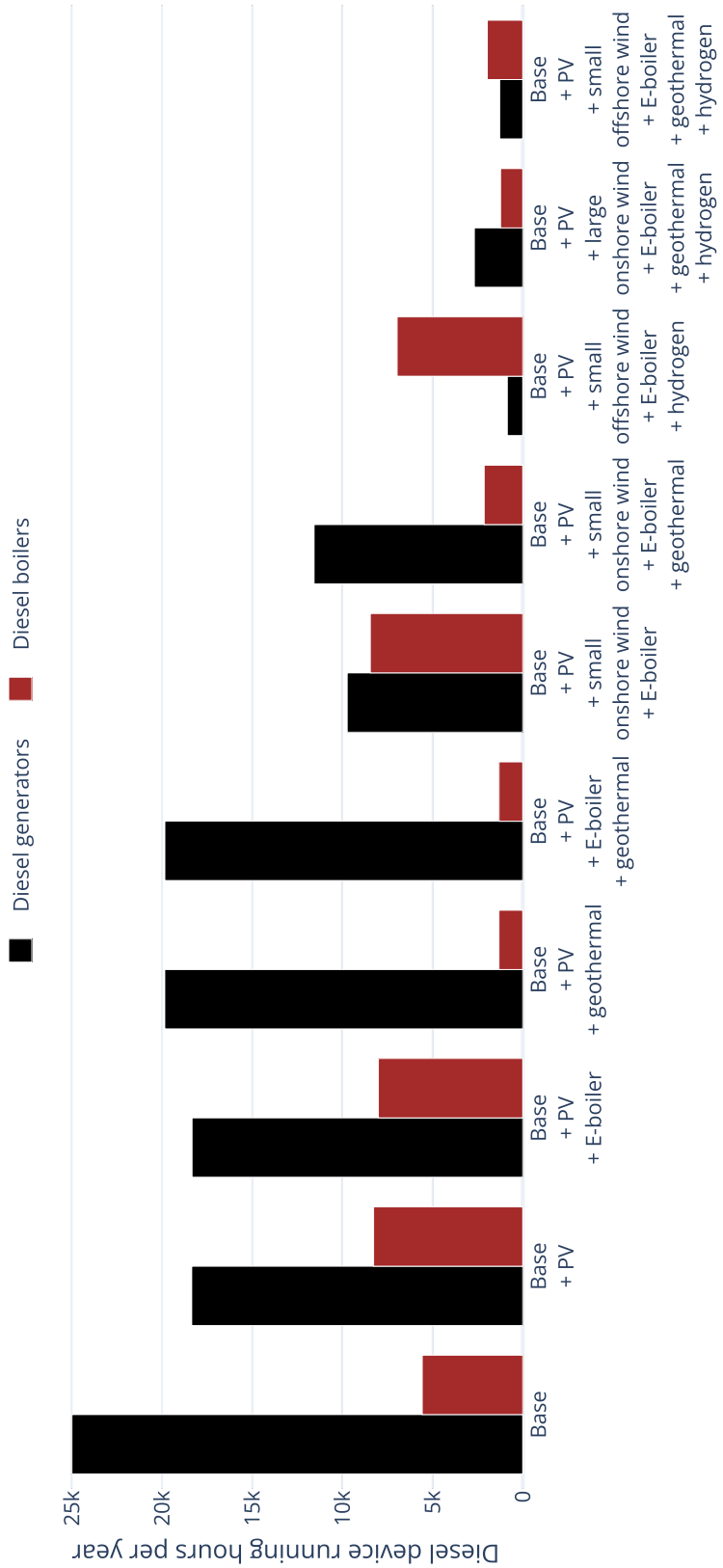

Figure A.2: The running hours of the diesel devices for the one year simulation for 12 different cases.

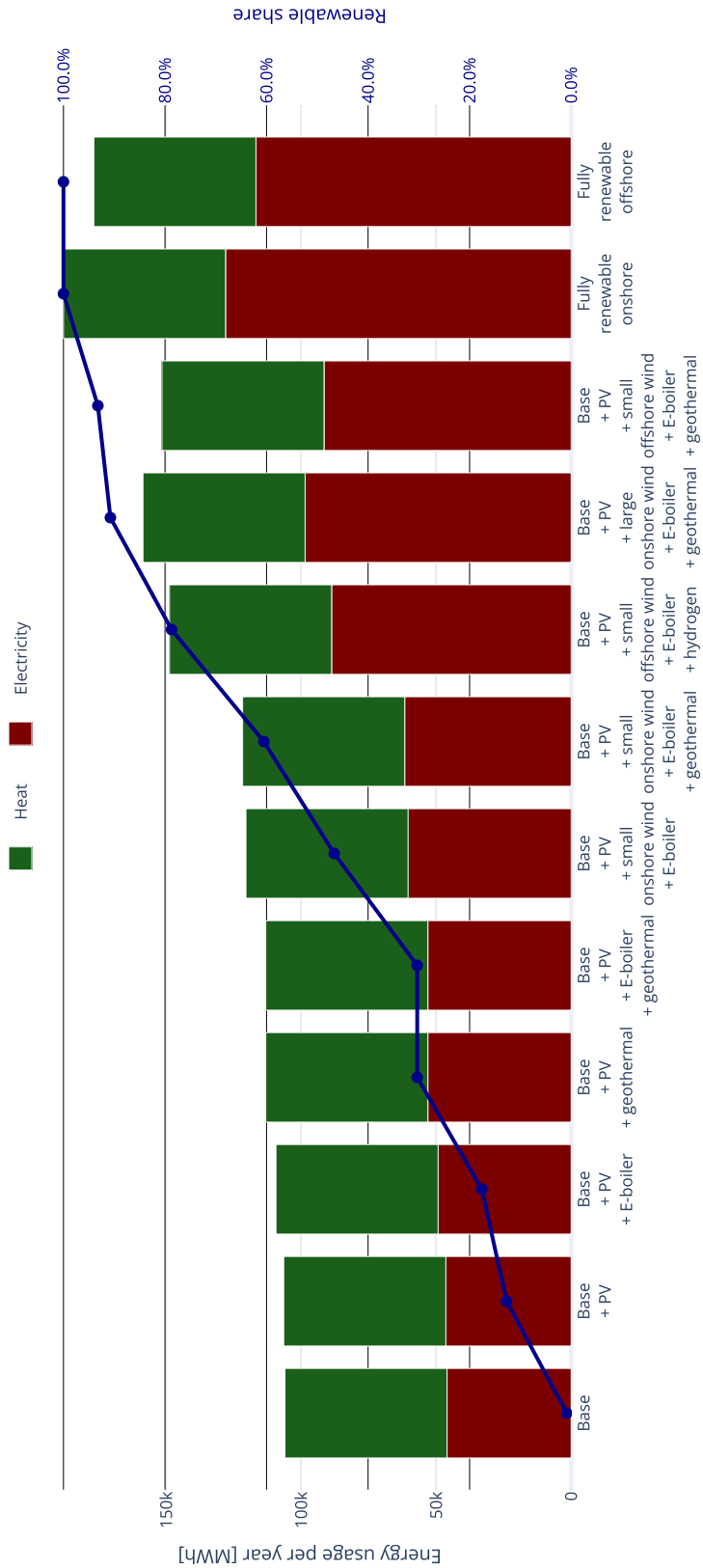

Figure A.3: The total energy consumption, as well as the renewable energy share, for 12 different cases.

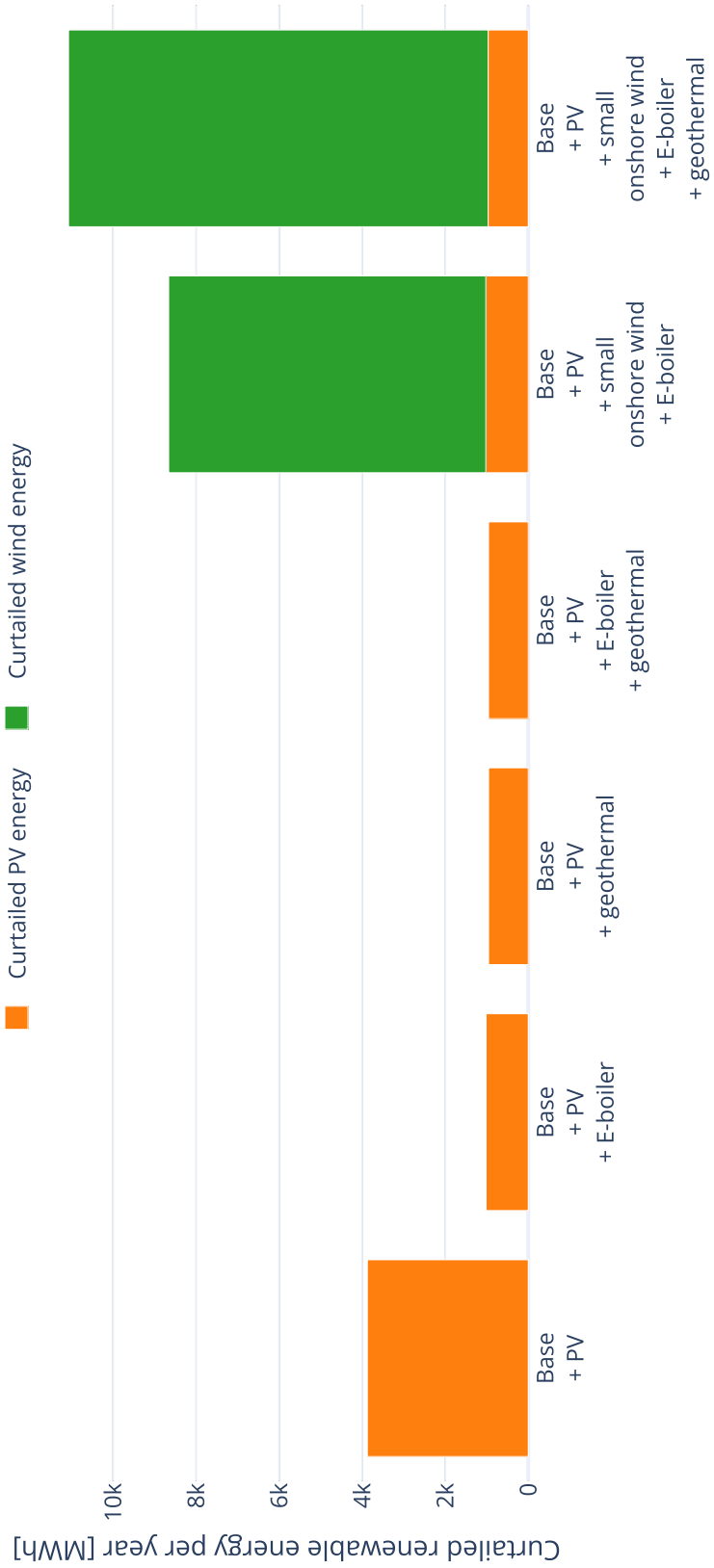

Figure A.4: The curtailed energy from PV and wind sources for 6 different cases without long term storage.

Figure A.5: The yearly energy lost either due to curtailment or from conversion loss when converting electrical energy to heat or stored energy. On the right axis the energy loss is given as the percentage of the produced energy for 12 cases.

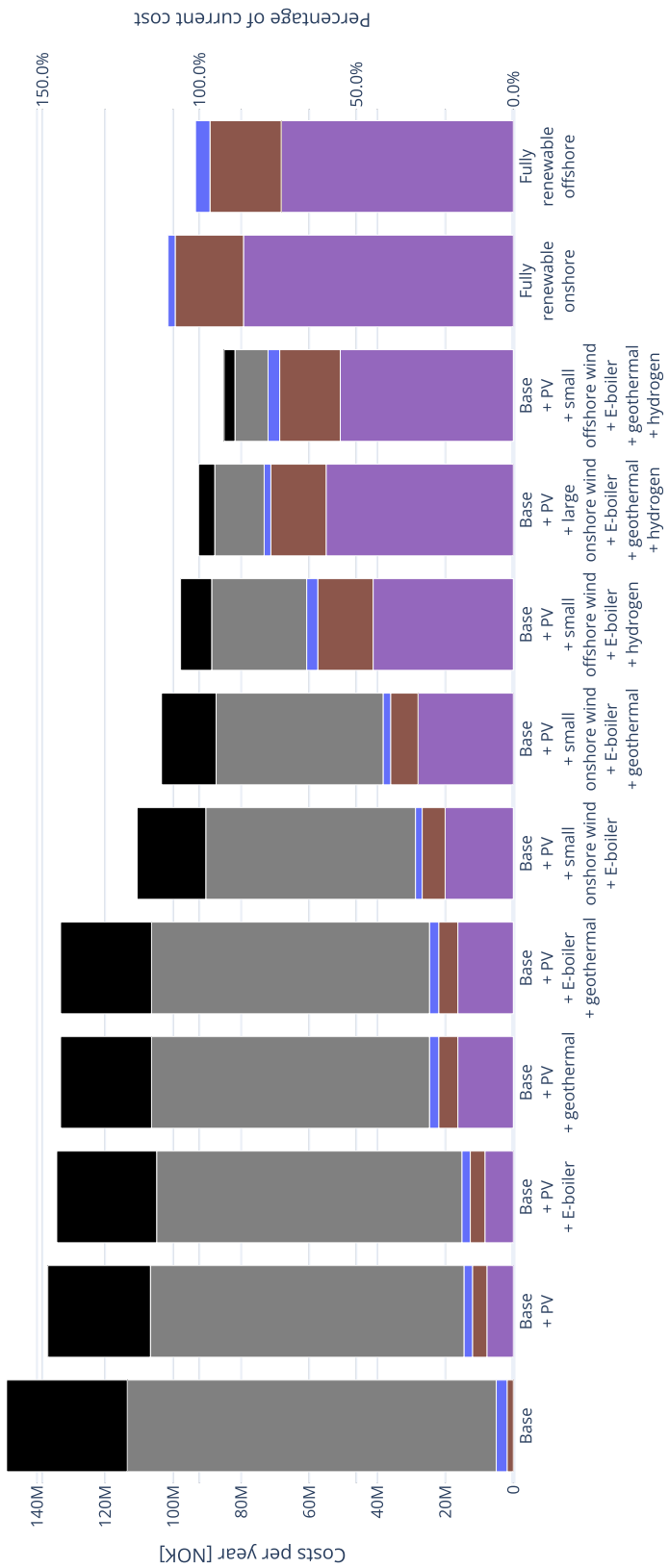

Figure A.6: The yearly costs, with investment costs annualized using the expected lifetime of each investment, for 12 different cases.

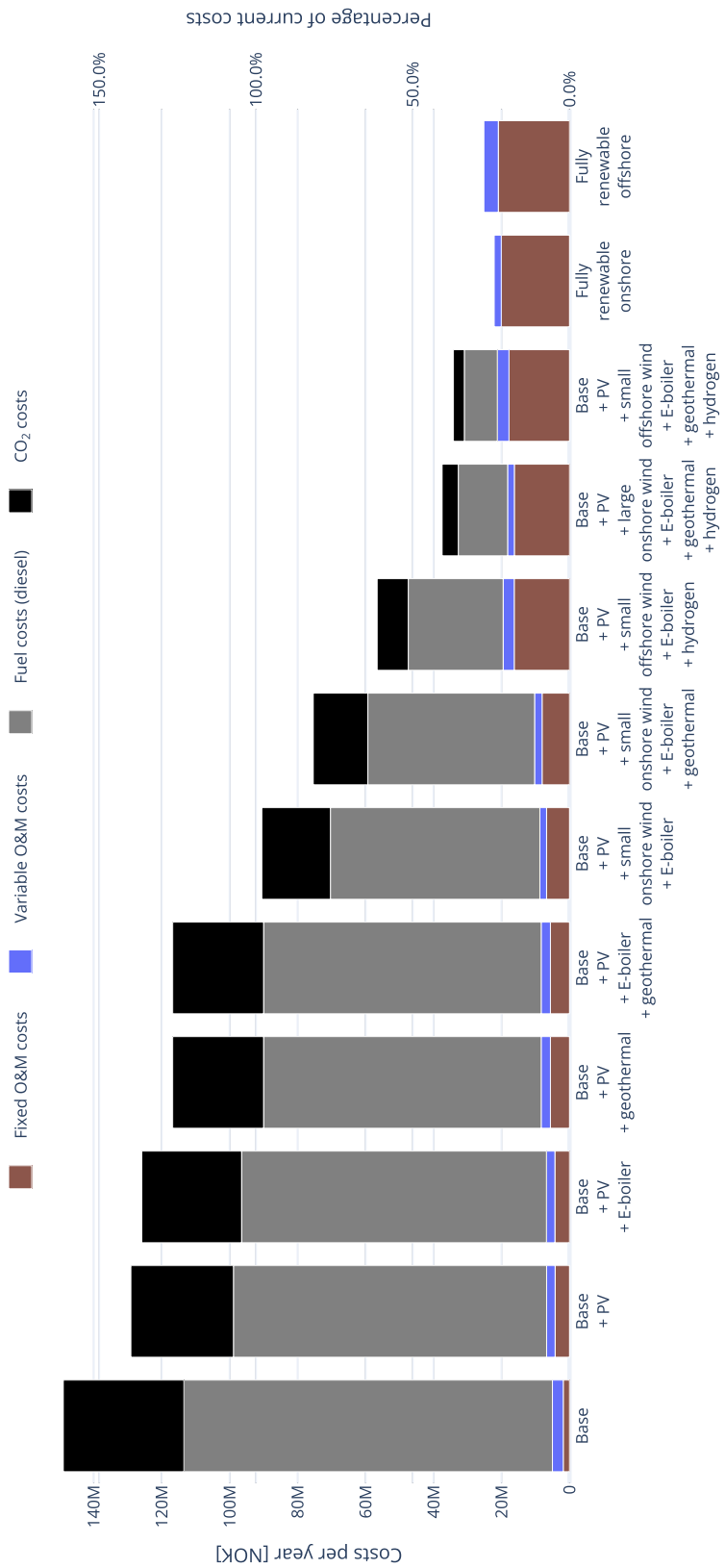

Figure A.7: The operation and maintenance costs, as well as fuel and CO_2 costs, per year for 12 different cases.

Sondre Erik Wennberg

Simulating renewable energy systems for Longyearbyen

NTNU
Norwegian University of
Science and Technology